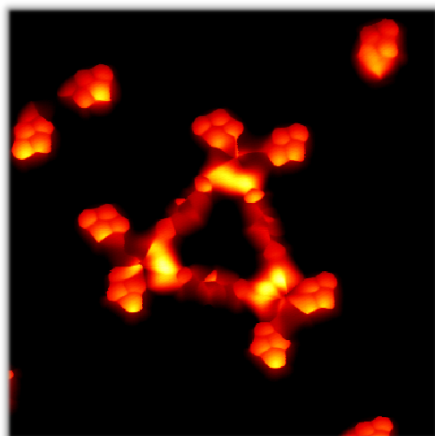


University of the Basque Country
EUSKAL HERRIKO UNIBERTSITATEA (EHU-UPV)



A thesis submitted for the degree of Doctor of Philosophy in
Physics of Nanostructures and Advanced Materials

Functional Materials Synthesis by Surface-Supported Chemistry



Author: Mohammed Sabri Gamal Mohammed

Supervisor: Dimas G. de Oteyza

November 2020

The work presented in this thesis has been carried out at Donostia International Physics Center and Centro de Física de Materiales-Materials Physics Center (CFM-MPC), CSIC-UPV/EHU



*In memory of Abdelsalam Kisha,
a great friend who devoted his life for a revolutionary change*

Acknowledgement

I take this chance to show my high appreciation for so many people who helped me reaching this point, a PhD candidate in physics with a special taste of personal experience. I surely know that I am not the first and definitely not the last, however my experience would have been extremely tough without the support of my beloved family, friends, colleagues and advisors. Staying physically away from my family, old/gold friends for 6 years has never been easy, that didn't stop them from sharing the care and showing their infinite support. So many hard times tackled with you being around.

I would also like to thank a lot all the friends and colleagues during the master's in Italy: all the Sudanese family in Calabria, Andrea Larosa, the brilliant and sometimes crazy friend from Mammola, Ciccio Pecora, the cheerful Cosentino, and all the rest members of the friendly international community there, first experience abroad with a lot of emotions and memories. Grazie di cuore.

In San Sebastian, the very captivating city with the awesome Basque-Spanish culture's mixture, it was like a PhD in the heaven, despite the pain of work (sometimes?!). I am really thankful to all my labmates, Luciano, Nestor, Naoya who already left the small "Apollo" group, James, Tao, and Alex who are still taking some addictive ultrahigh resolution images around. Wider nanophysics group former members Iñiki, Zakaria, Afaf, Jens and the current ones: Paul, Fernando, Khadiza, Rishav, Wen, Carmen, Marina, Rodrigo and Pablo, I wish you good luck mates.

Having a supervisor who becomes a close friend too is not always possible for every PhD student, Dimas made this possible. Joining such a successful group with its friendly atmosphere is a decision that I never regretted. I really thank you for giving me this chance to develop my career, guiding and dedicating much time and effort for that. I hope you got what you expected from my side, as I got from yours. I deeply value the efforts of Donostia International Physics Center DIPC and Centro de Física de Materiales (CSIC-UPV/EHU) teams to facilitate and efficiently make a suitable environment for the belonging researchers, this is made by the smart administration, staff members and workers. I thank you all for this level of excellence and widely-open collaboration in research.

Many thanks extend to whoever has been by my side in some parts of this long journey or all of it. I acknowledge being such lucky to have you around. Thank you all from the bottom of my heart.

Mohammed Sabri
Donostia - San Sebastian, November 2020

Abstract

The mature research field of conventional solution-based chemistry has allowed for a continuous generation of increasingly refined materials with amazing physical and chemical properties. This has contributed to great advances in the field of organic nanomaterials. The development of the recently revealed surface-supported synthesis under ultrahigh vacuum conditions has opened new doors for the formation of defect-free low-dimensional carbon nanostructures that are not achievable by conventional means. This new field, typically termed on-surface synthesis (OSS), is lately showing a booming growth that resonates with almost all the requirements for promising quantum-size materials with tunable physicochemical properties.

In this thesis, this novel approach is applied for the growth of a variety of materials, followed by a comprehensive characterization of the structural, chemical and electronic properties of the intermediates and end-products. This is achieved mainly by scanning tunneling microscopy operating at low temperature (4.3 K) in various measurement modes, assisted by theoretical calculations (DFT and probe particle methods). In particular, the following systems have been studied:

(i) Metal-organic chemistry, in which the stereospecific coupling motif of gold thiolates is found to be controllable by varying the on-surface reaction parameters (i.e. coverage and substrate temperature).

(ii) Pyrene-based chemistry. With alkyne-functionalized pyrene molecules, the impact of the presence of metal-organic complexes on alkyne coupling reactions is investigated. The complexes do not only modify the reaction outcome, but also reduce its activation temperature threshold, becoming an excellent example of second-order on-surface synthesis (i.e. OSS of catalyst to steer following OSS reactions). Secondly, pyrenes are used that are functionalized with alkynes and also Br atoms, allowing for alkyne homo- and cross-coupling reactions. The resulting products and their relative abundance are explored thoroughly after different annealing steps, revealing a dominant Glaser-coupling product upon heating. The absence of the latter when using non-halogenated precursor evidenced the role of Br in this coupling reaction. Importantly, a systematic comparison of the electronic properties of the different product structures has allowed drawing important structure-property relations with regard to the various inter-pyrene coupling motifs.

(iii) Acene-based chemistry. The synthesis of higher acenes is studied, in particular heptacene on Ag(001), starting from tetrahydroheptacene molecular precursors with and without additional functionalization by Br atoms. A variety of stable reaction intermediates is found, often resulting from hydrogen migration events. However, heptacene is the end-product from the two precursors and displays a fully charged LUMO orbital. Focusing on the intermediates, two sp^3 -hybridized carbon atoms present at the second ring of dihydroheptacene are shown as sufficient self-decoupling factors. Magnetic Kondo fingerprints associated to specific charging scenarios are investigated. Finally, the impact of the surface structure on coupling reactions with acene-based precursors is then explored. More specifically, Au(111) and Au(110) surfaces, as well as anthracene precursors functionalized with halogen and methyls are used with this aim. On Au(111), the atomically flat surface, five covalent coupling motifs are found, with the 3-fold symmetric starphene showing the highest occurrence upon annealing. In contrast, on Au(110), being a 2×1 reconstructed surface, the uniaxial symmetry of the surface promotes the formation of mainly linear non-benzenoid polymers along the grooves of this substrate.

This thesis contributes to the surface science field by showing the possibility to synthesize a variety of novel carbon-based nanomaterials using on-surface synthesis methods. The second main contribution is the detailed characterization of the produced materials using surface-sensitive techniques assisted by theoretical calculations. A deep understanding of the physicochemical properties of these materials is a crucial step forward towards their ultimately progressing applications.

Resumen

La química orgánica es un campo de investigación extremadamente maduro cuyos continuos avances han ido permitiendo la generación de materiales cada vez más refinados, caracterizados por fascinantes propiedades físicas y químicas. La aplicación de tales compuestos orgánicos nanoestructurados ha ido generando importantes impulsos al campo de la nanociencia. En los últimos 15 años se está desarrollando una nueva alternativa a la química convencional: la síntesis en superficies (“on-surface synthesis”, OSS) bajo condiciones de ultra alto vacío. Este nuevo planteamiento ha abierto nuevas puertas para la formación de nanoestructuras de carbono que no están al alcance de los métodos convencionales. Su aplicación para la síntesis de materiales orgánicos de baja dimensionalidad y con precisión atómica está mostrando un crecimiento en auge y tiene un enorme potencial para aplicaciones que incluyen nuevas tecnologías cuánticas.

En esta tesis, este novedoso enfoque se aplica al crecimiento de diferentes tipos de materiales, seguido de una caracterización integral de las propiedades estructurales, químicas y electrónicas de los productos intermedios y finales. Para tal fin se ha utilizado principalmente la microscopía túnel de barrido a baja temperatura (4,3 K) en varios modos de medición, complementados con cálculos teóricos (DFT y métodos de partículas de sonda). En concreto se han estudiado los siguientes sistemas:

(i) Química metal-orgánica, en la que se muestra la manera de controlar la estructura de enlace de tiolatos de oro y su estereoespecificidad variando los parámetros de reacción en la superficie (recubrimiento y temperatura del sustrato).

(ii) Química basada en pirenos. Usando moléculas de pireno funcionalizadas con alquinos, se investiga el efecto de los complejos metal-orgánicos descritos anteriormente en las reacciones de acoplamiento de alquinos. Los complejos metal-orgánicos no solo modifican el resultado de la reacción, sino que también reducen el umbral de la temperatura de activación, siendo por tanto un excelente ejemplo de síntesis en superficie de segundo orden (es decir, OSS del catalizador para dirigir nuevas reacciones de OSS). De otro lado, también se han utilizado pirenos funcionalizados con dos tipos de grupos funcionales distintos, como son los alquinos y átomos de Br. La presencia de ambos grupos funcionales permite nuevo abanico de reacciones que incluyen el tanto el acoplamiento de alquinos o el acoplamiento cruzado. El análisis de los productos resultantes y su abundancia tras tratamientos de calentamiento muestran una dominancia del acoplamiento de Glaser (acoplamiento de alquinos con pérdida de hidrógeno) como reacción inicial. Sin embargo, al utilizar un precursor no halogenado se observa una prevalencia de un acoplamiento sin pérdida de hidrógeno y una total ausencia de acoplamiento Glaser, evidenciando el papel crítico del Br en la reactividad de alquinos. Es importante destacar también que una comparación sistemática de las propiedades electrónicas de las diferentes estructuras de los productos ha permitido trazar importantes relaciones entre la estructura y las propiedades de los diversos tipos de acoplamientos entre pirenos.

(iii) Química basada en acenos. Se ha estudiado la síntesis de acenos de gran tamaño, en concreto de heptaceno sobre Ag(001), a partir de precursores moleculares de tetrahydroheptaceno con y sin funcionalización adicional por átomos de Br. Se ha encontrado una variedad de productos intermedios que a menudo resultan de eventos de migración de hidrógeno. Sin embargo, el heptaceno es el producto final de los dos precursores y muestra un orbital LUMO completamente cargado. Centrándonos en los intermedios, se observa cómo dos átomos de carbono con hibridación sp^3 en el segundo anillo de dihydroheptaceno son suficientes para causar el auto-desacoplamiento electrónico de la molécula y el sustrato. Se han investigado asimismo las señales magnéticas, evidenciadas en resonancias Kondo, asociadas a determinados escenarios de carga. Finalmente, utilizando precursores basados en acenos se ha explorado el impacto del sustrato en las reacciones de acoplamiento. En concreto se han utilizado superficies de Au(111) y Au(110), así como precursores de antraceno funcionalizados con halógenos y metilos. Sobre Au(111), una superficie atómicamente plana, se encuentran cinco tipos de productos covalentes, siendo el “starphene” con simetría de eje ternario el producto dominante. Por contra, sobre la superficie reconstruida de Au(110) 2×1 , su simetría uniaxial promueve la formación de polímeros lineales no benzenoides.

Esta tesis contribuye al campo de la ciencia de superficies, mostrando la posibilidad de sintetizar una variedad de nanomateriales novedosos basados en carbono mediante la síntesis en superficie, así como mediante la caracterización detallada sus propiedades. La comprensión de las propiedades físico-químicas de estos materiales avanzados es un paso de gran relevancia hacia sus futuras aplicaciones.

Contents

1	Introduction	3
1.1	State of the art strategies for production of functional materials at the nano scale: top-down v.s bottom-up	3
1.2	On-surface reactions	4
1.3	Dissertation overview	9
2	Principles, methods, and techniques	10
2.1	Introduction	10
2.2	Ultra-high vacuum	10
2.3	STM and STS	10
2.3.1	STM imaging basics	10
2.3.2	STM theoretical aspects	11
2.3.3	Scanning tunneling spectroscopy	12
2.3.4	SPM tip functionalization	14
2.3.5	The impact of tip character on molecular orbitals imaging	15
2.4	XPS	16
2.5	LEED	17
2.6	Sample prep.	18
2.6.1	Sample cleaning	18
2.6.2	Molecular deposition by thermal evaporation	19
2.7	Tip preparation	20
2.7.1	CO-molecules identification on various surfaces	20
2.7.2	Technical CO-functionalization methods	21
2.7.3	Cl-functionalization of the STM tip	21
2.7.4	High-resolution imaging and dI/dV measurements	22
2.8	Kondo analysis	22
2.9	Instrumentation	23
3	Metal-organic chemistry	24
3.1	Introduction	24
3.2	Results and discussion	25
3.3	Conclusion	34

4 Pyrene-based chemistry	35
4.1 Steering alkyne homocoupling with on-surface synthesized metal–organic complexes	35
4.1.1 Introduction	35
4.1.2 Results and discussion	35
4.1.3 Conclusion	40
4.2 Alkyne coupling reactions	42
4.2.1 Introduction	42
4.2.2 Results and discussion	43
4.2.3 Conclusion	56
5 Acene-based chemistry	57
5.1 On-surface synthesis of heptacene from brominated and non-brominated precursors	57
5.1.1 Introduction	57
5.1.2 Results and discussion	57
5.1.3 Conclusion	63
5.2 Self-decoupling of polyacenes	64
5.2.1 Introduction	64
5.2.2 Results and discussion	64
5.2.3 Conclusion	71
5.3 From starphenes to non-benzenoid linear conjugated polymers by substrate templating	72
5.3.1 Introduction	72
5.3.2 Results and discussion	72
5.3.3 Conclusion	81
A List of publications	82
A.1 Derived from this thesis	82
A.2 Other publications	82

Chapter 1

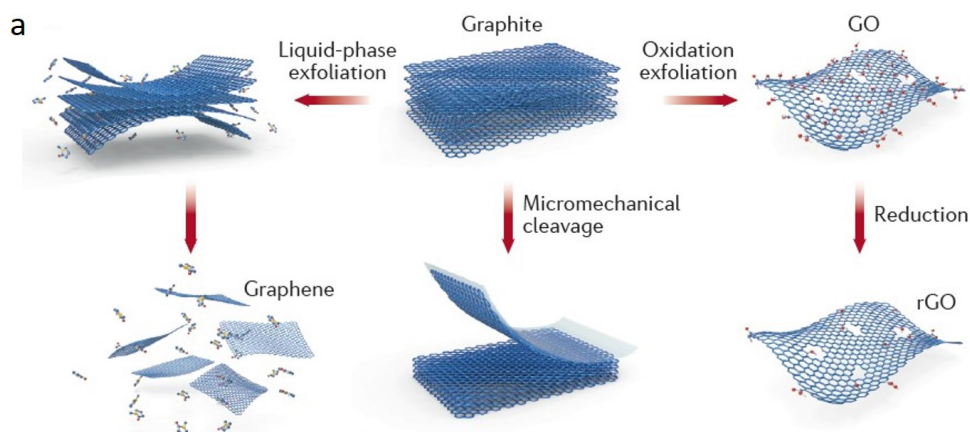
Introduction

1.1 State of the art strategies for production of functional materials at the nano scale: top-down v.s bottom-up

The methodological aspects used over the past few years for the fabrication of organic nanomaterials with attracting physical and chemical properties on metal surfaces rely on two main approaches:

1. *Top-down approach:*

In which materials are reshaped into the desired end-product. An excellent example is the use of top-down approach for the production of graphene sheets from graphite. The first graphene sheet was produced using an adhesive tape to micro-mechanically exfoliate graphene with few millimetres size from graphite¹ exhibiting electronic properties close to those expected from calculations² and leading to winning the Nobel prize in physics 2010 for this interesting field of research. Other techniques include the chemical methods for graphene synthesis using graphite oxide as a precursor, exfoliation to 2D graphene oxide (GO) and then reduction either chemically by hydrazine or thermally for achieving reduced graphene oxide (rGO). However the rGO-produced graphene exhibits undesired structural defects and high carbon-to-oxygen ratio (about 10) which have a direct impact on the electronic properties, namely the charge-carrier mobility. Liquid-phase exfoliation of graphite in solvents with surface tension that favours the detachment of the layered graphite (i.e. N-methyl-2-pyrrolidone) assisted by sonication and subsequent centrifugation is shown to produce better quality graphene structures when compared to those of GO reduction.³



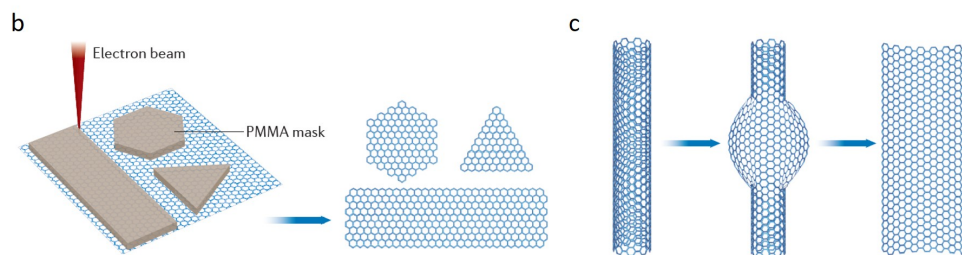


Figure 1.1: Typical production methods of graphene using top-down approach at larger scales a, electron beam lithography and unzipping of carbon nanotubes b-c for producing nano meter sized graphene structures. Adopted from ref. [4]

Going down to nano scale, graphene quantum dots (GQDs) can be produced using electron-beam lithography to cut the graphene sheet in different shapes by employing, for instance polymethylmethacrylate (PMMA) masks with the desired structure to shield it while oxygen plasma etching.⁵ These few nanometers sized graphene structures (also called nanographenes) can be achieved by unzipping carbon nanotubes CNTs as well. What calls the attention in these nanographenes is their electronic bandgaps due to the quantum confinement of electrons. One particularly promising candidate for molecular devices is graphene nanoribbons (GNRs) which exhibit electronic bandgap inversely proportional to the width of the GNR.

2. Bottom-up approach:

Despite the valuable progress achieved by top-down approach for the production of materials, it remains challenging to achieve structurally well-defined defect-free organic nanostructures, as the precision in the fabrication process does not reach the atomic level and thus often impacts the physics and the chemistry of the end-product.

To achieve new classes of nanomaterials with atomic precision, a different approach becomes necessary from the bottom-up. That is, the materials are produced by the self-organization of appropriately designed building blocks. Although for organic materials the most common interactions exploited for the self-assembly have been non-covalent in nature, the use of chemical reactions leading to covalently bonded structures is greatly increasing in the last years, a growing field that, when confined to well-defined surfaces, is typically termed as "on-surface synthesis".

1.2 On-surface reactions

There are major differences when comparing on-surface chemistry to the conventional solvent-based chemistry. These differences are most obvious in the environment (on-surface synthesis is often performed under vacuum), as well as in the two-dimensional confinement for the former. The reduced dimensionality affects the intermolecular interactions and thus also the possible reaction schemes. As a result, new materials can be synthesized that are not achievable by conventional means. In addition, vacuum environment further allows synthesizing and characterizing molecular structures that would not be stable in solution.

On-surface reactions can be activated in different manners. Thermally by heating the substrate after/during the deposition of the precursor molecules, by photo-activation with light sources, or using the STM-tip to overcome the energy barriers to trigger the chemical reactions on the surface.

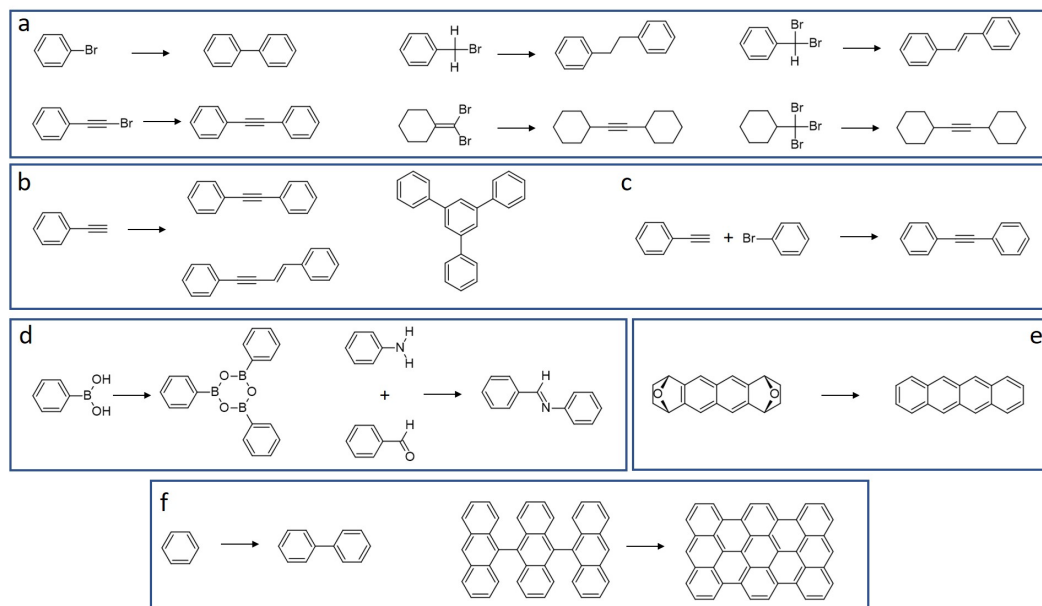


Figure 1.2: Typical reactions used in on-surface synthesis a) dehalogenative coupling b) alkyne coupling c) Sonogashira coupling d) condensation reactions e) reduction reactions f) inter- and intramolecular C-H activation reactions.

The most popular reactions in the field of on-surface chemistry for covalent linking of the building block precursor molecules consist of Ullmann-coupling reactions, in which a carbon-halogen bond is cleaved leaving radicals at the position of the specific carbon atom, followed by covalent bond formation with another similarly radical-possessing carbon atom. Such dehalogenative reactions are widely used in on-surface chemistry due to their efficiency and robustness, which opens a wide door for designing the precursor molecules with the halogens at positions of choice for precise engineering of the end-product. Other common types of on-surface reactions are dehydrogenative coupling reactions, where C-H bonds are activated for the formation of a new C-C covalent bond at the intermolecular or intramolecular level. Alkyne coupling reactions are also among the most studied and commonly used surface-supported reactions. These and other common on-surface reactions are schematically shown in figure 1.2. The most important parameters determining the performance of on-surface synthesis reactions and the associated outcome are the following:

1. The design of the precursor molecules

An important choice to be made before moving to the step of synthesizing organic nanostructures *via* on surface chemistry is how we design the precursor molecules with capability to activate certain reaction/reactions assisted by the surface in the UHV environment. The chemical changes that these precursors undergo in the UHV can consist of single/multiple reaction steps. In case of the latter, it can be extremely useful to separately control the activation of subsequent steps, allowing e.g. for the hierarchic growth of molecular nanoarchitectures. Beautiful examples of the importance of the precursor design have been shown in the field of on-surface synthesis of graphene nanoribbons.⁶⁻¹² Changing only the halogen atom positions within the building unit (a binthryl precursor molecule) leads to different structures of the end-product after undergoing two on-surface reaction steps: the first is the polymerization after dehalogenation and C-C bond formation (Ullmann coupling reaction), and the second is the cyclodehydrogenation after which we get the planar GNR structure. This is pictured in Figure 1.3.

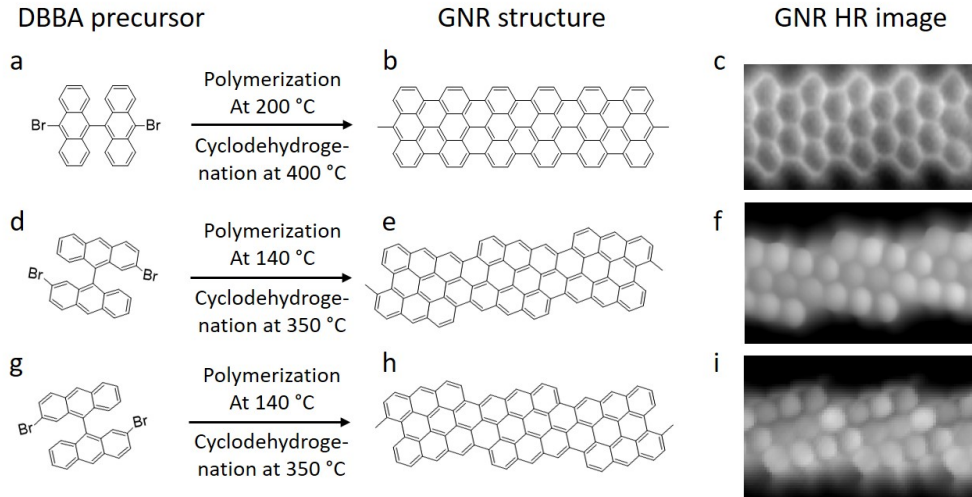


Figure 1.3: On-surface synthesis routes for graphene nanoribbons with different edge orientation obtained by changing the Br positions on the DBBA precursor: 7-armchair GNRs a-c,^{6,13,14} and (3,1) GNRs with different prochirality d-f and g-h.^{7,15}

2. The choice of the substrate

The playground to be utilized in the process of making controllable reactions on is of a great importance. Substrate reactivity, crystallographic orientation, epitaxial growth and templating effects are the parameters through which the surface contributes in the reactions of the adsorbed materials. Among the most used substrates for on-surface reactions, Au comes on top due to its low interaction with the molecular adsorbates, leading in most of the case to physisorption. This low coupling makes Au widely used in the field of scanning tunneling spectroscopy (STS) as the hybridization of the molecule-substrate is reduced which helps in showing a more clear appearance of the molecular electronic states. This is further explained in the next chapter when we show the requirements for optimum STS measurements. Other metals as Ag and Cu have also been used in on-surface synthesis with higher molecule-substrate interaction (higher for Cu than Ag) exhibiting the chemisorption scenario. Some reports for reactions on Pt,^{16–20} Co,²¹ Pd,^{22–24} and on insulators^{25–27} are shown to be successful as well. Kinetic stabilization of reaction intermediates has also been reported to result from substrate thermalization and the efficiency of energy-dissipation.^{28,29}

Previous reports have studied the intrinsic nature of the substrate on the growth of on-surface synthesized materials, figure 1.4 shows an example of the impact of substrate's nature on the Ullmann-type reaction of trisbromophenylbenzene (TBPB) molecules comparing 111 surfaces of Cu, Au and Ag.

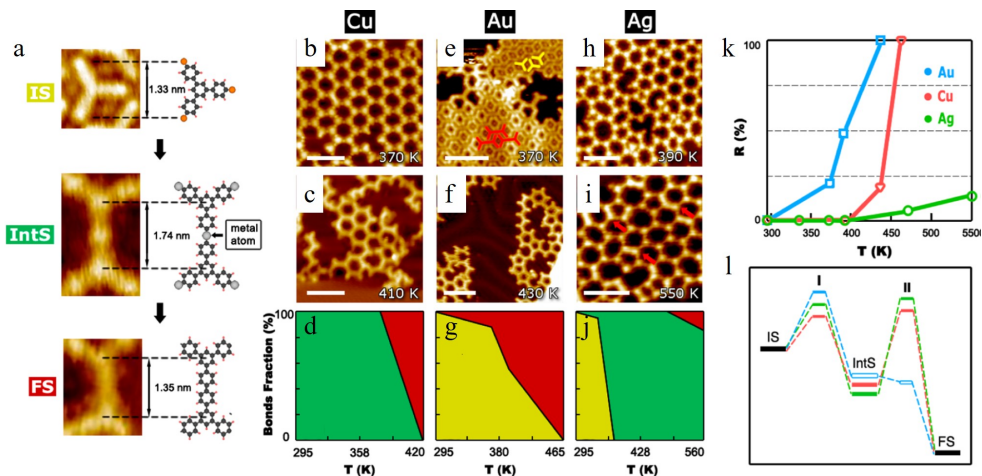


Figure 1.4: The influence of substrate's nature on TBPB molecules coupling on Cu(111), Au(111) and Ag(111). a) STM topography images of the initial state (IS) in yellow, the organometallic intermediate state (IntS) in green and the final state (FS) of covalently-bonded structure in green. Representative STM

topography images and occurrence of the product states as a function of temperature on b-d) Cu, e-g) Au and h-j) Ag. k) Conversion ration of the covalently-bonded structure as a function of the annealing temperate for the three different surfaces. l) Schematic Ullmann-coupling energy diagram for showing relative energy position of the states on the three surfaces. Adopted from ref. [30] (a-k) and ref. [31] (l).

The evolution of the initial state (IS), intermediate organo-metallic state (IntS) and the final state (FS) during the Ullmann reaction on the three surfaces of Cu(111), Au(111) and Ag(111) is different as a function of annealing temperature (figure 1.4 (b-d)). Au(111) shows a high reaction activation efficiency, then comes Cu(111) and Ag(111) with gradually decreasing efficiencies.^{30,31} The same concept is predicted from theoretical calculations for Ullmann reaction mechanisms of (Br and I) functionalized phenyls with different reaction rates as a function of annealing temperature comparing Au(111), Ag(111) and Cu(111) surfaces.³²

Among the substrate properties that can impact the synthesis process is also the surface orientation. The same material with a different orientation may behave very differently in on-surface reactions. For instance, the periodic steps in Au(322) have been used to control the growth of graphene nanoribbons from dibromo-paraterphenyl (DBTP) precursor, resulting in a highly controlled yield of 6 atom-wide armchair GNRs, whereas a variety of GNRs of different widths is obtained on flat Au(111).³³

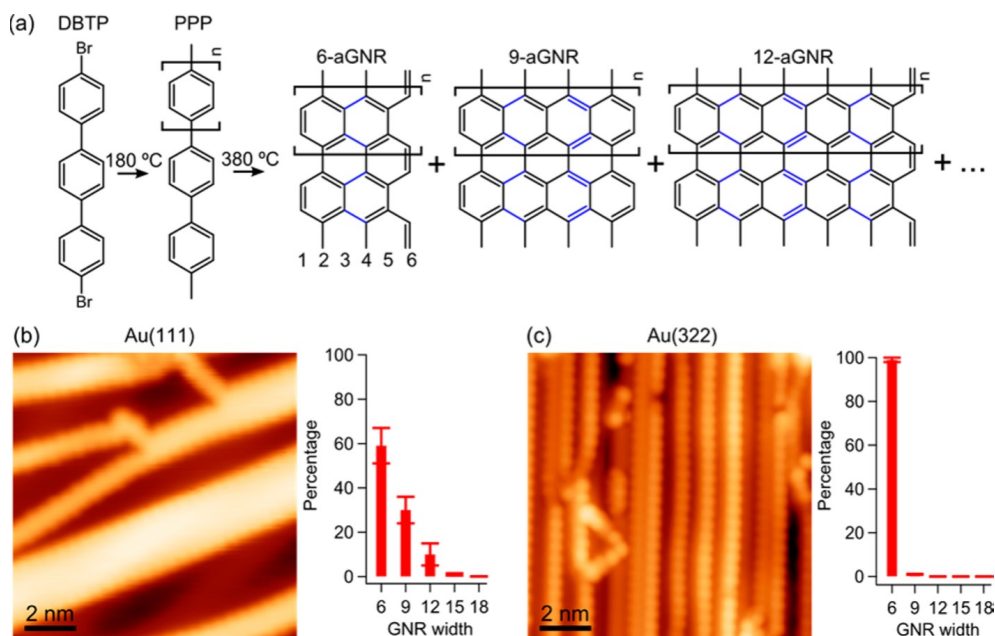


Figure 1.5: Comparative study of the on-surface synthesized armchair graphene nanoribbons from DBTP molecules. a) Showing the reaction path including the first Ullmann coupling to form the linear poly-paraphenylene (PPP) chains, followed by cyclodehydrogenation to form armchair GNRs. b-c) STM topography images of GNRs product and statistics for the resulting width on Au(111) and Au(322) respectively. Adopted from ref. [33]

3. The characterization technique

For the characterization of these systems, the well-defined surfaces and UHV environment enable the use of a whole battery of surface science techniques. By far the most popular are scanning probe microscopy (nc-AFM and STM) methods, probably because of their ability to resolve not only the topographical shape of the molecules, but even the bonding structure that allows the identification of the reaction products for each on-surface reaction step using functionalized tips, and thereby provides information on reaction mechanisms. A pioneering example thereof is shown in Fig. 1.6, in which de Oteyza et al., presented the application of nc-AFM for studying complex on-surface transformation and cyclization processes of individual oligo-(phenylene-1,2-ethynyls) on Ag(100) with an astonishing level of resolution of the reactant molecule and the different products.³⁴ Moreover, STS stands out as a powerful technique for addressing the electronic properties of on-surface synthesized materials allowing for the determination of the electronic band structure in both valence and conduction band regimes and making the localization of electron local density

of states (LDOS) within these structures possible. Furthermore, nc-AFM allows for mapping the local contact potential difference LCPD, which corresponds to the conventional Kelvin probe force microscopy (KPFM) measurement. This helps in understanding many surface and reaction phenomena as the surface reconstruction, surface inhomogeneities (dopants and defects) and for tracking the charge distribution at a single-atom level.^{35,36} As introduced earlier in this chapter, STM tips were proved to be util not only for characterization but also for activation of on-surface chemical reactions,^{37–39} and for manipulating molecules over the surface to move them from or to a specific region (e.g decoupling layer) for further characterization.^{10,40–42}

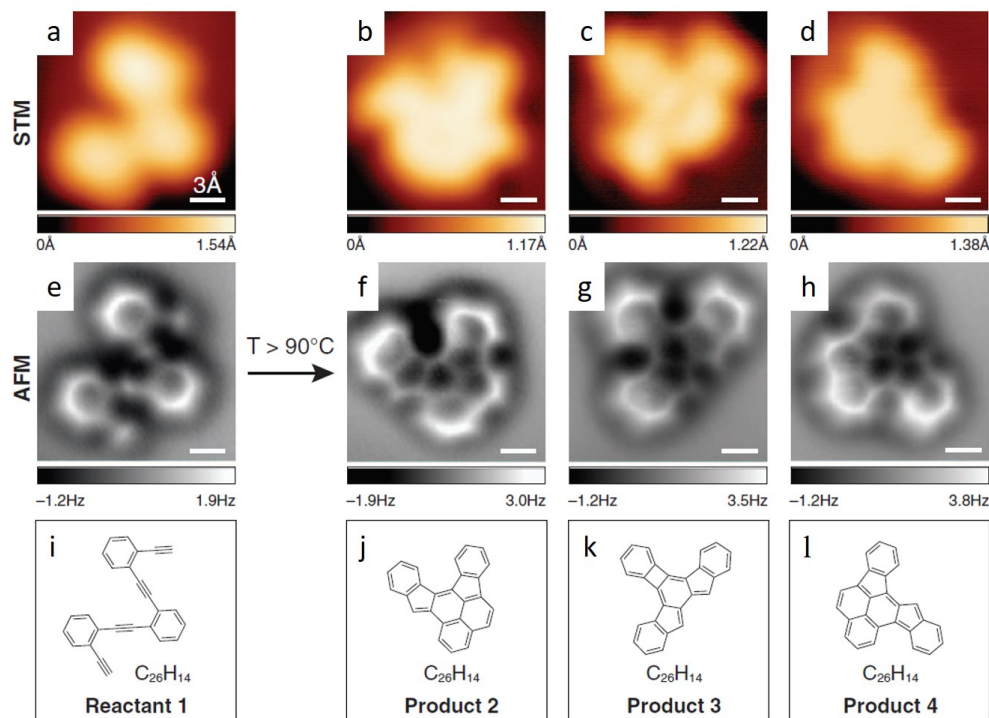


Figure 1.6: STM topography a-c) nc-AFM images e-h) and the chemical structure i-l) of the reactant molecule and the different intramolecular on-surface reaction products. Adopted from ref. [34]

Nevertheless, there are some limitations for each of SPM techniques like the inability to scan insulating materials using conventional STM and the planarity prerequisite in both techniques for UHR-imaging the structures as it requires constant-height scanning mode with functionalized tips, that operation mode leads -in the best case scenario- for losing the tip when scanning non-planar structures. Next chapter includes further principal and technical details.

Chemical composition characterization of surface-supported reactions is normally performed using X-ray photoelectron spectroscopy XPS which is a spectroscopic technique to characterize the chemical and the electronic state of the elements on the surface within the first few nanometers to clarify the bond formation and bond breaking steps.^{43,44} Moreover, temperature-dependent XPS is capable to track the whole reaction process not only limited to the chemical bond changes^{45,46} and the molecules desorption but also the the changes in the substrate structure upon adsorption and reaction.⁴⁷

Further spectroscopy techniques have also been employed for the characterization of on-surface organic nanomaterials. By way of example, Raman spectroscopy can be used to study the chemical properties of materials and, not requiring conductive substrates, it allows assessing the chemical stability of on-surface synthesized products upon transfer to different substrates as well as over time. Further examples include UV-visible spectroscopy to investigate the absorption properties materials,⁴⁸ angle-resolved photoemission spectroscopy (ARPES), core-level XPS and near edge X-ray absorption fine structure (NEXAFS) as surface averaging techniques that provide information on the chemical and electronic properties of the materials, or low energy electron diffraction (LEED) to obtain structural information about the surface or adsorbates.⁴⁹

Altogether, surface-sensitive techniques provide important structural, electronic, optical and chemical information about on-surface synthesized nanomaterials. However, the limitations of

each technique is something to be considered specially because most of the facilities have only very few -if not only one- of these techniques which takes us back to the question of what properties do we exactly want to investigate out of the specific synthesis study case. This is also a nice chance of collaboration when other techniques are required, but organic materials synthesized on-surfaces are often unstable to atmosphere pressures so sample transfer mechanisms (e.g vacuum suitcases) or re-preparation is to be considered in such cases.

1.3 Dissertation overview

In this dissertation the main focus will be on the synthesis and characterization of novel functional materials, providing answers to most of the following questions:

1. What is the on-surface reaction mechanism for achieving reaction species?
2. What is the role of the underlying substrate?
3. What is the chemical structure and the electronic properties of the different molecular species as characterized by the available techniques?
4. How do the experimental results compare to theoretical calculations?

The dissertation is divided into six chapters. In this first chapter we have already introduced the motivation behind this project, aiming for synthesizing and characterizing organic nanomaterials *via* on-surface reactions as an emerging bottom-up approach. Since these materials are being synthesized under ultra-high vacuum conditions and characterized by specific techniques, mainly low-temperature scanning tunneling microscopy/spectroscopy (LT STM/S) in addition to other surface sensitive techniques that are used in some parts, the next chapter explains the basic principles of these techniques. Furthermore, it shows the instrumentation of the LT-SPM system by which the major part of the results included in this dissertation are acquired. Moving to the results part which starts from the third chapter, it presents the use of on-surface reactions to control the stereospecific bonding of sulfur-containing organic nanostructures coordinated by Au atoms.

Subsequently, chapter 4 presents insights of the use of on-surface chemistry to explore pyrene-based molecules with alkyne/alkyne-halogen functionalization groups. First it shows how the alkyne coupling reactions can be changed in presence of on-surface synthesized metal-organic complexes. Then it describes the various coupling possibilities when both halogen and alkyne are present at the precursor pyrene molecules.

The last results chapter, chapter 5 describes acenes, starting from differently functionalized heptacene, it reports how we can achieve and characterize the different on-surface reaction intermediates and the end-product heptacene. The second part focuses on the use of sp^3 carbon atoms within the on-surface generated functionalized pentacene molecule for the creation of molecule-substrate barrier featuring a self-decoupling system. And the third part of this chapter shows how the functionalized anthracene coupling reactions and consequently the electronic properties change as we move from Au(111) surface to Au(110)-(2×1) surface.

Chapter 2

Principles, methods, and techniques

2.1 Introduction

This chapter descriptively defines the basic concepts and the operation methods for the various surface-sensitive techniques used in this project. To start with, the ultra-high vacuum (UHV) environment -in which reactions are achieved and products are characterized- is discussed. Then the operation principles and both theoretical and experimental methods employed in the following chapters are described.

2.2 Ultra-high vacuum

One of the major differences between conventional chemistry and on-surface synthesis is the reaction environment. Wet chemistry is a really mature discipline that has allowed the production of numerous functional compounds in life and industry. The evolution in the field of nanotechnology with its wide sub-fields, specially molecular electronics, demands for novel materials with tunable physicochemical properties and high level of precision in their design. The combination of conventional wet chemistry with on-surface synthesis opens new doors to the creation of otherwise unfeasible materials with extremely interesting properties.

In addition, the ultra-high vacuum environment normally used in on-surface synthesis, allows for the synthesis of materials that would not be stable in different conditions. Furthermore, UHV is also critical for the characterization of these materials using the various surface-sensitive characterization techniques that can only be applied under UHV conditions. Besides, a proper study of the chemical and physical properties of the reaction product requires -in most of surface characterization techniques- the absence of other materials as they commonly perturb the measurement and may hinder their proper interpretation.

2.3 Scanning tunneling microscopy and spectroscopy

2.3.1 STM imaging basics

In the classical picture of physics, there are minimum requirements to have a current flow within an electrical circuit. These requirements include the source, the switch, the resistor and the wires closing the loop. This implies that there is no chance for current to flow in the open loop (also known as open circuit) scenario. However this is not the case when considering the quantum picture. More explicitly, there can be a current flow already when two electrodes are not yet in contact but sufficiently close. The effect is known as "quantum tunneling" and the resulting current is then called "tunneling current". This "tunneling" results from the wavelike nature of electrons, which are quantum mechanically understood to have both particle- and wave-like

properties. This electron tunneling concept has led to revolutionary development in surface science after the invention of scanning tunneling microscope by Gerd Binnig and Heinrich Rohrer⁵⁰ in 1981, providing the first images of surface atoms and few years later in 1986 winning the Nobel prize in physics for this groundbreaking invention.

Using a sharp metal tip of a conductor in an xy scanning motion over a conductive surface at very close tip-sample distances ($z \approx 1$ nm), the tunneling current I_t is maintained while scanning by regulating the distance z and the xy motion using a piezo scanner tube (as shown in Figure 2.1), allowing for recording the topography of the surface in the so-called "constant current" operation mode.

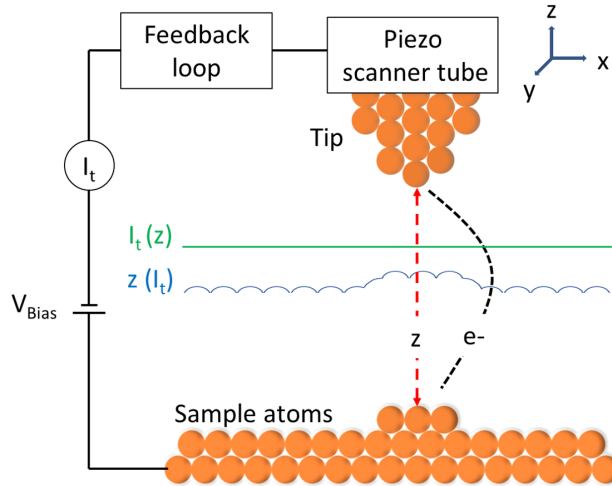


Figure 2.1: Schematic drawing of STM imaging modes, the measured tunneling current " I_t " is maintained by the the feedback loop to record the topography " z " signal in the typical constant current operation mode. Constant height mode is shown in brackets.

Another operation mode is the "constant height" mode in which the z distance is maintained by deactivating the feedback loop, and the I_t signal is recorded while scanning. Efficient and fast atomic resolution imaging can be performed on various surfaces, under different ambiances.⁵¹ However, for imaging single molecules with bond-resolution (BR-STM) there are necessary conditions. In addition to vibration isolation (*e.g.* using damping system and suspension springs) ultra-high vacuum and temperature ranges of a few Kelvin are crucial. The BR images are typically acquired with CO functionalized tips operating at constant height mode, which requires a great stability of the system. This is achieved with low temperatures that damp all the kinetic movements.

Another extremely important role for the liquid Helium temperature ranges is the energy resolution when performing scanning tunneling spectroscopy measurements, since the measured signals, whether stemming from inelastic electron excitations, Kondo effects or molecular orbitals are otherwise thermally-broadened at higher temperatures.

2.3.2 STM theoretical aspects

Theoretically, the STM tunneling is a complex technique, and to take all whole parameters into account is an extremely challenging process. Derived from first-order perturbation theory, Tersoff and Hamann⁵² presented a description for the tunneling current between two electrodes as:

$$I_t(V) = \frac{2\pi}{\hbar} e^2 V \sum_{\mu\nu} |M_{\mu\nu}|^2 \delta(E_\nu - E_F) \delta(E_\mu - E_F) \quad (2.1)$$

where V is the applied bias voltage, e is the elementary charge of electron, \hbar is the reduced Planck's constant, $M_{\mu\nu}$ is the tunneling matrix element between ψ_μ and ψ_ν states of the tip and the surface respectively,⁵³ while E_μ is the energy of ψ_μ in the absence of tunneling and E_F is the Fermi energy. Using an ideally spherical-tip scenario, with a radius R and the sphere being centered at r_0 and s -wave tip wavefunction, equation (2.1) can be approximated as:

$$I_t(V) \propto V \rho_t(E_F) e^{2kR} \sum_{\nu} |\psi_{\nu}(r_0)|^2 \delta(E_{\nu} - E_F) \quad (2.2)$$

Where $\rho_t(E_F)$ is the tip density of states, k is the inverse decay length in the vacuum barrier, with m_e being the electron mass, ϕ_{eff} is the effective barrier height (local workfunction):

$$k = \sqrt{\frac{2m_e \phi_{eff}}{\hbar}} \quad (2.3)$$

and

$$\sum_{\nu} |\psi_{\nu}(r_0)|^2 \delta(E_{\nu} - E_F) = \rho(\vec{r}_0, E) \quad (2.4)$$

is the surface local density of states LDOS. Then the tunneling current is proportional to the surface LDOS:

$$I_t(V) \propto \rho(\vec{r}_0, E) \quad (2.5)$$

This approximation is however extremely simplified since it is only valid for very low bias voltage regimes and spherically-shaped STM tip. A more generalized picture at finite bias voltage V , with the tunneling current I_t as a function of the integrated states between the tip and the surface bias window, and a weighted factor of the transmission coefficient,^{54,55} thus I_t can be rewritten as:

$$I_t(V) \propto \int_{E_F}^{E_F+eV} \rho_t(E - eV) \rho_s(E) T(z, E, eV) dE \quad (2.6)$$

where ρ_t and ρ_s are local density of states of the tip, and the sample respectively, $T(z, E, eV)$ is the transmission coefficient, as shown it clarifies the tunneling current dependence on the tip-sample distance z , the energy E and the applied bias voltage V . In summary with this more realistic picture, the tunneling current is a function of the LDOS of the tip and of the sample, and the transmission coefficient. First-order approximations of this picture consider ρ_t and T to be constant, for small bias values, so I_t can be approximated to be proportional to ρ_s integrated within $(E_F, E_F + eV)$ window of energy as shown in Fig. 2.2.

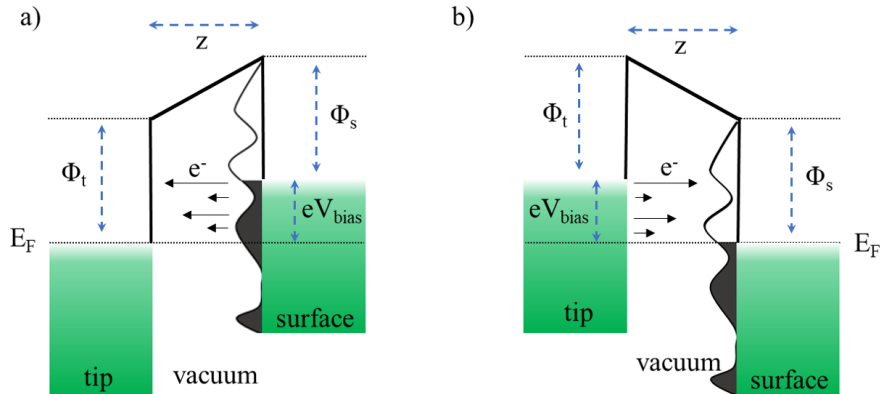


Figure 2.2: Schematic drawing of the tunneling process in the STM: a) at positive sample bias where electrons tunnel from occupied surface states towards the tip through the vacuum barrier z , and b) at negative sample bias where occupied tip states tunnel through vacuum to the unoccupied surface states.

Black arrows length is proportional to the transmission barrier coefficient at a certain energy eV_{bias} .

2.3.3 Scanning tunneling spectroscopy

From the dependence of the tunneling current I_t on the tip-sample distance z and the bias voltage V as shown in Eq. 2.6 and Fig. 2.2, scanning tunneling spectroscopy (STS) measurements aim to show the relation between these parameters by fixing one and measuring the dependence of the other two. Various information can be acquired in each measuring mode:

1. I-z curves with the V constant measure the current dependence on the z variation, providing information on the local work function (also know as the effective barrier height),^{56,57} which is closely related to the Kelvin probe force microscopy KPFM measurements using atomic force microscopy AFM.
2. V-z curves show the variation in the tip-sample distance by changing the bias at constant I.
3. The typical STS mode is the I-V mode with the z constant provides information on the conductance variations by ramping the bias and measuring the tunneling current at constant z.

Commonly, the differential conductance (dI/dV) is measured in the I-V mode, which is a good approximation of the local density of states LDOS at a specific energy eV , with V being the bias applied between the tip and the surface. The dI/dV relation can be obtained by the derivative of Eq. 2.6 with respect to the bias V:

$$\begin{aligned}
\frac{dI}{dV} &\propto \rho_t(E_F)\rho_s(E_F + eV)T(E_F + eV, eV, z) \\
&+ \int_{E_F}^{E_F+eV} \rho_t(E - eV)\rho_s(E)\frac{dT(E, eV, z)}{dV} dE \\
&+ \int_{E_F}^{E_F+eV} \rho_s(E)\frac{d\rho_t(E')}{dE'}T(E, eV, z) dE
\end{aligned} \tag{2.7}$$

Using the first approximation of considering ρ_t and T to be constant at low bias, the two integrals in Eq. 2.7 vanish and then:

$$\frac{dI}{dV} \propto \rho_t(E_F)\rho_s(E_F + eV)T(E_F + eV, eV, z) \tag{2.8}$$

Often in dI/dV , measurements lock-in modulators are used to superimpose a high-frequency sinusoidal bias signal (V_{ac}) to the constant dc bias. This oscillation generates a sinusoidal response in the tunneling current I_t . The derivative of this modulated current signal dI/dV is is proportional to the local density of states. For small V_{ac} signal:

$$V_{ac} = V_{osc}\sin(\omega t) \tag{2.9}$$

and the modulated current can be written as:

$$\begin{aligned}
I(V_{bias} + V_{osc}\sin(\omega t)) &\approx I(V_{bias}) + \frac{dI(V_{bias})}{dV}V_{osc}\sin(\omega t) \\
&+ \frac{dI^2(V_{bias})}{dV^2}V_{osc}^2\sin^2(\omega t) + \dots
\end{aligned} \tag{2.10}$$

Inelastic electron tunneling spectroscopy IETS acquired as the second derivative dI^2/dV^2 vs. V spectra at the second harmonic of the lock-in oscillation amplitude provide information relative to the vibrational spectra of the molecules. However, dI^2/dV^2 measurements are extremely demanding as they require mechanical and acoustical noise vibrations' isolation, and very low temperatures (close to 0 K) for ideal energy resolution.

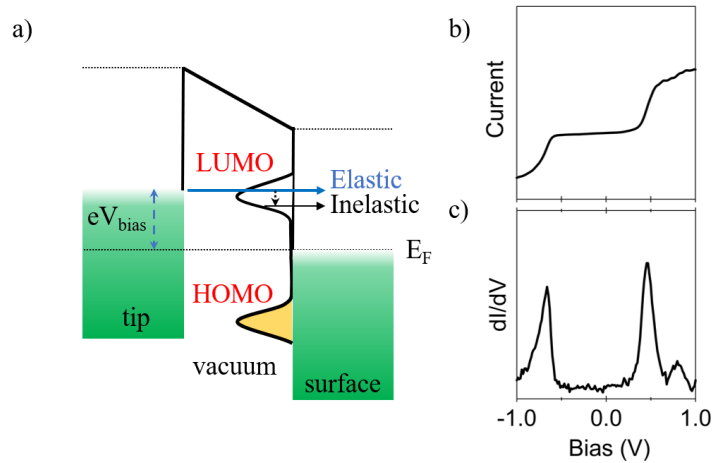


Figure 2.3: STS measurements illustration, a) at positive tip bias, electrons tunnel from the tip to the surface through the unoccupied molecular orbitals, b) example of I-V spectrum acquired with a lock-in modulator ($V_{osc} = 20$ mV), the change in the tunneling current slope is proportional to the LDOS, c) dI/dV conductance spectrum corresponding to the current curve in b, the current and dI/dV units are arbitrary.

2.3.4 SPM tip functionalization

Metal tip functionalization is an essential requirement for achieving bond-resolving of the chemical structures on surfaces. With this aim, several functionalization methods have been applied and proven successful. Leo Gross and *et al.* in 2009 demonstrated ultrahigh resolution of the chemical structure of pentacene on Cu(111) (Figure 2.4 c-d) using CO-functionalized tip of non-contact atomic force microscopy nc-AFM.⁵⁸ Following research in that direction showed metal tips terminated by *e.g.* Xe, Br, Cl,³⁵ N₂O,⁵⁹ and O^{60,61} to gain altered resolution of the molecular structures as well. At room temperature, Si and passivated Si tips are found to also acquire similar resolution.⁶² Molecules with larger sizes have also been employed for tip functionalization such as pentacene,⁵⁸ C₆₀ molecule,^{63,64} and naphthalenetetracarboxylic diimide NTCDI.⁶⁵ Still, the most popular functionalization of the metal tips for ultrahigh resolution imaging is CO for its high aspect ratio, chemical inertness (no interaction with the molecules being scanned at close tip-sample distances), ease of simulation of the tip since it attaches certainly with C bonded to the metal, and finally its lateral flexibility which provide the distinctly sharp signals at the bonds.

This level of resolution is not only limited to nc-AFM but can also be reached using STM, similarly in the repulsive Pauli force regime.^{66–70}

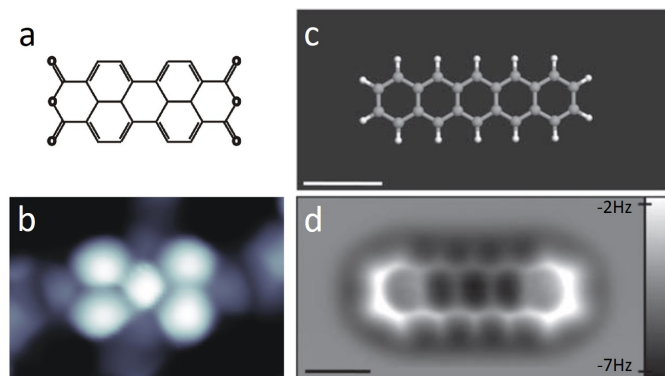


Figure 2.4: Bond-resolving SPM images with functionalized probes, a) chemical structure and b) constant height STM image of PTCDA molecule acquired with hydrogen functionalized tip. c) chemical structure and d) constant height nc-AFM image of pentacene on Cu(111) imaged by CO-functionalized tip, scale bar is 5 Å. Adopted a-b from ref. [66], and c-d from ref. [58].

The origin of the high-resolution when a probe particle is attached to the tip apex at close tip-sample distances in AFM and STM measurements is the strong lateral relaxations of the probe particle at the tip termination caused by Pauli repulsion. The functionalized tip acts as a nanoscale force sensor that responds by relaxation of the functionalizing particle towards the local minima of the tip-sample interaction potential regions. These lateral relaxation forces are converted into frequency shift signal in AFM and into tunneling current signal in STM case, yielding the sharp contrast features in the images.^{68,69}

2.3.5 The impact of tip character on molecular orbitals imaging

The wave function character of the STM tip plays an important role in the visualization and the realization of the molecular orbitals dI/dV measurements. From theoretical studies, Tersoff and Hamann have shown that for s -wave tips, STM images are approximated measures of the sample local density of states, given by the squared modulus of the sample wave functions.⁷¹ Then Chen found that for p -wave tips, STM images are relative to the spatial derivatives of the sample wave functions.⁷²⁻⁷⁴

Using tip functionalization methods as those mentioned in the previous sections can modify the tip character, and consequently impact the imaging of the sample we probe. Recent experimental works by Gross et al. [75] have shown that STM images with CO-functionalized tips to be a lateral gradient of the wave function with a significant contribution of the p -wave tip states, evidencing the theoretical findings by Chen. This study shows that significant tunneling current contribution to occur through the π_x and π_y orbitals of the CO molecule which features nodal planes normal to the sample surface.

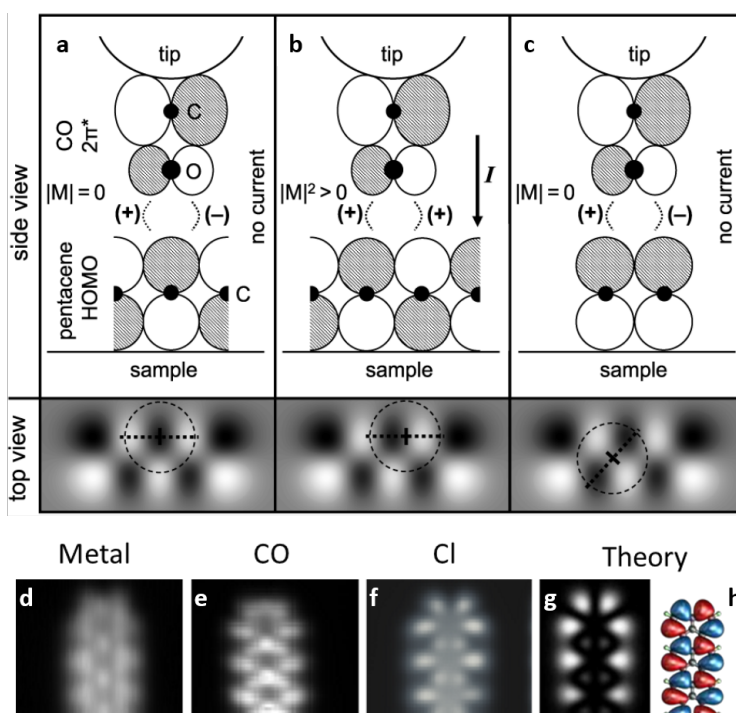


Figure 2.5: a-c) Schematic drawing of tunneling incidence between $2\pi^*$ molecular orbital of CO (tip) and a pentacene HOMO (sample), indicating in grey scale the different wave function signs, the dotted line in the lower panel indicate the position and orientation of the CO orthogonal cut planes, adopted from ref. [75]. d-f) Experimental constant height dI/dV maps of a 12 unit cell 5-armchair GNR zoomed at one end, mapped with metal tip, CO-terminated tip and Cl-terminated tip respectively. g) Simulated constant-height STM image and h) calculated shape of molecular orbitals wave functions of a free standing molecule corresponding to d-f.

In contrast, Cl-functionalized tips are found to show higher contribution from the p_z -wave states⁷⁶ with no nodal plane orthogonal to the surface, approximately resembling the s -wave tip scenario.⁷⁷ However, it is of a great importance to consider the tip character when interpreting

the STM images and comparing them to the theoretically plotted images. That is, LDOS images acquired using CO-tips possess a mixed sp -wave character with the relative contributions of the s - and p -waves changing as we change the imaging mode from constant current to constant height, typically, a significantly high p -wave tip character arises at constant current images using CO-terminated tip. This mixed sp -wave character of the CO-functionalized tip does not only depend on the tip but also on the lateral position of the sample, with the p -wave character increasing at the high lateral gradient of the sample orbitals, and the s -wave character increasing at the low lateral gradient positions of the sample.⁷⁵

Shown in Figure 2.5d-f the experimentally mapped orbitals at 70 mV of 5-armchair GNR, looking at the overall resolution, one can easily favor the maps taken by CO and Cl terminated tips over the one recorded with the metal tip. Comparing maps taken with CO-functionalized tip (Figure 2.5e) and with Cl-functionalized tip (Figure 2.5f), we notice their qualitative agreement at the molecule outer sides signal intensities. A closer look at the molecules' internal signals reveals the frequent maxima along the molecules' long axis in the CO-tip map while there is a nodal plane in the Cl-tip map. As we compare both to the theory results, excellent agreement between image acquired Cl-tip (Figure 2.5f) and the simulations in Figure 2.5g-h is evidenced.

This major difference on molecular orbitals mapping between CO-functionalized tips and Cl-functionalized tips arises from the crucial dependence of maps with CO-tips on the lateral variations of the sample wave function, with the relative contributions from the s - and p -wave characters varying accordingly (Figure 2.5a-c, e and h).⁷⁵ This is not the case when mapping with Cl-functionalized tip because of the absence of the nodal plane orthogonal to the surface and the s -wave character of the tip, showing no dependence on the sample wave function lateral variations, and offering a great functionalization alternative for mapping the molecular orbitals.

2.4 X-ray photoelectron spectroscopy

X-ray photoelectron spectroscopy (XPS), also known as electron spectroscopy for chemical analysis (ESCA) is a technique that allows studying the chemical composition of the surface. This technique is the most powerful and widely used for the aim of investigating the chemical states of materials within the first atomic layers of the surface, providing information about the composing elements and their chemical states quantitatively.

XPS is performed by irradiating the surface with a monoenergetic beam of soft x-ray photons of energy $h\nu$ and analyzing the energy of the emitted electrons, presenting the data as a spectrum of intensity (or electron counts or counts/second) vs. electron energy. Typical soft x-ray sources use Mg- $K\alpha$ or Al- $K\alpha$ radiation with photon energy of 1253.6 eV or 1486.6 eV respectively. The parameters involved in the XPS experiment are related as follows:

$$E_B = h\nu - E_K - \phi_s \quad (2.11)$$

where $h\nu$ is the x-ray photon energy, E_B is the binding energy of the atomic orbital from which the electron is ejected, E_K is the kinetic energy of the emitted electron, and ϕ_s is the spectrometer work function.

Since each element has a specific and unique set of binding energies, we can use XPS for identifying and quantifying the elements concentration on the surface. The binding energy variations (also known as the chemical shifts) result from chemical potential and polarizability changes of the compounds, rendering the ability of XPS to analyze the chemical state of the materials within the top few nanometers of the sample.

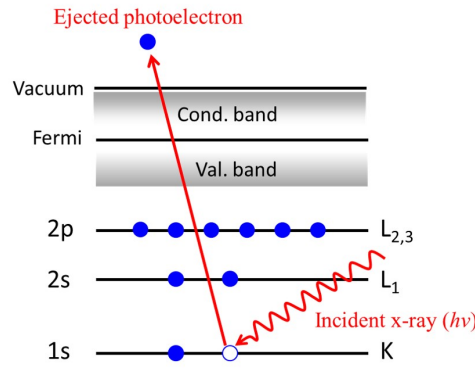


Figure 2.6: Schematic drawing of the ejection of K electron (1s electron) by the incidence of x-ray photons.

2.5 Low-energy electron diffraction

LEED is the technique that uses electron beams with low energy (typically in the order of 20 - 200 eV) to study the surface structure in reciprocal space from the diffracted electrons pattern. Analyzing the spot positions of these patterns provide quantitative information about size, symmetry and rotational alignment of the unit cell of the adsorbate materials with respect to the substrate unit cell. In turn, the intensity analysis of the diffracted beams as a function of the incident beam energy generate the so-called I-V curves, which in comparison to calculations may provide information about the accurate atomic positions.

Focusing on the diffraction process, de Broglie relationship describes an electron wavelength λ as a function of of the momentum p as:

$$\lambda = \frac{h}{p} = \frac{h}{\sqrt{2meV}} \quad (2.12)$$

where h is the Planck's constant, m is the electron mass, e is the electron charge and V is the the acceleration voltage (equals kinetic energy in eV). Therefore, for an electron with a kinetic energy of 150 eV, the wavelength is $\approx 1 \text{ \AA}$, which is similar to the interatomic spacing in a crystal and a necessary conditions for the observation of diffraction patterns coming from the atomic structure. In LEED, only elastically diffracted electrons contribute to the diffraction pattern, secondary electrons (lower energy electrons) are filtered out by the energy-filtering grids located in front of the fluorescent screen (see Figure 2.7 a). The mean free path of these low energy electrons is very short (few atomic layers), therefore, most elastic collisions occur at the topmost sample layers, making LEED highly sensitive to the 2-dimensional atomic structure of the sample surface.

To obtaine patterns from the elastically scattered electrons, the sample must be crystalline, with a well-ordered surface (or adsorbate) structure. Diffraction from a 2D surface in combination with the conservation of momentum can be expressed as:

$$k_{\parallel} - k_0^{\parallel} = G_{hk} \quad (2.13)$$

which in this case of 2D lattice concerns only the components of the wave vector (k) parallel to the surface, where k_0 is the incident wave vector, k is the scattered wave vector, and G_{hk} is the reciprocal 2D lattice vector. The reciprocal lattice vector G_{hk} is a set of points, having their coordinates defined by:

$$G_{hk} = ha^* + kb^* \quad (2.14)$$

where h and k are integers ($= 0, \pm 1, \pm 2, \dots$), a^* and b^* the primitive translation vectors of the reciprocal space, which are related to the primitive translation vectors of the real-space a and b by:

$$a^* = 2\pi \frac{b \times n}{|a \times b|}, \text{ and } b^* = 2\pi \frac{n \times a}{|a \times b|} \quad (2.15)$$

with n being a unit vector normal to the surface. From Equation (2.15) we can deduce that the reciprocal space vectors a^* and b^* lie in the same plane as the real-space vectors a and b , with a^*

perpendicular to b and b^* perpendicular to a . The vectors a^* and b^* have their lengths given by:

$$|a^*| = \frac{2\pi}{a \cdot \sin \angle(a, b)}, \text{ and } |b^*| = \frac{2\pi}{b \cdot \sin \angle(a, b)} \quad (2.16)$$

Note that the dimensions for real-space vectors a and b are [length], while for reciprocal space vectors a^* and b^* the dimensions are [1/length]. Figure 2.7 b shows the Ewald construction of diffraction from a 2D lattice.

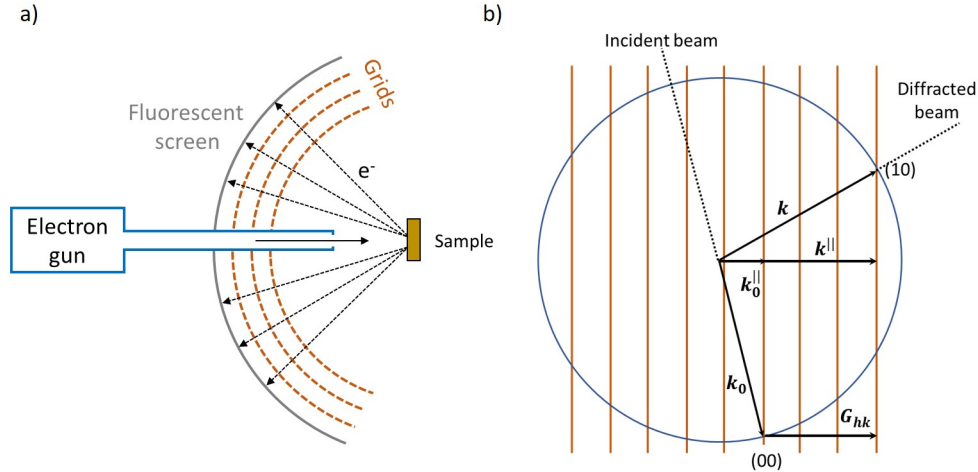


Figure 2.7: a) The typical experimental setup for LEED, b) Ewald sphere construction for diffraction from a 2D lattice, showing the momentum conservation $G_{hk} = k^{\parallel} - k_0^{\parallel}$.

2.6 Sample preparation

2.6.1 Sample cleaning

Metal single crystals of Au(111) and Ag(001) are normally cleaned by Ar^+ bombardment. Argon gas at partial pressure ranges of $3\text{E-}6$ mbar to $5\text{E-}6$ mbar are typically used. The gas is ionized in the sputter gun and the ions are accelerated towards the surface with a kinetic energy of 0.8-1.5 KeV to etch the first atomic layers of the surface on which typically the adsorbents exist. Using a resistive filament underneath the sample, it is then annealed to temperature ranges of 650-740 K for the desorption of whatever remaining impurities from the surface, and for the kinetic reorganization of surface atoms. These sputtering-annealing cycles may normally be applied several times until the surface is clean and flat. Au(110) single crystal is normally cleaned by applying sputtering conditions similar to those of Au(111) and Ag(001) but lower annealing to 575 K to maintain the homogeneous 2×1 surface reconstruction.

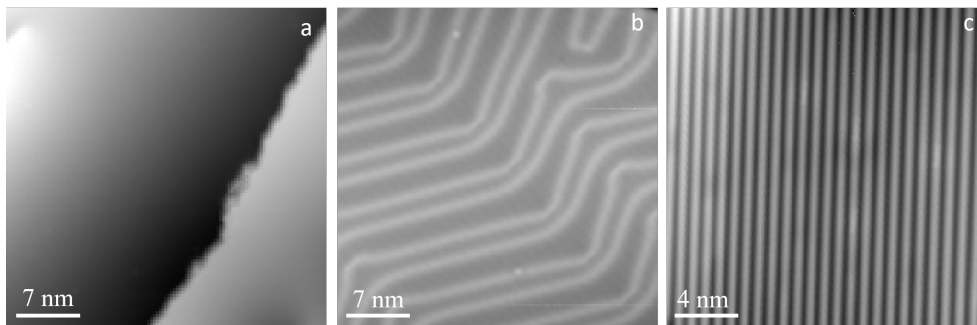


Figure 2.8: STM topography images of clean surfaces: a) Ag(001), b) Au(111) and c) Au(110). Imaging parameters: a) 1 V, 70 pA, b) -1 V, 300 pA, and c) 0.2 V, 100 pA.

2.6.2 Molecular deposition by thermal evaporation

After cleaning the metal surface, a custom-built Knudsen-cell evaporator is used to sublime the molecules on the facing clean surface. This is normally performed after calibrating of the molecular deposition rate with quartz crystal microbalance (QCM).

Molecular precursors used in this project are produced in solid-phase (molecules' powder) by collaborating synthetic chemists. Few milligrams of this powder is introduced into the pre-cleaned quartz (or boron nitride) crucible located in the evaporator. This process is carried out in atmosphere pressure. Figure 2.9 shows the structure of the custom-built evaporator during preparation at atmosphere pressure.

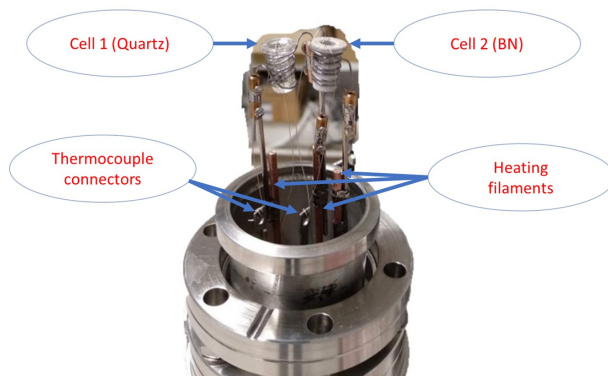


Figure 2.9: Custom-built double cell evaporator during preparation at atmosphere pressure. The two cells can be heated separately with thermocouples inside both of them for more accurate temperature reading.

The evaporator is subsequently attached to our preparation chamber and pumped down using an external turbo pumping station. The evaporator is then baked for > 10 hours. Afterwards, the molecules are also degassed for a couple of hours by heating the crucible using the resistive heating of the filaments surrounding each of them (see Figure 2.9) to temperatures close to the respective molecule's sublimation point. After the degassing process and at comparable pressures between the evaporator and the preparation chamber the gate valve separating the evaporator and the preparation chamber is opened and the evaporator is introduced. Evaporation rate is then calibrated by heating the molecules and monitoring their rate at the QCM. The evaporation rate and subsequently the coverage on the surface depend on the evaporation temperature (crucible heating), substrate temperature (sticking coefficient), the pressure of the chamber, the evaporator-sample distance, and the molecular mass. Once a stable rate is reached, the temperature is used as the reference evaporation temperature and the coverage of deposited material on the surface can be adjusted by changing the deposition time. Table 2.1 reports the sublimation temperatures for the different molecular precursors used in this project, as measured with type K (chromel–alumel) thermocouples located inside the crucibles.

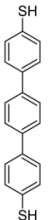
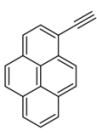
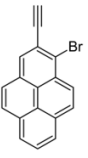
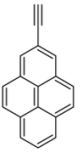
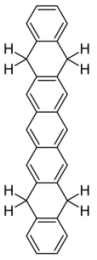
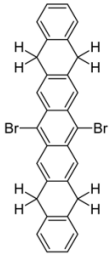
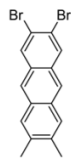
Chemical structure							
T_{evap} (K)	380	300	358	300	453	523	385

Table 2.1: Chemical structure and evaporation temperature T_{evap} for the molecular precursors used in this project.

Depending on the targeted products on surfaces, some samples are post-deposition annealed to trigger on-surface reactions, deposition on the cold substrate by might be the case as well.

2.7 STM tip functionalization methods

For experiments requiring CO or Cl functionalization of the STM-tip, NaCl is normally deposited afterwards by sublimation at ≈ 780 K.

The sample is then transferred to the STM chamber, which is isolated from the preparation chamber by a gate valve. After cooling to 4.3 K, CO is deposited on the sample (while locked at its cool-down position). Afterwards, the sample is brought to its hanging position and the tip can be approached for measuring.

2.7.1 CO-molecules identification on various surfaces

The easiest way to realize the carbon monoxide molecules' appearance on the flat Au(111) and Ag(001) surfaces is to deposit CO on the surface partially covered by NaCl overlayer as mentioned earlier in this chapter. Using a sharp metal tip to scan over these NaCl islands renders small circular dips on the flat NaCl/flat metal surface at specific scanning parameters ($U_{bias} > 0.5$ V) indicating the position of the adsorbed CO molecules as shown in Figure 2.10 (upper panel). On NaCl/Ag(001), CO molecules appear similarly as on Au(111). While on the bare metal Ag(001), the appearance is shown as in Figure 2.10 (lower panel).

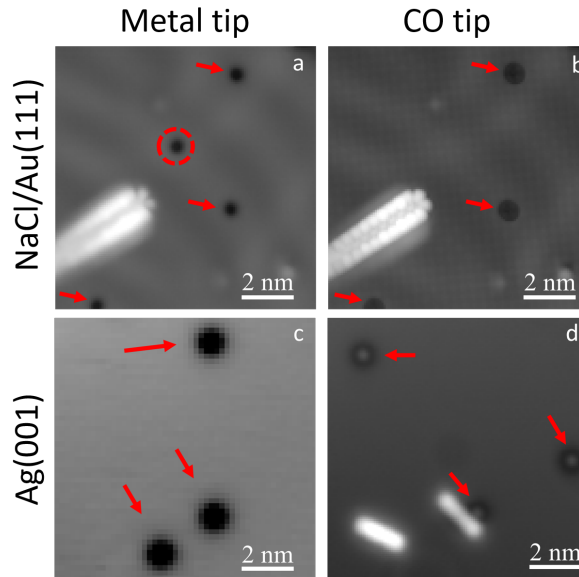


Figure 2.10: CO appearance on NaCl island on Au(111) as imaged by a metal tip a) and by CO-functionalized tip b). Red arrows mark the CO molecules while the dashed circle in **a** marks the picked CO to functionalize the tip to image **b**. **c** and **d**) CO appearance on the bare Ag(001) surface as imaged by metal and CO tips respectively. Constant current with imaging parameters: $V = 500$ mV, $I_t = 40$ pA for both **a** and **b**. **c**) $V = 1$ V, $I_t = 100$ pA, and **d**) $V = 50$ mV, $I_t = 100$ pA.

On the Au(110) reconstructed surface, CO functionalization of the tip is achieved directly and easily by directly from the bare metal surface, with no need to deposit NaCl as the visualization of the CO molecules is obvious along the rows of the Au atoms. Figure 2.11 shows the same frame imaging before and after functionalizing the metal tip with a CO molecule.

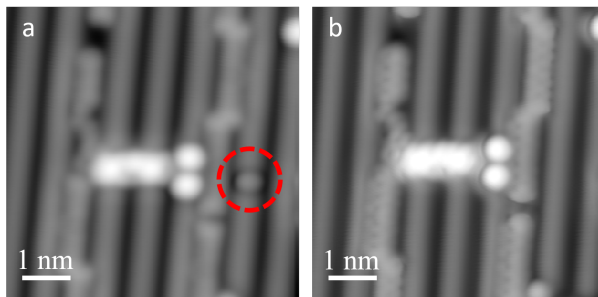


Figure 2.11: Constant current images of Au(110) region with metal tip a) and with CO-terminated tip b), marking the picked CO molecule in **a** with the dashed red circle. Imaging parameters: a) $V = -5$ mV, $I_t = 1$ nA, b) $V = -50$ mV, $I_t = 200$ pA.

2.7.2 Technical CO-functionalization methods

Herein, different CO picking practices used in the project are reported, those are:

1. Bias pulsing of -2 V for 500 ms after positioning the tip over the CO with feedback parameters of 100 mV/ 100 pA.
2. Scanning at higher currents (approximately 500 pA or higher) and negative voltages (-0.5 V to -1.5 V).
3. Freezing the scan line (in constant current mode) while scanning at ≈ -1 V, 100 pA, and approaching the z . A notable change in the z monitor after picking up the CO can be observed.
4. On Au(110), a more controlled functionalization can be performed using z -spectroscopy. That is, starting from feedback parameters of 50 - 100 mV, 50 pA, approaching the z by ≈ 450 pm. A clear change in the recorded tunneling current between the forward vs backward sweep hints the successful operation.

Getting rid of the CO from the metal tip apex without changing the metal tip is achievable and found to occur with high level of success by bias pulsing of $+2$ V for 500 ms (from starting feedback parameters of 100 mV/ 100 pA) on the clean metal regions. In most of the case, the same CO molecule can be found around within ≈ 10 nm from the pulsing spot, this allows for picking it up later if needed again *e.g.* after sharpening the tip or after performing measurements that require only-metal tips. This method is found to work for the three surfaces used in this project, Au(111), Ag(001) and Au(110).

2.7.3 Cl-functionalization of the STM tip

The impact of Cl-functionalization of the STM metal tips is more significant in the dI/dV mapping (Figure 2.5), as Cl-terminated tips do not feature the same flexibility to deflect and ultimately enhance the bond-resolution as in the case of the CO-terminated tips. However, the resolution of the former is still better than the standard STM metal tip (Figure 2.12).

To have a Cl-termination of the STM tip, we normally use z -spectroscopy on NaCl monolayers on either Au(111) or Ag(001) flat surface disabling the feedback at 100 mV/ 100 pA over the Cl and approaching by 350 pm, traces of the Cl vacancy within the island as a "hall-like" feature together with the resolution enhancement evidence the successful Cl functionalization. Figure 2.12 a-c shows the Cl functionalization as performed on Au(111). On Au(110), Cl-terminated tips can be achieved similarly by z -spectroscopy approaching the STM metal tip over the targeted Cl by 420 pm from starting feedback parameters of 20 mV/100 pA (Figure 2.12 d-e).

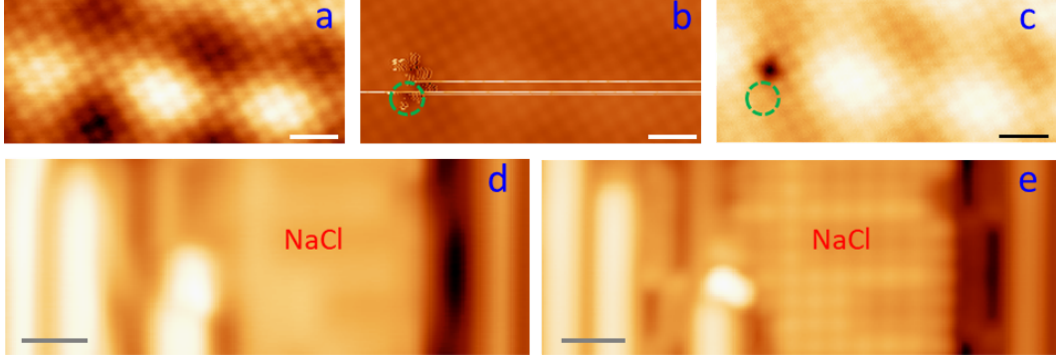


Figure 2.12: STM topography images for the Cl-functionalization of the STM tip showing samples with NaCl monolayer islands on Au(111) "upper panel" and on Au(110) "lower panel". (a) and (d) show the islands as imaged by a Pt/Ir metal tip, (b) shows the same frame in (a) as imaged with the same feedback parameters (50 mV/ 300 pA) after Cl-functionalization of the tip, the dashed green circles show the initial Cl vacancy position which seems to be changed after scanning (b), as imaged in (c) with the Cl-terminated tip at farther feedback parameters (500 mV/ 50 pA). On Au(110), (e) shows the post-functionalization imaging resolution change with respect to (d) with both frames scanned at the same feedback parameters (100 mV/100 pA). Scale bar is 1 nm.

2.7.4 High-resolution imaging and dI/dV measurements

Once the metal tip is CO-functionalized, bond-resolving images of the molecular structures can be acquired at STM constant height operation mode, opening the feedback loop over the flat molecular structure at bias voltage of 2-10 mV and tunneling current of 50-150 pA. To avoid potential loss of the CO or even tip crashing due to the feedback being disabled, these constant height images must be done over flat molecular structures and in the absence of objects that extend in z such as step edges.

For dI/dV spectroscopy and mapping of the sample, a digital lock-in (Nanonis) is used, operating at a typical frequency of 731 Hz, depending on the energy resolution expected from the orbitals, a modulation signal with amplitude of 1-20 mV is used.

2.8 Kondo temperature analysis methods

The Kondo temperature analysis is performed following the procedure described in reference [78]. In a first step, we correct for the broadening due to the finite tip temperature as proposed by Zhang et al. [79]:

$$w_{eff} = \sqrt{\Delta^2 - \Delta_{tip}^2} \quad (2.17)$$

With

$$\Delta_{tip} = 1/2 * 3.5k_B * T \quad (2.18)$$

Here, Δ is the half-width at half-maximum (HWHM) obtained from the fit to a Fano function and w_{eff} is the effective width. In a second step we correct for the broadening due to the lock-in oscillation by defining an effective temperature as proposed by Girovsky et al. [80]:

$$T_{eff} = (1/5.4k_B) * \sqrt{(5.4k_B T)^2 + (1.7V_{rms})^2} \quad (2.19)$$

Where, T_{eff} is the effective temperature, T is the measurement temperature and V_{rms} is the root mean square value of the lock-in oscillation voltage. In a last step, the Kondo temperature T_K is extracted fitting the effective width as a function of the effective temperature to the Fermi-Liquid model:⁸¹

$$w_{eff} = (1/2) * \sqrt{(\alpha k_B T_{eff})^2 + (2k_B T_K)^2} \quad (2.20)$$

2.9 Instrumentation

The machine used for the major part of this thesis is a low-temperature scanning probe microscope LT-SPM from Scienta Omicron (Figure 2.13), equipped with low energy electron diffraction LEED, Auger spectroscopy, residual gas analyzer RGA, quartz crystal microbalance QMB, sputter gun, and a double-stage manipulator.

The STM system is controlled by Nanonis electronics system, the measurement temperature ranges from room temperature, liquid Nitrogen temperature (77 K) and liquid Helium temperature (4.3 K). Ion getter pumps are distributed (one in the STM chamber and the other in the preparation chamber) to maintain a dynamic UHV pressure P environment, ($P_{STM(base)} < 1 \text{ E-11 mbar}$, $P_{prep(base)} < 5 \text{ E-10 mbar}$). A turbo molecular pump is used in the preparation chamber for sample preparation processes. PT/Ir wire is used for scanning the samples, usually sharpened by poking into the bare metal surfaces or by applying bias pulses. Bias voltage refers to the sample voltage with respect to the tip.

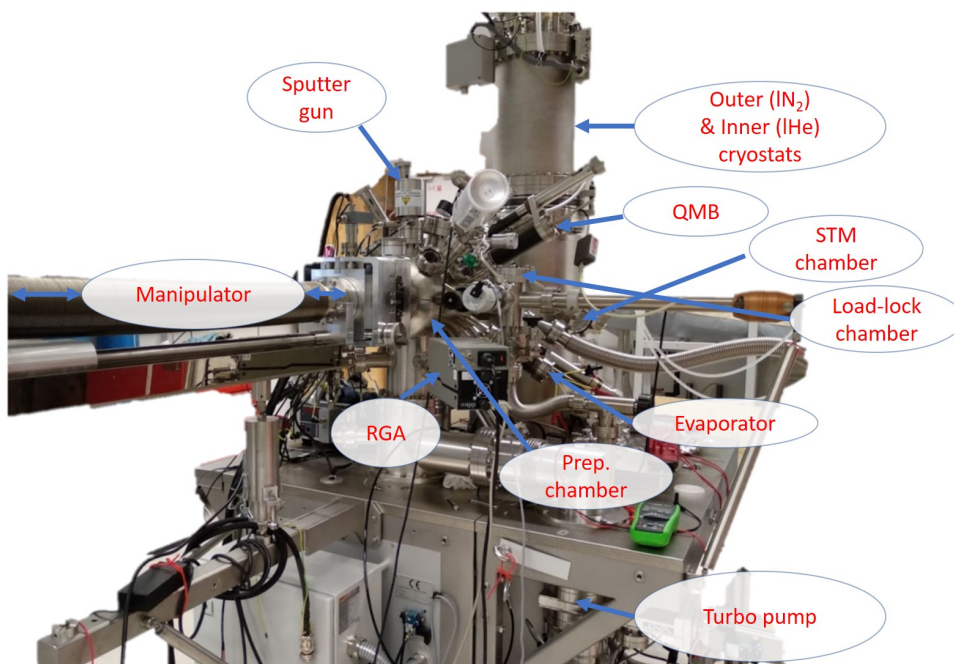


Figure 2.13: LT-SPM system (Scienta Omicron) with the apparent parts indicated.

Chapter 3

Metal-organic chemistry

Controlling the stereospecific bonding motif of Au-thiolate links

For the work included in this chapter, sample preparation, SPM measurements and data analysis were performed in collaboration with Luciano Colazzo, probe particle model simulations were provided by Aurelio Gallardo and Pavel Jelinek, Zakaria M. Abd El-Fattah performed the DFT and electron-boundary-element-method (EBEM) calculations, and José A. Pomposo provided the precursor molecules.

3.1 Introduction

The production of monolayers of sulfur-containing organic compounds on noble metals was readily recognized long ago to be of great interest for the development of functional interfaces.^{82–88} After decades of research, the interactions between organosulfur compounds and gold have in fact become textbook examples for strongly interacting metal–organic interfaces and the investigations on the interactions between organic sulfur, *e.g.* thiol (R-SH), and gold have shown a remarkable evolution with fruitful applications that span from biology^{89–92} to drug- and medical-therapy^{92–94} to materials science^{95–99} or nanoplasmonics.^{100–102}

Such a broad range of applications rely on the strong Au–S connection that occurs on the metallic surface. While the hydrogenated R-SH group would only weakly interact through coordination-type bonds with gold *via* the S lone pair electrons,¹⁰³ it is widely accepted that the Au–thiolate complex is formed after the dehydrogenation of the sulfhydryl group and the quenching of the resulting thiyl radical (RS•) with gold.¹⁰⁴ Small¹⁰⁵ or flat lying arenethioles¹⁰⁶ have provided excellent examples to explore the direct anchoring point of the Au–S connections by its visualization with scanning probe microscopy (SPM) and lately the use of multi-functional arylthiols has additionally demonstrated the possibility of using RS–Au–SR type bonding schemes to create extended and complex molecular networks on surfaces.^{107,108}

In this work, combining low-temperature scanning tunneling microscopy and spectroscopy (LT-STM/STS), low energy electron diffraction (LEED), core level photoemission (XPS) and molecular modeling, we not only provide a detailed picture of the whole formation process of Au–thiolates, with the associated impact on the underlying Au(111), but further show the means to control the resulting stereospecific RS–Au–SR anchoring motifs. Using 1,4-bis(4-mercaptophenyl)benzene (BMB, Fig. 3.1a) we can thus choose whether to form regular arrays of triangular nanopores of Au₃BMB₃ with a well-defined size of 1.8 nm side length or wires of poly-[S–Au–S–BMB–]_n. The nanoporous Au₃BMB₃ turns out to be thermodynamically more stable on the gold surface than its linear counterpart and causes 2D quantum confinement of the Au(111) surface electrons, an interesting effect more commonly studied on the surfaces of Cu(111)^{109,110} and Ag(111)^{111,112} than on those of Au(111).¹¹³

3.2 Results and discussion

A representative STM image obtained after deposition of BMB on the Au(111) surface held at 120 K is shown in Fig. 3.1a. Scattered BMB molecules and disordered molecular aggregates are observed. A closer inspection of the molecules reveals a variability of their appearance, in particular at their extremities. While three central lobes remain a common molecular trait and are depictive of a quasi-flat lying geometry of a terphenyl-core, the side lobes display two types of contrast, bright or dim (see the three different examples in Fig. 3.1aⁱ, aⁱⁱ and aⁱⁱⁱ). Such a behavior is associated with a partial dehydrogenation of the thiol groups (R-S-H) readily occurring during the condensation process. In line with a prior STM study on the thermal reactivity of benzenethiols on Au(111), the intact or undissociated thiol group is distinguished from the chemisorbed Au-thiolate (R-S-Au) by the characteristic bright and dim contrast, respectively, of the associated protrusions.¹⁰⁶ Thus, Fig. 3.1aⁱ, in which the terphenyl-core is sided by two bright lobes of homogeneous contrast, corresponds to the undissociated BMB molecule. Fig. 3.1aⁱⁱ shows a bis-mercapto moiety with bright and dim contrast on either side, in accordance with a partial molecular dehydrogenation. Finally, the molecule in Fig. 3.1aⁱⁱⁱ, sided by two dim protrusions, represents a fully dehydrogenated BMB. Noteworthy, isolated S atoms are also observed in Fig. 3.1a. The presence of these atoms will be further discussed below.

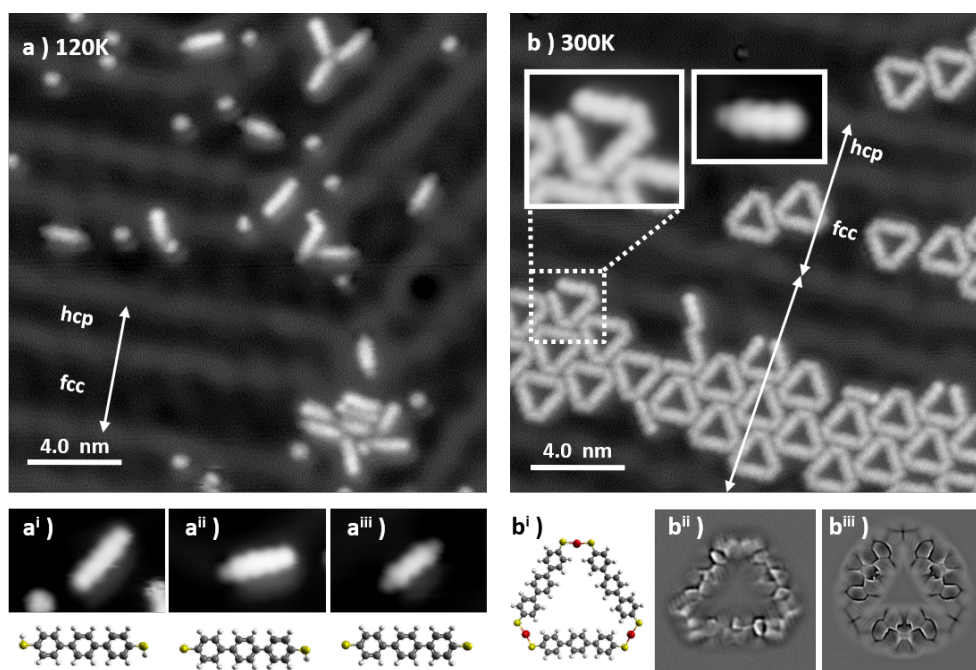


Figure 3.1: (a) As-deposited, unreacted BMB molecules, $20 \times 20 \text{ nm}^2$, $V = 30 \text{ mV}$, $I = 10 \text{ pA}$, $T_{depos} = 120 \text{ K}$; (aⁱ) close-up $3.0 \times 2.0 \text{ nm}^2$ of (a), and a molecular model of the fully hydrogenated BMB molecule; (aⁱⁱ) a close-up $3.0 \times 2.0 \text{ nm}^2$ of (a), and a molecular model of the partially dehydrogenated BMB molecule; (aⁱⁱⁱ) a close-up $3.0 \times 2.0 \text{ nm}^2$ of (a), and a molecular model of the fully dehydrogenated BMB molecule. (b) An aggregate of Au_3BMB_3 molecules obtained from (a) after annealing at RT ($20 \times 20 \text{ nm}^2$, $V = 210 \text{ mV}$, $I = 500 \text{ pA}$), with insets displaying close-up views of an open triangle and of a reactant molecule lacking a thiol/thiolate group on the right side; (bⁱ) a molecular model of an isolated Au_3BMB_3 complex and (bⁱⁱ) $3.0 \times 3.0 \text{ nm}^2$ Laplace-filtered constant-height STM image with a CO-functionalized probe ($U = 2 \text{ mV}$). (bⁱⁱⁱ) Laplace-filtered image of a probe particle model simulation of a Au_3BMB_3 complex. The reconstruction periodicity and the respective hcp and fcc sections are marked with arrows and labeled, respectively, for the as-deposited and thermalized sample, revealing the widening of the fcc sections and thereby the enhanced reconstruction periodicity for the latter.

The scenario changes completely when the sample is allowed to thermalize at room temperature (RT) and cooled again for imaging. Triangular shaped molecular units appear on the surface as isolated objects or as clusters, both lying preferentially on the fcc regions of the Au(111) surface reconstruction. The clusters aggregate with a moderate lateral ordering and appear closely packed on widened fcc regions of the herringbone reconstruction (see Fig. 3.1b).

Within the triangular complexes the sides are discernible as terphenyl-units, while the bright connectors at the three vertexes fit with the S–Au–S bonding motif displayed in the molecular model of Fig. 3.1bⁱ. In order to corroborate the bonding structure of these units, constant height measurements with a CO-terminated STM tip were performed. Fig. 3.1bⁱⁱ shows a representative Laplace-filtered tunneling-current image of an isolated triangular unit. Intramolecular features are clearly identified and reveal that, within each terphenyl side, the central phenyl rings appear distorted. This results from their tilt angle with respect to the surface plane, imposed by the steric hindrance with the neighboring rings. Importantly, each S atom of the mercapto-residue connects one Au adatom and generates a *cis*-type S–Au–S coordination. Here the question arises whether the Au adatom is extracted from the surface or captured from freely diffusing Au adatoms at RT. However, the fact that the average fcc/hcp period of the Au(111) herringbone reconstruction is increased or otherwise modified in this sample implies a lower compression of the reconstructed surface layer, which in turn evidences the extraction of Au surface atoms for the thiolate–Au complex formation.

Further proof that the terphenyl-sides are linked through thiolate–Au complexes and not *e.g.*, through disulfide bonds is obtained from theoretical calculations. Both options have been simulated and relaxed by DFT (Fig. 3.2), revealing a formation energy of the Au₃BMB₃ complex several eV more favorable than that of the BMB₃ structure due to the presence of covalent Au–S bonds. Besides, the Au₃BMB₃ structure shows an excellent agreement with the experimental images. Proof of it is found in the simulations with the particle probe model,⁶⁸ whose Laplace filtered image in Fig. 3.1bⁱⁱⁱ displays a notable similarity with the experimental data in Fig. 3.1bⁱⁱ. Particularly revealing is the presence of characteristic sharp edges at the presumable thiolate bonds of the Au₃BMB₃ structure due to the lateral relaxation of the CO-tip, which is completely missing in the case of the BMB₃ structure. From the total energy DFT simulations we can also deduce that the formation of strong covalent bonds between gold and sulfur atoms introduces a slight lateral distortion of the relatively soft BMB molecular units. These deformations are clearly visible in the high-resolution STM images acquired with the CO-tip.

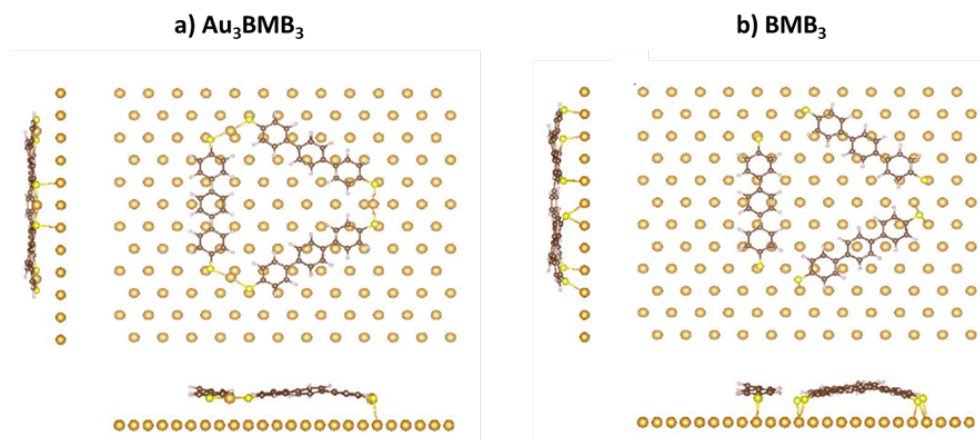


Figure 3.2: Top and lateral views of (a) the Au₃BMB₃ and (b) the BMB₃ relaxed structure. Both structures, were considered in DFT calculations. The formation of the structures connected by S–Au–S is found to be around 5 eV more favorable than the S–S linked one. The interaction between molecules in absence of adatoms is hard to attain, since the molecules tend to stay linked mainly with the substrate. This is reflected in the relaxed structure of three BMB molecules put close each other trying to form a BMB₃ compound by S–S linkers (Figure 3.2b). In this scenario the molecules repels each other and links the S atoms to the substrate, with a S–S distance of 4.77 Å in average, while the distance between the sulfur and substrate atoms is 2.58 Å in average. In addition, as readily commented in the text, the structure with S–Au–S links agrees much better with the structure observed experimentally.

It is also worth pointing out that, occasionally, incomplete triangles are found (Fig. 3.1b). A closer look at these metal organic complexes (see *e.g.* inset in Fig. 3.1b) evidences only three phenyl rings and the lack of a thiol/thiolate group at the open end, presumably associated with a thermal degradation occurring during the sublimation of the BMB powder. Similar findings can also be observed on single molecules like those in the second inset in Fig. 3.1b, clearly displaying three lobes associated with the three phenyl rings and a dim moiety on the left hand side attributed to

a thiolate group, but a lack of any thiol or thiolate groups at the right hand side of the carbon backbone. Indeed, following the deposition at 120 K, it was found that a large amount of elemental sulfur adsorbs on the Au surface. In addition to single atoms or few-atom clusters, numerous 2D sulfur islands are also generated (Fig. 3.3a). Combining STM and LEED on this sample (Fig. 3.3c and 3.3d) it was found that S adsorbs in the well-known $(\sqrt{3} \times \sqrt{3})$ R30 phase,^{114,115} not affecting the herringbone reconstruction of the underlying Au (Fig. 3.3b). This phase is known to display limited stability, which may be the reason why we are able to observe it only at 4.3 K after its condensation on the Au surface held at 120 K. Finally, by letting the system thermalize to RT and cooling again to 4.3 K for imaging, a complete desorption of the atomic sulfur and a transformation of the scattered single molecules into the triangular metal-organic complexes are observed.

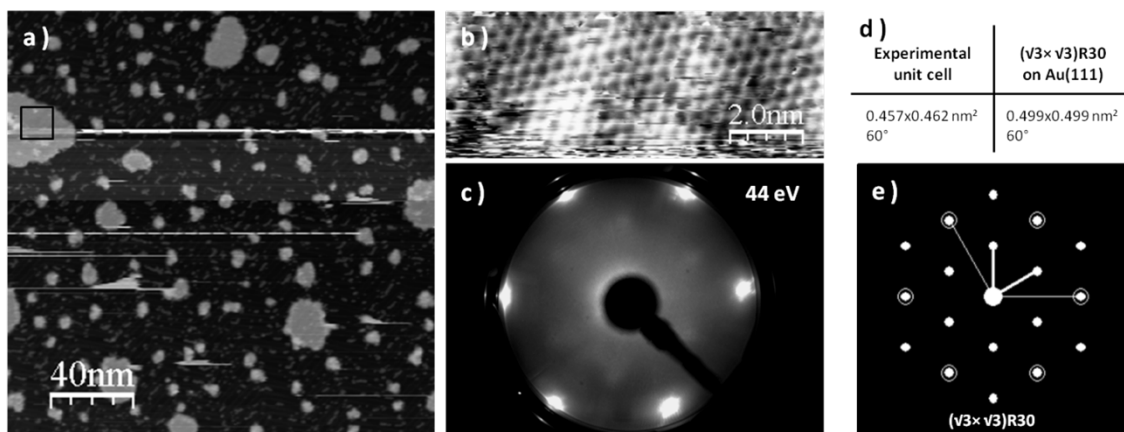


Figure 3.3: STM topography after the deposition of BMB molecules at 120K, $200 \times 200 \text{ nm}^2$, $V = 600 \text{ mV}$, $I = 25 \text{ pA}$. The black square on the left side of the image corresponds to b) STM topography of a S island $10 \times 4 \text{ nm}^2$, $V = -50 \text{ mV}$, $I = 40 \text{ pA}$ c) LEED patterns; d) comparison chart for the experimental S unit cell and the simulated $(\sqrt{3} \times \sqrt{3})$ R30 unit cell on Au(111) (substrate unit vector 0.288 nm) e) simulated LEED pattern of the $(\sqrt{3} \times \sqrt{3})$ R30 unit cell on Au(111).

Considering the stereochemistry of the molecular product obtained in the sub-monolayer regime, and in particular focusing on the S–Au–S connectors of the molecular structure, it is remarkable that the *cis*-configuration of the system, which allows the formation of the triangle, occurs with such high specificity. We have explored the possibility to stabilize the *trans*-conformation of the S–Au–S connections in order to generate linear chains of *poly*-bis-mercaptobenzene. The control over the stabilization of specific bonding configuration, *via* surface coverage or temperature, has been extensively reported in the literature.¹¹⁶ Examples include halogenated molecules^{117–119} or thiols^{107,108} on metallic surfaces. In particular the selective stabilization of chains or ring-shaped structures has recently attracted much attention in the field of on-surface chemistry as a way to perform precise surface nanopatterning.

In our case, to obtain linear chains, the molecular deposition has been performed with a high molecular flux (by increasing the deposition rate to 300 monolayers per h), low temperature (the Au(111) surface being held at 120 K) and full monolayer (ML) coverage. As can be observed from the bright termini of the BMB molecules (Fig. 3.4a,d), under these conditions the –SH groups remain intact and the Au(111) reconstruction underneath the molecular layer is not affected (Fig. 3.4a and 3.5aⁱ). The molecule’s bright ends attributed to thiol end groups disappear when the system is annealed to RT. Although in this temperature range the transformation of the overlayer into linear Au–thiolate chains does not occur quantitatively, the molecular arrangement loses its original periodicity and concurrently the surface morphology, *i.e.* the herringbone reconstruction, starts getting affected due to the cumulative extraction of surface atoms by the thiolates (Fig. 3.5b)

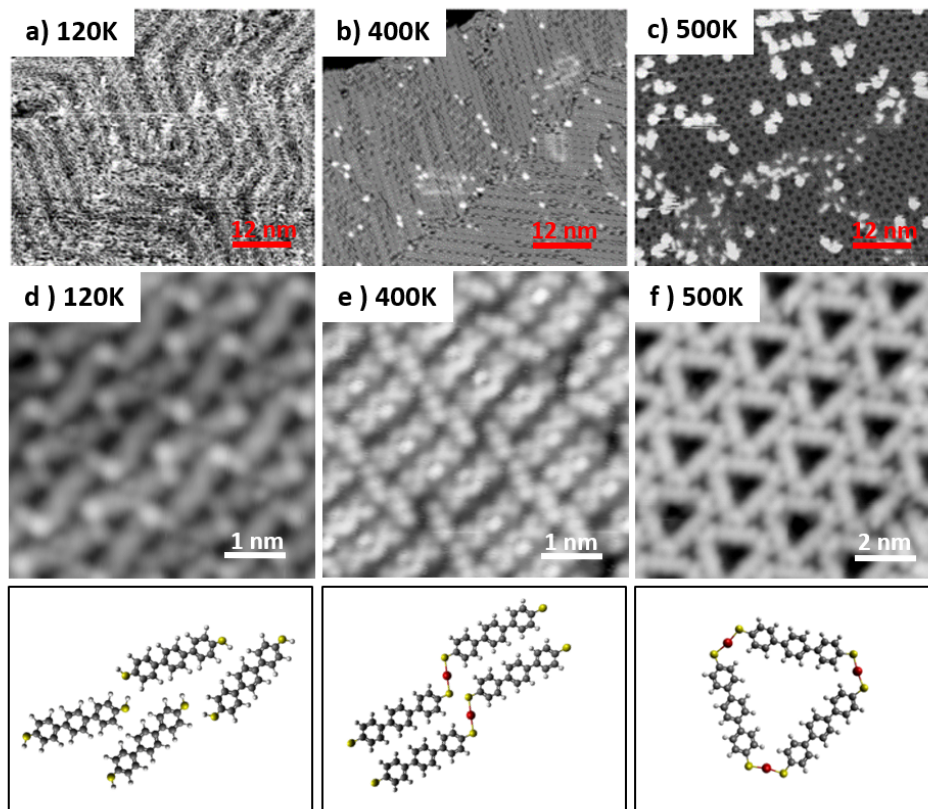


Figure 3.4: Formation of the linear $poly\text{-}[\text{S-Au-S-BMB}]_n$ at RT, in the high coverage regime and subsequent *trans*-to-*cis* isomerization into Au_3BMB_3 at higher temperatures on Au(111). (a,d) As-deposited ($T_{depos} = 120$ K), unreacted BMB molecules ($V = 50$ mV, $I = 80$ pA). (b,e) $poly\text{-}[\text{S-Au-S-BMB}]_n$ obtained from (a) after thermalization at RT ($V = -100$ mV, $I = 300$ pA). (c,f) Au_3BMB_3 obtained after annealing of (b) at 500 K ($V = -500$ mV, $I = 10$ pA)

Although XPS measurements employing Mg-K α or Al-K α radiation can be used for the study of sulfur-gold interactions,¹²⁰⁻¹²² most experiments do not provide data with sufficient signal to noise ratios to meticulously address tiny spectral features, especially if low coverages and small differences in chemical binding are concerned. In the low coverage experiment shown in Fig. 3.1, the extremely low density of the BMB molecule on the Au(111) surface would have made it virtually impossible to detect the molecular S 2p signal *via* Mg-K α radiation. Therefore, at this stage, XPS measurements on the high coverage experiment are used as complementary pieces of evidence supporting that the adsorption of BMB molecules on Au(111) at 120 K occurs with intact thiol functionalities before the thermally induced collective generation of Au-thiolate complexes. The as-deposited system at 120 K shows the S 2p_{3/2} peak at 163.3 eV (Fig. 3.5a) characteristic of physisorbed or unbound thiol groups.¹²³⁻¹²⁵ When the sample is annealed to RT an obvious chemical shift to lower binding energies is observed, namely 162.4 eV (Fig. 3.5b). This value is in agreement with several studies with different precursors regarding the RT formation of the Au-thiolate.^{108,125,126} As a result, the molecules now appear with dimmer termini in the STM images. It is worth pointing out that at 300 K the system is characterized mostly by BMB units with S atoms coordinating to surface atoms, but at the same time we observe the onset of the formation of linear BMB chains. This involves the ablation of Au-surface atoms. As a result, a notable deformation of the Au(111) herringbone reconstruction is observed. The number of dislocations along the reconstruction lines is reduced and their lateral periodicity increases to tens of nanometers (Fig. 3.5b²). Taking into account that the pristine herringbone reconstruction is formed by a high-density overlayer, Au atom ablation reduces its density and thus increases the reconstructions periodicity. By further increasing the annealing temperature the chemisorbed sulfurs no longer coordinate to surface atoms but extract them from the topmost Au layer converting them formally into adatoms (Fig. 3.4b,e). However, the virtually unchanged XPS spectrum of the sample after being annealed to 450 K (Fig. 3.5c) reveals that once the covalent S-Au bond is formed, the coordination to Au surface

atoms or to ablated Au adatoms results in S atoms with hardly distinguishable core levels. The associated STM images (Figure 3.5cⁱ) reveal that at this temperature the linear metal-organic complex is the dominant product and the herringbone reconstruction has been completely lifted. Also the onset of the formation of the triangular complexes is observed at 450 K. Such conversion is readily fulfilled at 500 K (Fig. 3.4c,f). The lower density of this phase denotes a substantial molecular desorption. Interestingly, the formation of small islands is observed concurrently with the phase change (Fig. 3.4c). We associate them with Au islands and rationalize their appearance as follows: the higher molecular density within the linear chains system induces the ablation of a higher number of Au atoms from the surface, compared with the triangular system. During the phase change, the desorbing molecules leave the ablated Au atoms behind, which causes the excess Au atoms to aggregate as islands. These islands display an apparent height around 0.25 nm, comparable to the height of a monatomic Au step (0.24 nm). Annealing above 500 K the molecular overlayer undergoes degradation and desorbs almost entirely. The XPS spectra thus become heavily attenuated. Besides, the onset of side reactions (formation of thioethers)¹⁰⁸ and the broadening of the spectra makes the identification of the sulfur species *via* XPS analysis impossible.

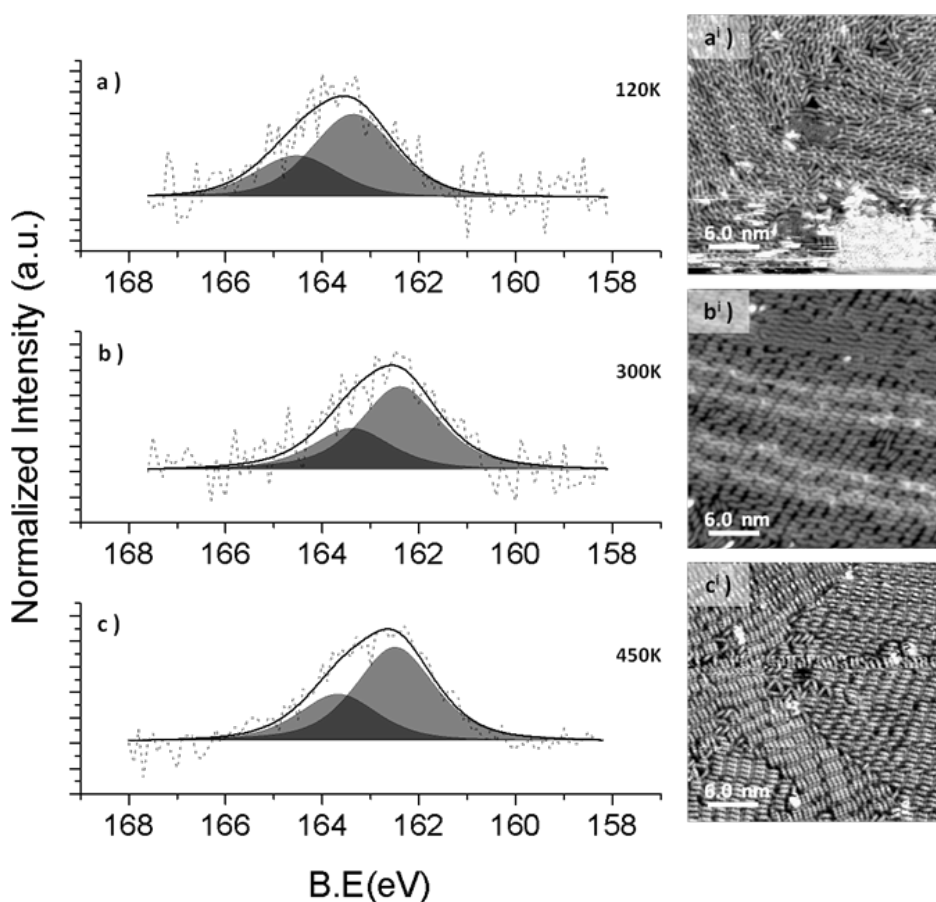


Figure 3.5: Mg-K α XPS spectra of S 2p acquired a) after deposition at 120 K b) after RT thermalization and c) after annealing at 450 K. The annealing steps were carried out on the same sample. S 2p 1/2 and 3/2 doublet fitted with a fixed energy separation of 1.18 eV. aⁱ) STM topography 30 \times 30 nm², V = -50 mV, I = 10 pA for the system deposited at 120 K and recorded at 4.3 K bⁱ) STM topography 30 \times 30 nm², V = -50 mV, I = 80 pA for the system thermalized at RT and recorded at 4.3 K and cⁱ) STM topography 30 \times 30 nm², V = -500 mV, I = 100 pA for the system annealed at 450 K and recorded at 4.3 K. The white arrows act as a guide to the eye denoting the herringbone reconstruction periodicity and revealing its enhancement as the Au adatom ablation sets in at 300 K.

Altogether, these experiments confirm the feasibility of our strategy to control the stereospecific bonding motif of Au-thiolates. We can use it to form linear chains that extend over several tens of nanometers, although their lateral order remains rather limited. This strategy is, however, strictly dependent on the coverage and temperature processing parameters. That is, the selective

formation of the linear thiolate isomers can be stabilized in a kinetic bottleneck by increasing the initial density of the precursors. However, the metastability of the trans-organometallic chain is revealed when the system is annealed at 500 K. These findings imply that the triangular complexes are more stable than their linear counterparts. To corroborate this hypothesis, we carried out total energy DFT simulations of linear and triangle structures and compared the formation energies of their 2D assemblies.

First, we compared the formation energies of a single 1D chain and triangle (see Fig. 3.6). Interestingly, the C–S–Au bond angles are similar, in both cases (and in the triangular complex calculated on Au(111)) ranging between 109.9° and 112.2° , but the individual chains turn out to be energetically slightly favorable by 18 meV per molecule. However, the situation changes when 2D assemblies are formed. After optimizing the lattice parameters for the free-standing assemblies, the binding energy per molecule turns out to be 230 meV larger for the triangle complexes. This indicates that it is the cumulative dispersion forces involved in the formation of the 2D molecular arrays which make the triangular aggregates substantially more stable than the chain-type aggregates.

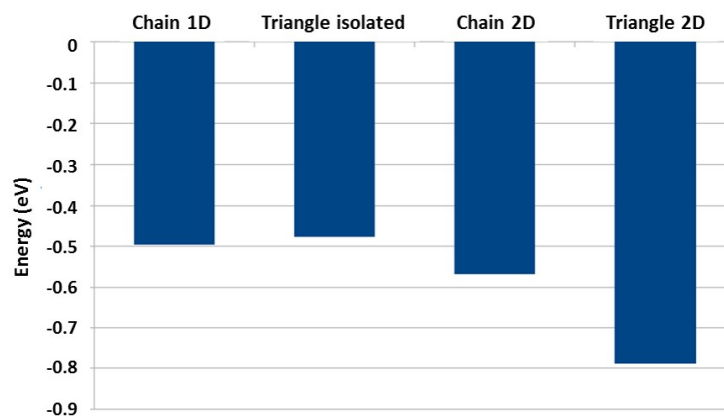


Figure 3.6: Formation energies per molecule calculated by DFT for linear and triangular complexes as single entities, as well as in 2D assemblies.

In order to describe the 2D crystal lattice periodicity and to extract the adsorbate unit cell, LEED analysis was performed on the thermodynamically stable network of triangular complexes. The triangular units adsorb on the Au(111) by adopting two configurations, namely “up” and “down” as shown in Fig. 3.7a and both phases, related by a mirror plane, are observed to segregate during the formation of the closely packed molecular arrays (see unit cell representations and the boundary region highlighted with the yellow zig-zag line in Fig. 3.7a). Each “up” and “down” configuration includes three rotational domains, making up for the presence of a total of 6 epitaxially equivalent domains. The LEED pattern shows as a superposition of all domains, since they are probed simultaneously during the analysis. We have simulated the diffraction pattern for a superlattice characterized by the epitaxial matrix $(8, 1/-1, 7)$, associated with a hexagonal unit cell with lattice vectors $a = 2.17$ nm and a 6.59° rotation with respect to the underlying substrate lattice, all in agreement with our STM images. In Fig. 3.7b and c the diffraction patterns have been simulated for each up and down configuration. Finally, when the two images are superimposed, an excellent fit with the experimental LEED pattern is obtained (Fig. 3.7d), confirming the commensurate epitaxy. The stabilization energy of the self-assembled long-range-ordered 2D nanostructures arises from the intermolecular interactions, as already evidenced in the calculations of Fig. 3.6 while a favorable interplay of molecule–substrate interactions ensures the commensurability of this molecular layer with the underlying Au(111) surface.

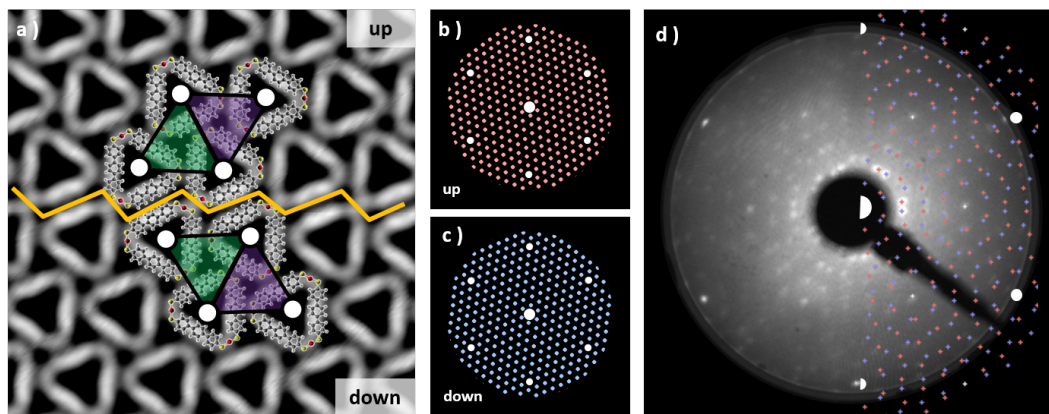


Figure 3.7: STM topography of a domain symmetry breaking of Au_3BMB_3 , $10 \times 10 \text{ nm}^2$, $V = 260 \text{ mV}$, $I = 400 \text{ pA}$. The yellow zig-zag line indicates the symmetry breaking region. Molecular models are superimposed on the STM topography and their mirror symmetry relation is indicated with a colored unit cell; (b) and (c) simulation of LEED patterns for the up and down domains, respectively; and (d) experimental LEED pattern at 51 eV with a superimposed LEED pattern simulation.

We have also probed the electronic properties of the Au_3BMB_3 complexes by STS and theoretical calculations, both on their metal-organic backbone and inside the pores. Regarding the former, Fig. 3.8b shows detailed density of states (DOS) calculations of fully optimized Au_3BMB_3 structures in a free-standing configuration (top) as well as adsorbed on Au(111) (bottom). The DOS of the free-standing complex displays well-defined orbitals, whose character is shown in Fig. 3.8a for the frontier states, involving unsaturated bonds in the coordination Au atoms that consequently appear around the Fermi level. Upon absorption on Au(111), the DOS appears broadened (Fig. 3.8b, lower panel) and the atomic orbitals of the complex Au atoms hybridize strongly with the surface atoms, causing an overall energy shift. However, the frontier orbitals are preserved and the same orbital character is now distinguished at lower energies (marked with arrows in Fig. 3.8b, bottom). The calculated DOS indeed shows a good agreement with our experimental data. On probing with STS on the terphenyl-units of the arms (black curve) we identify two clear resonances at 1.45 eV and +2.28 eV (Fig. 3.8e). Except for minor differences in energy due to size effects and the associated electron confinement,¹²⁷ the energies and local density of states distribution (Fig. 3.8d) very much resemble previous data on poly-para-phenylene on Au(111).¹²⁸ In contrast, spectra measured on the Au-thiolate connectors display a rather featureless signal, although evidencing a notable density of states within the previously mentioned terphenyl gap, including a shoulder around 0.7 eV (Fig. 3.8e). The corresponding conductance maps at 1.45 eV, 0.7 eV and +2.28 eV are shown in Fig. 3.8d. As mentioned above, while the maps at 1.45 eV and +2.28 eV resemble *poly-para-phenylene* orbitals,¹²⁸ the data at 0.7 eV reveal a spatially structured electronic density of states with the strongest weight around the Au-thiolate connection region. Notably, the three maps display a remarkable agreement with simulated dI/dV images (Fig. 3.8c) of the three frontier orbitals shown in Fig. 3.8a, providing a fully coherent picture of theory and experiment.

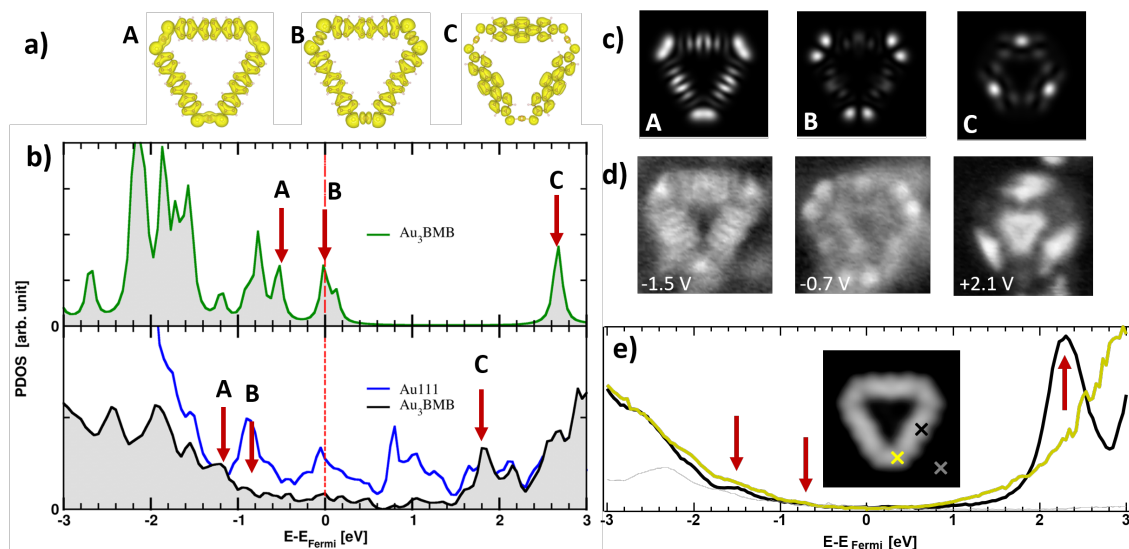


Figure 3.8: (a) Simulated frontier orbitals A, B, and C of an isolated Au_3BMB_3 complex. (b) Calculated density of states of a free-standing (top) and adsorbed (bottom) Au_3BMB_3 complex, marked with arrows the energies associated with A, B and C orbitals. (c) Simulated dI/dV maps of A, B and C. (d) Experimental dI/dV maps measured at -1.5 eV, -0.7 eV and +2.1 eV. (e) Experimental dI/dV point spectra ($V_{rms} = 15$ mV at 731 Hz, closing feedback parameters $V = 1$ V, $I = 200$ pA) measured on the terphenyl arm (black), Au-thiolate region (yellow), and reference spectrum on the substrate (grey), as marked in the inset by the colored crosses superimposed to the STM topography of an isolated Au_3BMB_3 on Au(111) (3.5×3.5 nm², $V = 50$ mV, $I = 100$ pA).

We now focus on the STS spectra recorded inside the pores. Interestingly, they reveal a substantially different signal from that detected on the bare Au(111) surface, in all cases evidencing the disappearance of the sharp Au(111) surface state onset at ≈ -0.48 eV (grey spectrum in Fig. 3.9c), and the concomitant appearance of a broad signal at higher energies. Fig. 3.9c shows a comparative series of representative dI/dV spectra within isolated triangular units and differently positioned units within a 2D island. The signal within the isolated triangles is a broad band centered around +200 mV (red curve), which we assign, in line with previous reports on porous networks,^{109–113,129} to electronic states associated with the confinement of the surface state electrons ($n = 1$ resonance). That is, the adsorbed Au_3BMB_3 complex acts as a scattering potential for the surface state electrons, which are thus confined into the nanopores and as a result upshifted in energy. However, there is also a certain transmission across such a scattering barrier, which partially accounts for the notable resonance width. Interestingly, when assembled into ordered arrays, these electronic states leaking through the confining barrier can couple with the states of the neighboring pores and end up forming well-defined bands.^{109,113,129} This effect can be nicely observed by comparing the previous spectrum with the spectra on regular complex arrays. The triangular complex at the island edge is sided by other complexes at two of its sides and leaves only one side leaking electronic density of states toward the bare Au(111) surface. As a result, the pore's density of states readily appears to be much better defined than that for the isolated triangle, but still utterly different from that of the following complex toward the island interior, surrounded by neighbors on its three sides. For such “bulk” complexes a much sharper and clearly structured density of states appears in between about -200 meV and 230 meV (displaying a strong maximum at 205 meV). As mentioned above, the electronic states at discrete energies within the pores couple, giving rise to bonding and anti-bonding states. For extended arrays, these form a continuous band whose bandwidth (limited by bonding and anti-bonding states at the low and high energy sides, respectively) is proportional to the interaction between the pores. Although much weaker, as shown in Fig. 3.9c and d, it is also possible to observe the following quantum well state centered around 0.55 eV.

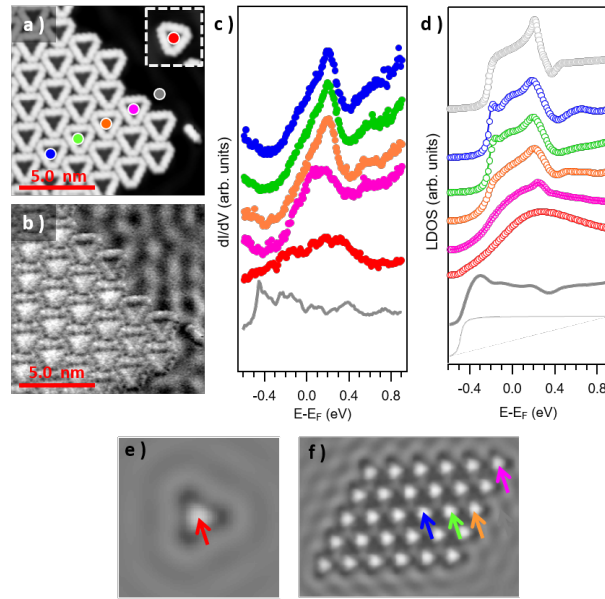


Figure 3.9: (a) STM topography of an array of condensed triangular Au_3BMB_3 complexes (a single complex is displayed in the inset) obtained after annealing at 450 K ($U = 210$ mV, $I = 400$ pA) and (b) the corresponding conductance map recorded simultaneously ($U_{osc} = 10$ mV at 731 Hz). (c) STS point spectra recorded inside the pores of the single triangle and of the triangles forming a condensed island, at the locations marked with the corresponding colored dots in panel (a) ($U_{osc} = 15$ mV at 731 Hz). (d) Simulated LDOS spectra at the pore center of an isolated triangle (red), of triangles displaying one (orange), two (green), and three (blue, violet) neighbors within a finite molecular island, and for an infinite network (light grey). The LDOS close to an island and for the pristine Au(111) substrate are shown in dark solid and light dashed grey, respectively. Spatially resolved LDOS map evaluated at the resonance energy ($E = 205$ meV) for (e) an isolated triangle and (f) a molecular island.

In order to quantify the degree of inter-pore coupling, *i.e.* the strength of the confining potential, we performed EBEM simulations for an isolated triangle and for a finite molecular array (Fig. 3.10). In the first approximation, we discard effective mass renormalization ($m_{eff} = 0.25 m_e$) and use the band minimum of the Shockley surface state on pristine Au(111) as the energy reference (EB = -0.485 eV). For a scattering potential of 0.6 eV, the onset of the surface state is upward shifted to -0.2 eV and the experimental resonance located at ≈ 0.2 eV is reproduced (Fig. 3.9d).

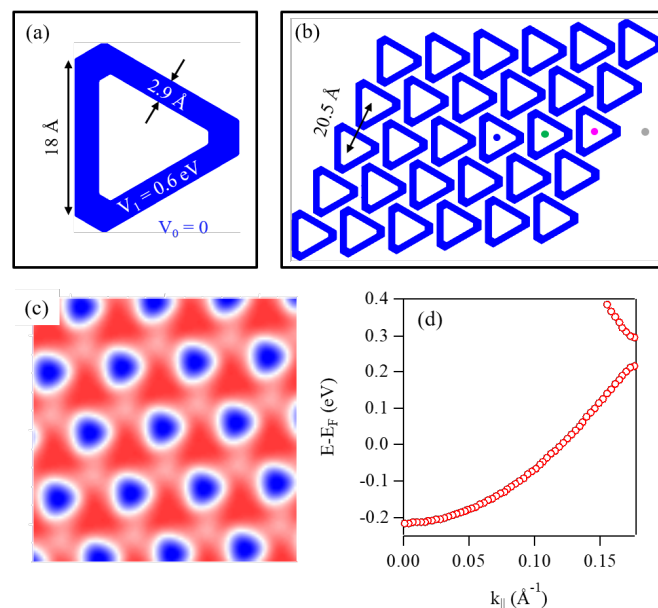


Figure 3.10: The geometries used for EBEM calculations for the (a) Single triangle and (b) a 5 x 6

molecular island. The white background stands for the Au(111) substrate, while the blue segments define the molecular backbone with a scattering potential of 0.6 eV. The molecular size and periodicity are indicated on the figure. The circles in (b) mark the location at which the LDOS's presented in Fig. 3.9 are taken. (c) The 2D-LDOS for an infinite network taken at the resonance energy ($E = 0.205$ eV). (d) The EPWE-calculated surface state dispersion for an infinite triangle network, showing a 80 meV gap opening at the zone boundary.

The LDOS on the substrate close to the molecular island is only slightly modified (dashed grey) with an onset that nearly coincides with that of the pristine Au(111) surface state (solid grey). The evolution/narrowing of the resonance width by going from an isolated triangle (red) to a complex at an island edge displaying one (orange) or two (violet) neighbors and eventually to the interior of the network (green and blue) agrees remarkably well with the experiment. Indeed, even for such a small island, the LDOS at the network's interior largely resembles the calculated one for an infinite network as obtained from EPWE calculations (black curve). The spatial distributions of the $n = 1$ pore state at the resonance energy for both a single triangle and a finite molecular island are presented in 2D-LDOS maps in Fig. 3.9e and f, respectively. The good matching between the LDOS obtained from EBEM and EPWE calculations allows the estimation of an 80 meV zone-boundary gap (Fig. 3.10).

3.3 Conclusion

In conclusion, we report the controlled formation of stereospecific RS–Au–SR bonding motifs allowing for the selective stabilization of linear or porous Au–thiolate isomers. The investigation of the formation mechanism of covalent S–Au bonds starting from physisorbed thioles has revealed that the selective stabilization of the thiolate isomers is strictly dependent on the surface coverage and temperature. The linear isomers are thermodynamically less stable than their porous counterparts but can be stabilized kinetically. Analysis of the electronic properties of the more stable porous arrays of Au_3BMB_3 has revealed that, besides the electronic states associated with the metal–organic backbone, the pores act as confinement barriers to the surface state electrons of the enclosed Au(111) patch. We can thus obtain 0-dimensional quantum dot states from single Au_3BMB_3 molecules, which can further couple into well-defined bands within extended ordered arrays of the Au–thiolate complexes. Interestingly, the finite size effects at the array's edges are unambiguously observed.

Chapter 4

Pyrene-based chemistry

Pyrene-based materials are a popular choice for organic electronics,¹³⁰ and quantitatively understanding the effects of changing their coupling allows the more precise design of future materials that can be tailored towards their applications. Importantly, the trends correlating the electronic and structural properties of the bonding motifs are also expected to apply to other organic materials. In the following two sections of this chapter, it is first reported a second-order on-surface reaction mechanism using a pyrene-based molecular structures functionalized with alkyne group, with the reaction yield impacted by the presence of a pre-synthesized metal-organic structure. Afterwards, it is addressed the role of the Br and alkyne functionalization on alkyne coupling reactions when both functional groups are present, and when only alkyne is present within the backbone of pyrene molecules. A detailed characterization of the electronic properties using STS point spectra and dI/dV maps is addressed .

4.1 Steering alkyne homocoupling with on-surface synthesized metal-organic complexes

For the work included in this section, sample preparation, SPM measurements and data analysis were performed in collaboration with Luciano Colazzo, calculations and probe particle simulations were provided by Aurelio Gallardo and Pavel Jelínek, and the precursor molecules were provided by José A. Pomposo.

4.1.1 Introduction

Metal-organic complexes are a class of compounds formed by organic building units linked by coordination to metal ions. These complexes are shown to be extremely versatile systems for many applications that include e.g. from biological and medical use¹³¹⁻¹³⁴ to hydrogen storage,^{135,136} CO₂ sequestration,¹³⁷ filtering¹³⁸ or catalysis.^{139,140} Their functionality frequently relies on the properties of the ligand and/or on their structure, which often forms long-range ordered porous frameworks (so-called metal-organic frameworks or MOFs). However, the catalytic activity is frequently determined by the metal centers. Despite the booming development of “on-surface synthesis” strategies, whereby chemical reactions are driven under the confinement of well-defined surfaces (often under vacuum conditions),¹¹⁶ the catalytic use of 2D metal-organic complexes to influence such surface-supported reactions has hardly been explored to date. In this work we study the effect of Au-thiolate structures (those synthesized in the previous chapter) on one of the most popular reaction schemes applied in on-surface synthesis: alkyne homocoupling.¹⁴¹ This is a particularly relevant reaction, among other reasons, because it results in conjugated structures and can thus be used in the synthesis of functional organic semiconductors.¹⁴¹

4.1.2 Results and discussion

In the previous chapter we reported how to control the stereospecific bonding motif in the formation of Au-thiolate links. Thereby, we could controllably form triangular Au-coordinated metal-organic complexes with 1,4-bis(4-mercaptophenyl)benzene (BMB) as organic ligands.¹⁴²

Now, we study their effect on the dimerization of 1-ethynyl-pyrene reactants and further compare the electronic properties of the different coupling schemes. Upon deposition of 1-ethynyl-pyrene (**m1**, Fig. 4.1.1a) onto Au(111) held at room temperature (RT) the molecules remain unreacted (Fig. 4.1.1b) and are found either as monomers (Fig. 4.1.1c) or as non-covalently bound dimers (Fig. 4.1.1d). The latter are clearly dominant, evidencing attractive intermolecular interactions that, however, do not drive formation of larger clusters. The dimers preferentially adsorb along the fcc trenches of the Au(111) herringbone reconstruction and display a clearly correlated inter-spacing along that one-dimensional confinement.

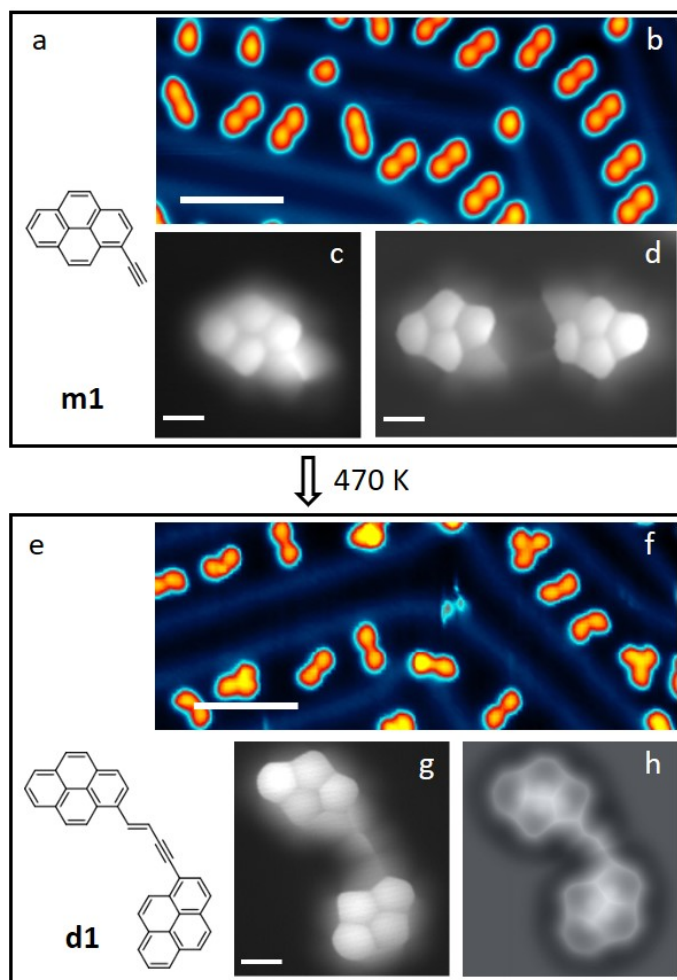


Figure 4.1.1: Visualization of conventional on-surface alkyne homocoupling on Au(111). (a) Chemical structure of the **m1** precursor. (b) STM overview of the sample after **m1** deposition on Au(111) held at RT. (c) High-resolution STM image with CO-functionalized tips of the monomer. (d) Similar image of a non-covalently bound dimer. (e) Chemical structure of **d1** product. (f) Overview image of the sample after annealing to 470 K. (g) High-resolution STM image with CO-functionalized tips of **d1**. (h) Particle probe model image simulation of **d1**. Imaging parameters and scale bars: (b) $U = 1.0 \text{ V/I} = 100 \text{ pA}$, 5 nm (c) $U = 2 \text{ mV}$, 3 Å (d) $U = 2 \text{ mV}$, 3 Å (f) $U = 0.5 \text{ V/I} = 10 \text{ pA}$, 5 nm (g) $U = 2 \text{ mV}$, 3 Å.

These findings are all reminiscent of those found with other comparably sized molecular systems, in which the dimerization was associated to attractive dipole–dipole interactions^{143,144} and the correlated inter-dimer spacing to electrostatic repulsion.^{143,145} As we anneal the sample to 470 K, the molecules react and couple covalently. Given the pronounced reactivity of the ethynyl group, the various types of reaction products all arise from alkyne homocoupling processes that result either in covalently bound dimers or trimers (Fig. 4.1.1e). Henceforth we will focus on the dimer structures. As known from previous reports, alkyne homocoupling can result in a variety of different coupling schemes.^{141,146} A particularly successful technique to determine the adsorbate’s covalent bonding structures at the single molecule level is scanning probe microscopy with CO-functionalized tips in the repulsive tip-sample interaction regime.^{34,58,147} Applying this imaging technique to the dominant dimer product in constant height scanning tunneling microscopy (STM) mode renders images as shown in Fig. 4.1.1g. From the non-linear arrangement of the “inter-pyrene” bonding motif and the lack of a mirror symmetry plane for the resulting product structure, dehydrogenative Glaser coupling can be discarded. Instead, the products can be assigned to structure **d1** (Fig. 4.1.1e), further supported by comparison to simulations with the particle probe model (PPM,

Fig. 4.1.1h).^{68,147} This structure stems from a non-dehydrogenative head-to-head alkyne coupling reaction^{29,141,146,148–150} and, surprisingly, all covalently coupled dimers share the same linking structure, whether in *cis* or *trans* configuration (Fig. 4.1.2).

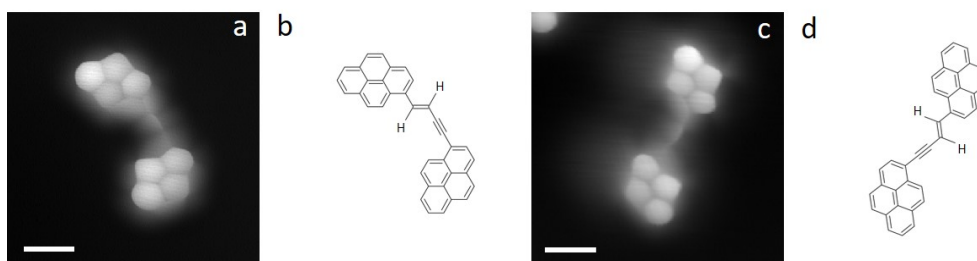


Figure 4.1.2: a,c) High-resolution STM images with CO-functionalized probes depicting the *cis* and *trans* dimer structures b,d) sharing the same coupling motif. For both a and c: $U = 2$ mV and Scale bars = 5 Å.

Note that, as opposed to non-contact atomic force microscopy (nc-AFM) imaging, in which the higher electron density at triple bonds makes them appear with higher contrast,^{34,147,151} in STM mode they appear as a nodal plane in the current signal (Fig. 4.1.1g)¹⁵¹ more obvious in the experimental data than in the PPM simulations. In the following we describe the changes in the reactivity of **m1** brought about by the presence of Au-thiolate-based metal-organic complexes. The Au₃BMB₃ complexes (Fig. 4.1.3b and c) are first formed, as described earlier,¹⁴² by deposition of BMB (Fig. 4.1.3a) on Au(111) held at RT.

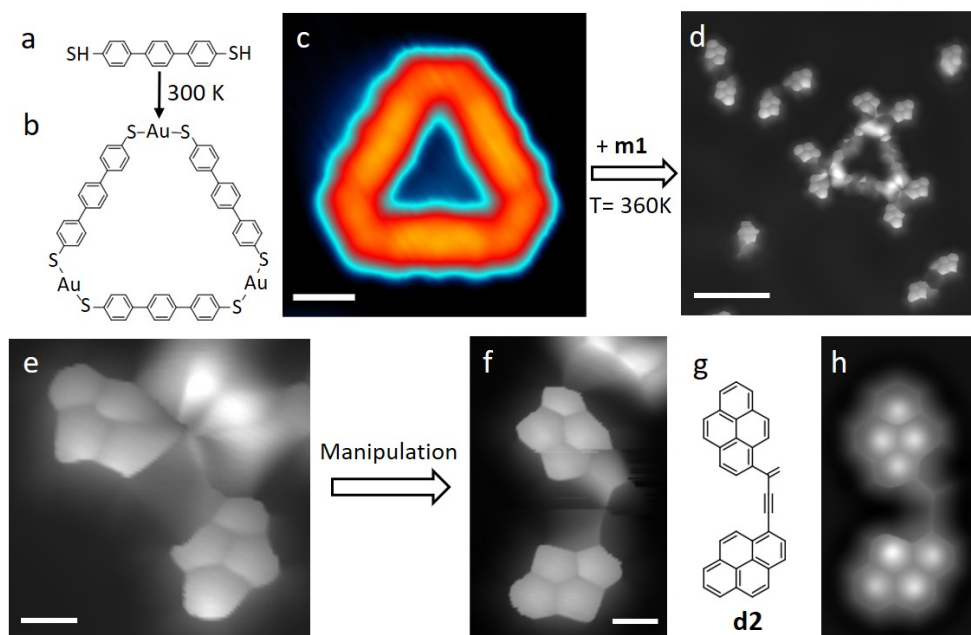


Figure 4.1.3: Steering alkyne homocoupling with on-surface synthesized metal-organic complexes. (a) Chemical structure of the BMB molecules and (b) chemical structure of the Au₃BMB₃ complex formed on Au(111). (c) Constant-height STM image of a Au₃BMB₃ and (d) **m1** sample after annealing to 360 K. (e) High-resolution constant-current image the **d2** dimer next to the metal-organic vertex and (f) after manipulating **d2** away from it. (g) Chemical structure of **d2**. (h) Particle probe model simulation of **d2**. Imaging parameters and scale bars: (c) $U = 150$ mV/ $I = 500$ pA, SB = 6 Å, (d) $U = 2$ mV, 2 nm, (e) $U = 2$ mV, 3 Å, (f) $U = 2$ mV, 3 Å.

Subsequently, the reactant **m1** is deposited and the sample is annealed. A representative image of the sample in vicinity of a Au₃BMB₃ complex after annealing to 360 K is shown in Fig. 4.1.3d. Whereas far from metal-organic complexes **m1** remains mostly unreacted (as illustrated by all the monomers and dimers that are not next to the metal-organic complex in Fig. 4.1.3d, as well as in the larger scale images of Fig. 4.1.4), next to Au₃BMB₃ the scenario is completely different, providing evidence for a reduced activation temperature in the covalent coupling reaction.

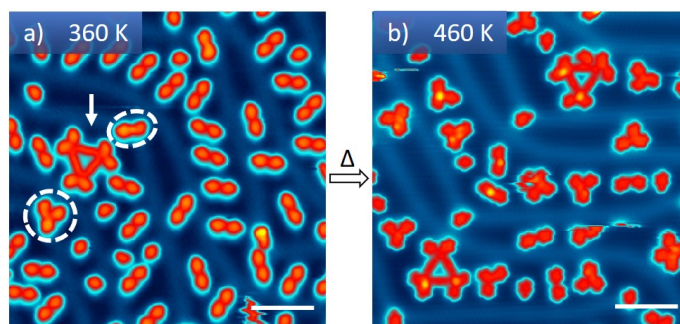


Figure 4.1.4: Larger scale STM images of sample with Au_3BMB_3 complexes and **m1** reactants after annealing to 360 K (a) and 460 K (b). It can be seen from the images that, at 360 K, all **m1** molecules remain unreacted, except the dimers directly at the metal-organic complex (marked with an arrow), as well as a nearby dimer and a trimer marked with the white ovals. At 460 K, as occurred in the absence of the metal-organic complexes, most reactants appear covalently bonded into dimers and trimers (occasionally even some tetramers).

A standing out observation is the remarkable tendency of the Au-thiolate vertices of the Au_3BMB_3 triangles to become decorated by pyrene dimers. High-resolution imaging with CO-functionalized probes, however, is greatly distorted by the proximity of the metal-organic vertex (Fig. 4.1.3e) and does not allow assigning a particular molecular structure to those dimers. As the distorting interactions of the CO with the metal-organic vertex are avoided by manipulating the dimers away from it, the high resolution imaging (Fig. 4.1.3f) eventually allows for the determination of the dimer's structure **d2** (Fig. 4.1.3g, note again the nodal plane in the current signal at the triple bond position), which results from a head-to-tail alkyne coupling^{148–150} and is further confirmed with PPM simulations (Fig. 4.1.3h) that nicely match the experimental data. However, one has to be sure that this manipulation process does not change the dimer's structure. To check this, we perform scanning tunneling spectroscopy (STS) measurements on the **d2** dimers before and after manipulation (Fig. 4.1.5). The unaffected dI/dV signal, which is proportional to the local density of states, provides evidence for the unchanged chemical structure.

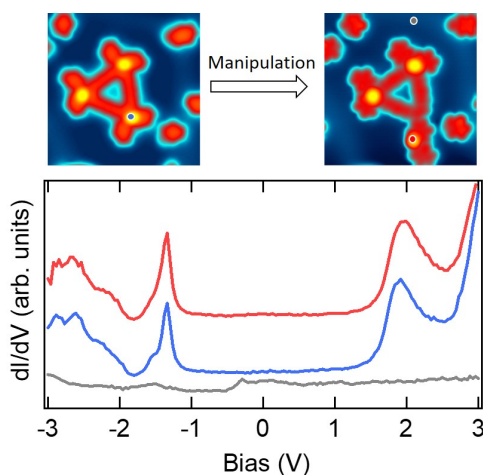


Figure 4.1.5: STM images of a **d2**-decorated Au_3BMB_3 complex before and after manipulation. The graph below shows the associated STS spectra of the **d2** dimer before (blue) and after (red) manipulation taken at the same position marked by blue and red dots on the images. The reference spectrum on the bare Au(111) surface is shown in grey.

This is further confirmed by the reversibility of the manipulation: the attractive interactions between organo-metallic vertex and **d2** often cause a spontaneous return of the manipulated dimer back to the vertex, resulting in a configuration that is indistinguishable from the starting point (Fig. 4.1.6). It is this attractive interaction which precludes the consideration of Au_3BMB_3 complexes as true catalysts. Although they lower the activation temperature for the reaction and thus increase the reaction rate, the products remain attached to the complex, not fulfilling a so-called catalytic cycle that should include the product's spontaneous detachment from the catalyst. It is worth noting that, whereas only one type of covalent coupling motif was found for the dimers on Au(111) in the absence of the metal-organic complexes, based on the analysis of 92 dimers at the Au_3BMB_3 vertices only 76% of them are **d2**. The remaining 24% are **d1** (no trimers are found next to the vertices).

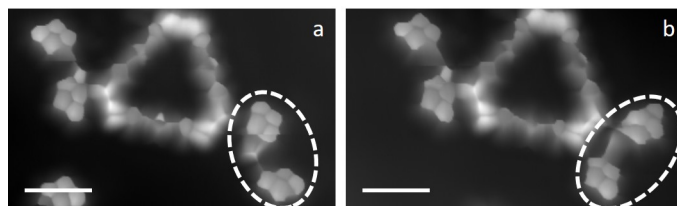


Figure 4.1.6: High-resolution imaging of **d2** dimer after manipulation (a) helps for better seeing the chemical structure which cannot be nicely resolved at the vertex due to the nonplanarity of the BMB triangles. By normal constant height as well as constant current scanning at low bias voltages we notice the tendency of the manipulated dimers to jump back to their initial position at the vertex (b) although STS data with the associated dI/dV maps show no strong bonding of the dimers at the vertices. Scale bar: 1 nm for a and b. $U = 2$ mV.

It remains unclear, however, whether the **d1** dimers also form next to the metal-organic vertices. Although only in low numbers, some covalently coupled dimers (**d1**) and trimers are also found on the Au(111) surface farther from the Au_3BMB_3 complexes upon 360 K annealing. Thus, we cannot discard that **d1** is formed on the bare Au(111) surface and only later diffuses to the metal-organic vertices, which could in turn imply that the selectivity for **d2** at the Au_3BMB_3 vertices is close to 100%. Not being able to discern the two scenarios from our experiments, we can only claim that the 76% yield for **d2** at the metal-organic vertices is a lower limit value. The mechanism whereby the Au_3BMB_3 complexes modify the alkyne-coupling reaction outcome remains an open question and is beyond the scope of this work. We hypothesize, however, that it relates to charge transfer between the organometallic complex and the reactant **m1**. On the alkyne, the HOMO has a bonding and the LUMO an antibonding character (Fig. 4.1.7). Thus, any type of charge transfer will weaken that bond and increase its reactivity, explaining the lower activation temperature for the coupling reactions. The charge transfer will generate local partial charges that also justify the electrostatic attraction of a second **m1** unit (as well as the vertex-dimer attraction).

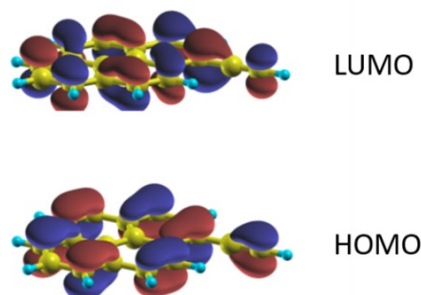


Figure 4.1.7: Calculated wavefunctions for the HOMO and LUMO orbitals of the reactant, revealing the HOMO's bonding character and the LUMO's antibonding character on the alkyne.

Apart from other chemical considerations like modified alkyne acidities,^{148–150} the coupling of the second **m1** dimer to the inner alkyne carbon atom may already be favored sterically if, as expected, the terminal alkyne of the first monomer points towards the Au_3BMB_3 vertex. This would leave the inner alkyne C atom more exposed and promote the observed head-to-tail bonding over the head-to-head coupling that dominates on the bare Au(111).

The two types of dimers observed are not only different in the imaging, but also in the electronic properties. This is an important point, since, apart from Glaser-type coupling,^{141,146} these are the other two possible linkage schemes that may result from linear alkyne coupling reactions (besides the branched 2D structures that are obtained if a third ethynyl group is involved).^{141,146} The electronic properties of organic materials greatly depend on their connectivity.¹⁵² Relevant examples thereof are linear on-surface synthesized polymers whose bandgap can be tuned as a function of the linking bridges between periodic polyaromatic hydrocarbon units.^{153,154} Indeed, an appropriate linkage between periodic pyrene units (as used in this work) has been shown to allow for the creation of remarkably low bandgap polymers.¹⁵³

In general, the bandgap of a material decreases as the electron delocalization increases.^{152,155} Applied to our dimers, the better the electronic coupling between the two pyrene units, the more delocalized will

be the electrons over the whole dimer structure, which will consequently be mirrored in a lower bandgap. Representative spectra for **m1**, **d1** and **d2** are shown in Fig. 4.1.8a. As expected, the monomer displays the largest bandgap. The second largest bandgap value is found for **d2**, with only a minor decrease from 3.8 eV to 3.4 eV (“peak to peak” values of the frontier states marked with shadows). A larger decrease down to 2.8 eV is found for **d1**.

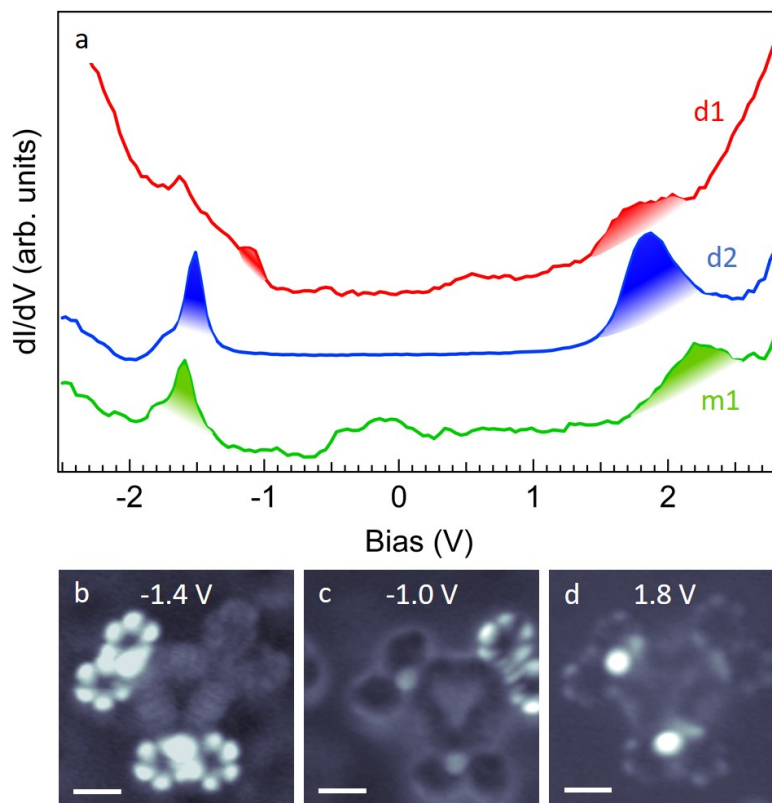


Figure 4.1.8: (a) Comparative dI/dV spectra taken on a monomer (green line), a **d1** dimer (red line) and a **d2** dimer (blue line). The energies of the HOMO and LUMO are shown by shadow colors in corresponding spectra. (b–d) Constant current dI/dV maps of a Au_3BMB_3 complex decorated with **d1** on the upper-right vertex and **d2** on the other two vertices at the HOMO energy of **d2** (b), at the HOMO energy of **d1** (c) and at the LUMO energy of both (d). Scale bars: 1 nm.

The difference between **d1** and **d2** can be rationalized as follows. Whereas **d1** is conjugated across the whole dimer structure, in **d2** one of the double-bonds in the inter-pyrene linkage branches off rather than continuing along the linear coupling motif and causes its cross-conjugation.^{127,155,156} That is, each of the pyrene units extends its conjugation up the branching point, but not with one another. This effect reduces the electron delocalization and causes a larger bandgap closer to that of the monomer.^{127,155} Evidence for the different bandgaps can also be obtained from dI/dV maps of Au_3BMB_3 complexes decorated with the two types of dimers (Fig. 4.1.8b–d, with **d1** on the upper-right vertex and **d2** on the other two vertices). The lowest unoccupied molecular orbitals (LUMO) of **d1** and **d2** only show a minor energy shift, much smaller than their considerable width. That is, the LUMO levels largely overlap and conductance maps around the LUMO energy thus show intensity on both kinds of dimers, as shown in Fig. 4.1.8d at 1.8 eV. The highest occupied molecular orbitals (HOMO), however, are not only sharper but also show a larger energy shift, making it clearly recognizable also in conductance maps. As such, a conductance map at -1.0 eV clearly shows stronger intensity on the lower bandgap structure **d1** (Fig. 4.1.8c), whereas at lower energy (e.g. at -1.4 eV in Fig. 4.1.8b) the signal becomes dominant on **d2**.

4.1.3 Conclusion

Altogether, in this work we have taken a step further in the development of on-surface synthesis. First, we proceed with the surface-supported synthesis of metal-organic complexes that are then used to steer on-surface alkyne coupling reactions. In doing that, the threshold temperature for the reaction activation is lowered and the dominant product outcome is modified. Whereas in the absence of the Au_3BMB_3 complexes a conjugated link is formed between the pyrene units that fosters the electron delocalization

and lowers the overall structure's bandgap, the metal-organic complex promotes the formation of a cross-conjugated link with a comparatively lower electron delocalization and thus with a larger bandgap.

4.2 Reassessing alkyne coupling reactions while studying the electronic properties of diverse pyrene linkages at surfaces

For the work included in this section, sample preparation, SPM measurements and data analysis were performed in collaboration with James Lawrence and Alejandro Berdonces-Layunta, and the precursor molecules were provided by Dulce Rey and Diego Peña.

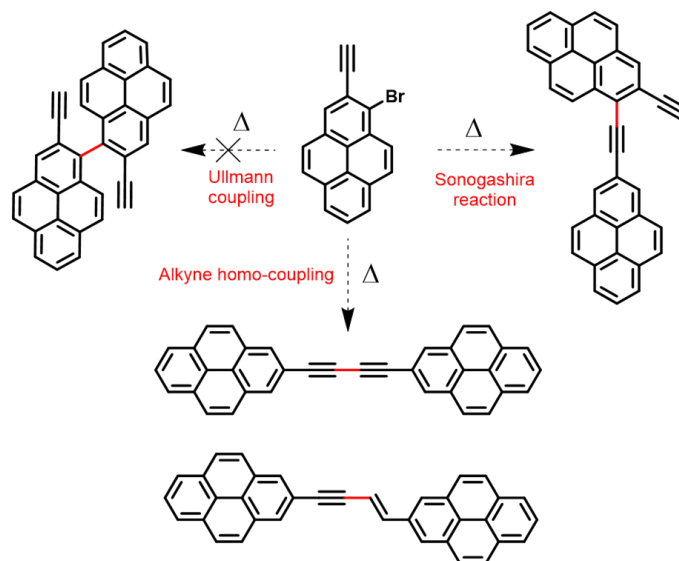
4.2.1 Introduction

Among on-surface reactions, one particular subset of organic reactions that has attracted considerable attention are those involving alkyne functional groups.¹⁴¹ Several reactions exist that involve both homo-coupling to other alkynes and also mechanisms that include hetero-coupling to different functional groups, such as azides,^{157,158} or C-X (where X is a halogen atom),^{159–163} Focusing on alkyne homo-coupling, there is already a wide variety of possible reaction schemes that include dehydrogenative Glaser coupling, as well as non-dehydrogenative head-to-head or head-to-tail alkyne coupling, all of which have been readily reported as occurring on coinage metal surfaces under ultra-high-vacuum as reported in the previous section (section 4.1, ref. [42]) and in other works.^{146,162,164–170} The two former coupling motifs are difficult to discern^{146,164} and although most of these works reported Glaser coupling as dominant, the few studies performed with bond-resolving power by scanning probe measurements with CO-functionalized probes revealed Glaser coupling to be absent and the non-dehydrogenative alkyne coupling to be the most common instead.^{29,42}

Focusing now on cross-coupling reactions, Sonogashira coupling involves the formation of a covalent bond between a terminal alkyne and a carbon atom that is initially bound to a halogen atom. This reaction is less well-studied and more difficult to control,^{160–163} since the starting materials with both alkyne and C-X groups can also undergo alkyne coupling or Ullmann coupling reactions, rendering higher levels of selectivity difficult. However, it has been shown that such systems can be controlled kinetically to lead to the desired Sonogashira product,¹⁶² as well as *via* the use of templating.¹⁶³

Terminal alkyne groups may also undergo cyclization reactions such as the Bergman cyclization.^{168,171,172} Cycloaddition reactions, such as the [2+2+2]^{164,173–175} and [1+1+1+1]¹⁷⁶ types are another possible route towards generating conjugated cyclic linkages. Other varieties such as cascade-type cyclization reactions^{34,177} have also been studied, and allow the formation of polymers after the cyclization step. Altogether, the combination of alkyne and halogen groups provides an extremely wide range of possible reaction schemes.

Here, we have chosen a pyrene-based moiety that possesses both a terminal alkyne and a halogen group, potentially allowing for a multitude of different homocoupling (Ullmann coupling and alkyne coupling) and cross-coupling (Sonogashira coupling) reaction pathways. However, Ullmann coupling is heavily disfavoured by steric clashes while the planar molecular units are adsorbed on the surface, leaving the less studied Sonogashira and alkyne couplings as the clearly favoured options. These basic pathways are summarized in Scheme 4.2.1. Furthermore, the vicinal position of the functional groups facilitates an assortment of cyclization reactions that can follow the initial intermolecular coupling. Whilst we find that there is one favoured reaction pathway that begins with Glaser coupling, a multitude of reaction products are found to coexist. The prevalence for an initial Glaser-coupling is, however, found to be dependent on the presence of the halogen, since in its absence the non-dehydrogenative head-to-head alkyne coupling is favoured instead. The variety of reaction products obtained in these experiments presents an excellent platform for examining the effects of the different coupling motifs on their electronic properties *via* scanning tunnelling spectroscopy measurements.



Scheme 4.2.1: A summary of the basic dimerization reactions that the 2-ethynyl-3-bromopyrene precursor may participate in when adsorbed on the Au(111) surface. Neither the various possible cyclization reactions that may follow nor any trimerization reactions are shown here. The Ullmann coupling pathway is crossed out due to the extreme steric hindrance within its product that would almost certainly prevent it from adsorbing in a planar fashion on the surface.

4.2.2 Results and discussion

As-deposited molecules

At a low coverage of approximately 0.2 monolayer of (M1), Fig. 4.2.1a, most of the molecules self-assemble into dimers, as shown in the STM images in fig. 4.2.1(b) and (c). 17% of the molecules are also found alone on the surface, with an even smaller percentage (<4%) showing signs of having lost one or more of their functional groups. As such, it is clear that the C-Br and alkyne groups generally do not break or react at room temperature on Au(111), fitting well with many other studies.^{32,165,175,177-180}

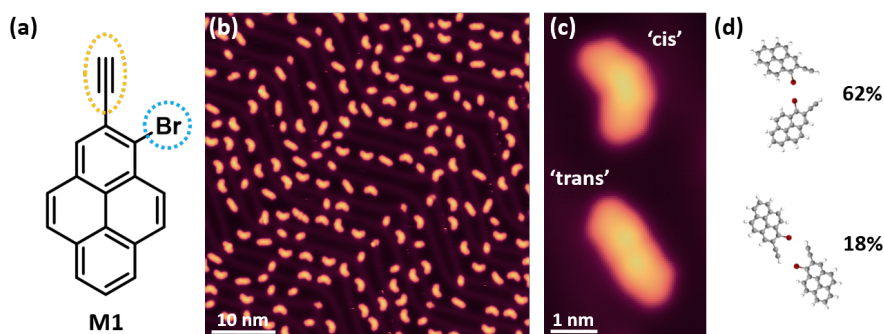


Figure 4.2.1: (a) The chemical structure of 2-ethynyl-3-bromopyrene, with the two reactive functional groups indicated. (b) Overview STM image at 4 K (50×50 nm, 30 pA, -1.5 V) of the as-deposited molecule on Au(111). (c) Zoomed STM image of *cis* and *trans*-type self-assembled dimers. (d) Corresponding models and abundances of the two types of self-assembled dimers. The remaining molecules were either intact monomers that had not self-assembled (17%), or monomers that had lost their bromine atoms/alkyne groups (<4%).

We have designated the two types of self-assembled dimers as '*cis*' and '*trans*' according to their shape. The structural models and abundances for both are shown in Fig. 4.2.1(d). The model for the more common '*cis*' type dimer is also supported by high-resolution BR-STM imaging performed with a CO tip (Fig. 4.2.2(a) and (b)), similar imaging could not be used for the '*trans*' dimers nor the isolated molecules due to their susceptibility to interactions with the STM tip. Both '*cis*' and '*trans*' dimers are held together by intermolecular interactions that are related to halogen bonding, or the equivalent alkyne-alkyne bonding that has been seen in other works.^{181,182}

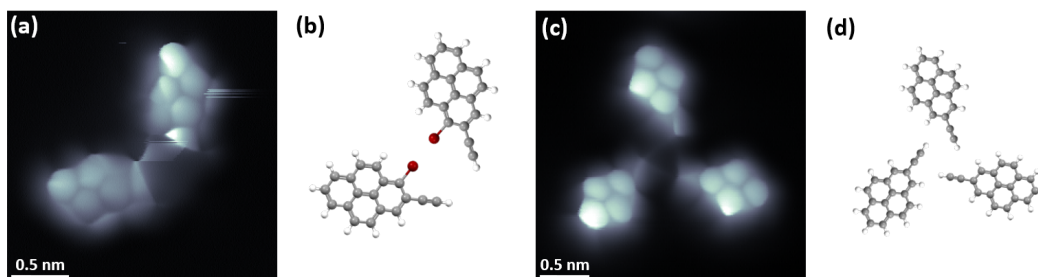


Figure 4.2.2: (a) and (b) BR-STM (CO tip, constant height, 5 mV) and molecular model of the *cis*-type self-assembled dimers of the intact precursor molecule **M1**. (c) and (d) BR-STM (CO tip, constant height, 5 mV) and molecular model of the self-assembled trimers of the molecule after the loss of bromine from its structure (**M2**) at 100 °C. It is assumed that the resulting radical has been passivated, as non-passivated radicals can form metal-organic structures, as seen in Fig. 4.2.8.

Both halogen and alkyne functional groups have been previously shown to possess a so-called "sigma hole" in their electrostatic potential, allowing electrostatic interactions that can govern molecular self-assembly.^{183,184} The more common '*cis*' dimer involves a type I halogen bond between C-Br groups as well as an alkyne-alkyne interaction. The '*trans*' dimer, on the other hand, has two mixed halogen-alkyne interactions. We speculate that the two mixed interactions that hold the '*trans*' dimers together could be overall less energetically favourable than the like-for-like bonds observed in the '*cis*' dimers, accounting for their relative abundances at this coverage.

The molecules are also found to be particularly susceptible to damage *via* bias voltage pulses. Fig. 4.2.3 shows STM images before and after a series of small (+2 V) voltage pulses were applied with the tip in close proximity to the molecules. We expect that the molecules most probably undergo tip-induced debromination,^{58,185} leaving behind radicals bound to the Au(111) surface. The debrominated molecule takes on a distinctive asymmetric shape when scanned at negative bias voltages, with a corresponding peak in the dI/dV spectra (Fig. 4.2.3(c)). The spatial distribution of this state as imaged by constant height dI/dV imaging bears a resemblance to the highest occupied states of the other pyrene species that are also found in this study. The ease with which the molecules were altered by recording dI/dV spectra and bias voltage pulses prevented any measurements of the energetic position of the unoccupied electronic states of the intact molecule.

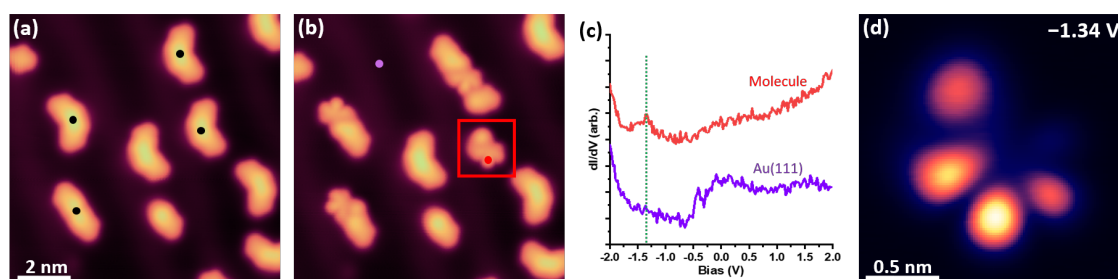


Figure 4.2.3: (a) and (b) STM images (-1.5 V, 200 pA) of intact precursor molecules (**M1**) before and after +2 V pulses and dI/dV spectra at the positions indicated with black spots. (c) dI/dV spectra recorded at the positions indicated with coloured dots in (b). A peak at approximately -1.34 V is marked with a dashed green line. (d) Constant height dI/dV image at -1.34 V of the molecule indicated with the red box in (b). This is most probably the highest occupied state of the debrominated molecule.

Recording another spectrum did not change the molecule any further.

The effects of annealing to 200 °C and 300 °C

Annealing the same low coverage sample to 100 °C, 200 °C, and 300 °C yields a variety of molecular structures on the surface. A comparison of the overview STM images obtained after these three annealing temperatures is shown in Fig. 4.2.4.

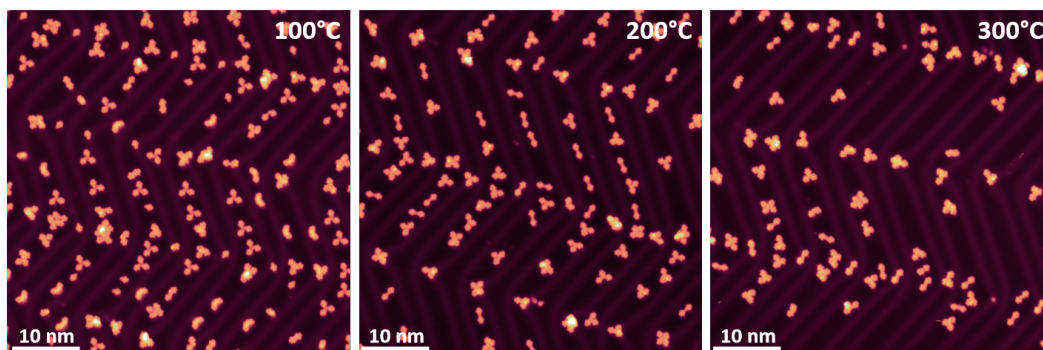


Figure 4.2.4: Large-scale STM images after annealing 2-ethynyl-3-bromopyrene to 100 °C, 200 °C and 300 °C.

At 100 °C, many of the molecules are simply debrominated, and often self-assemble with one another in a variety of clusters. An example of a BR-STM image of a self-assembled trimer of debrominated precursors (held together by alkyne-alkyne interactions) is shown in Fig. 4.2.2c and d. A comparison between the imaging of a pyrene with and without the alkyne group is also shown in Fig. 4.2.5.

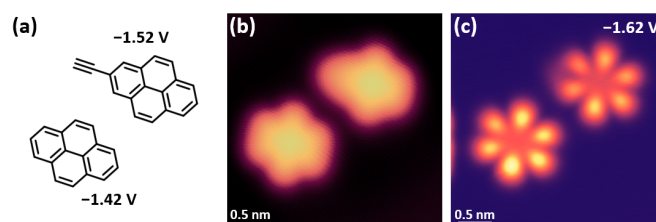


Figure 4.2.5: (a) Chemical structures of pyrene and 2-ethynyl-pyrene, with the onset of their highest occupied states as measured by STS. (b) STM image (-1.5 V, 50 pA) of the two molecules that were found adjacent to one other. (c) Constant height dI/dV image of the two molecules, recorded at a voltage that is slightly more negative than both of their HOMO resonances so that the spatial distribution of this state could be easily imaged for both molecules. A small amount of extra dI/dV signal (relative to pyrene) can be observed at the position of the alkyne group.

There are some signs of metal-organic structures as well as some covalent bonding occurring at this temperature, but the latter was found to be much more prevalent at higher temperatures. Images and dI/dV spectra of a metal-organic trimer structure are presented in Fig. 4.2.6. In normal constant current STM imaging, bright features are found between the original position of the Br substituent and the end of the alkyne group, implying two metal-carbon bonds: one between the debrominated pyrene sp^2 carbon and the metal, and another between the same metal atom and the dehydrogenated alkyne terminal sp carbon of an adjacent molecule. It is not always clear whether the molecules in other self-assembled clusters still possess the radical generated by their debromination, but no indications were found in the BR-STM images of any tilting of the molecules towards the surface or metal adatoms. It may be the case that an unknown fraction of the radicals are passivated by hydrogen atoms that are released by a small number of dehydrogenative reactions that may occur at this temperature, as well as hydrogen that may originate from elsewhere in the UHV chamber, as has been suggested in other studies.^{186, 187}

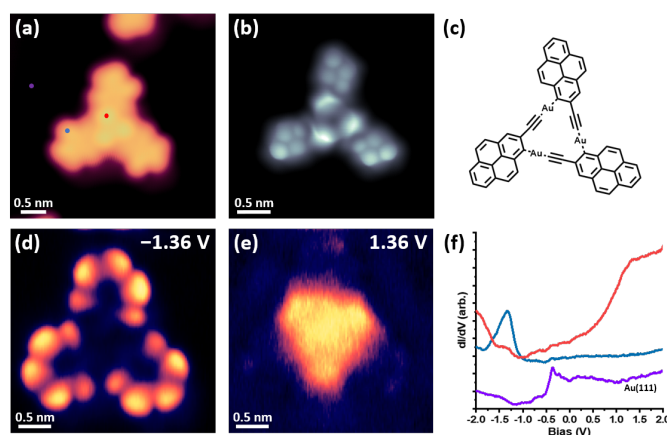
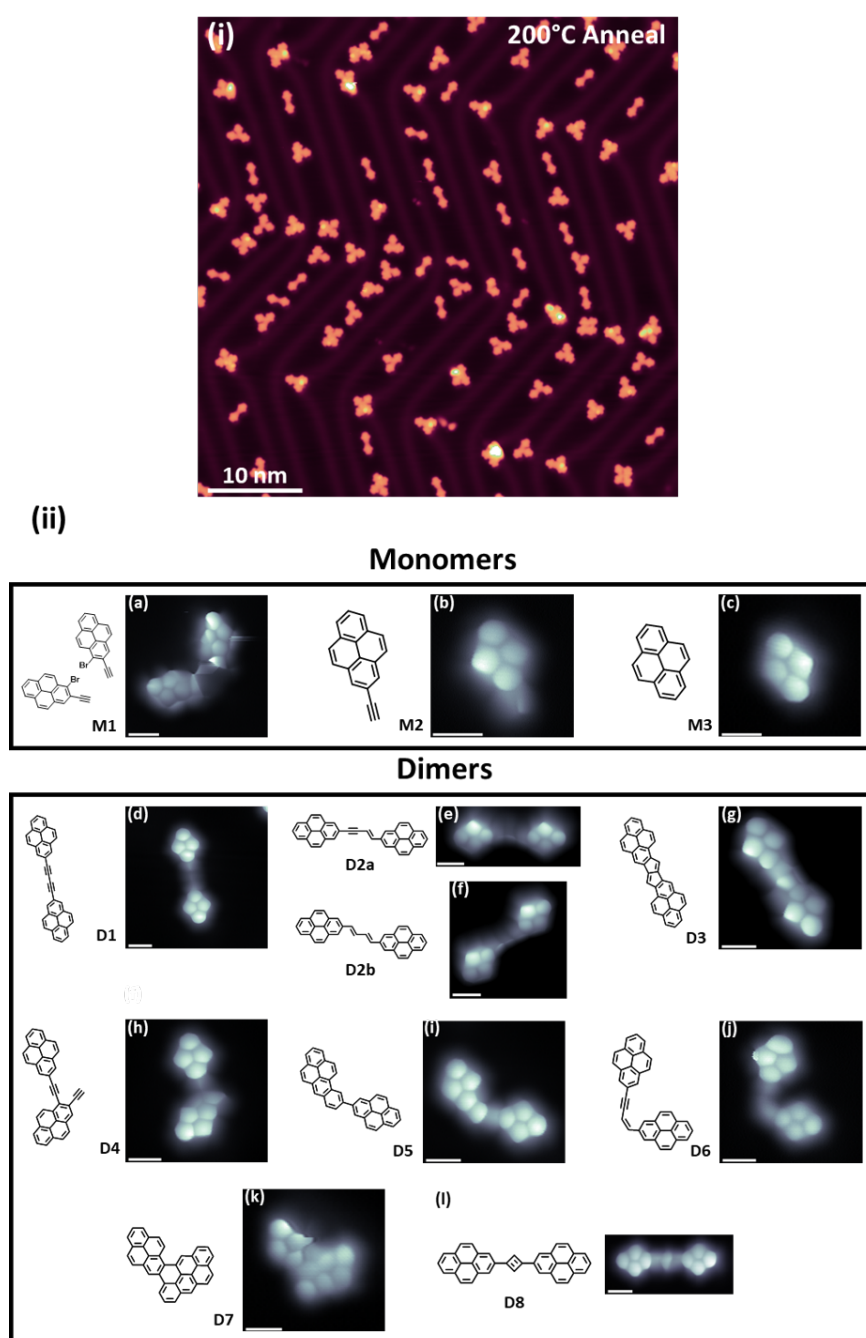


Figure 4.2.6: (a) Typical STM image of a metal-organic trimer (**MO1**) (-1.36 V, 50 pA). (b) BR-STM image of the same trimer (CO tip, constant height, 5 mV). The bright features correspond well to the position of the metal-organic coordinative bonds. The part of the molecule bound to the metal is noticeably darker with less distortion, perhaps indicating that the molecules are tilted towards the surface. (c) Chemical structure of the metal-organic trimer. (d) and (e) Constant current dI/dV images of the same trimer at the highest occupied and lowest unoccupied states taken from the dI/dV point spectra that are shown in (f) and recorded at the positions indicated in (a).

Large-scale STM image of the objects observed after a 200 °C anneal is shown in Fig. 4.2.7i. While in Fig. 4.2.7ii BR-STM image and the corresponding chemical structure of the species observed at this temperature, the Glaser-coupled dimer **D1** is shown in Fig. 4.2.7ii-d.



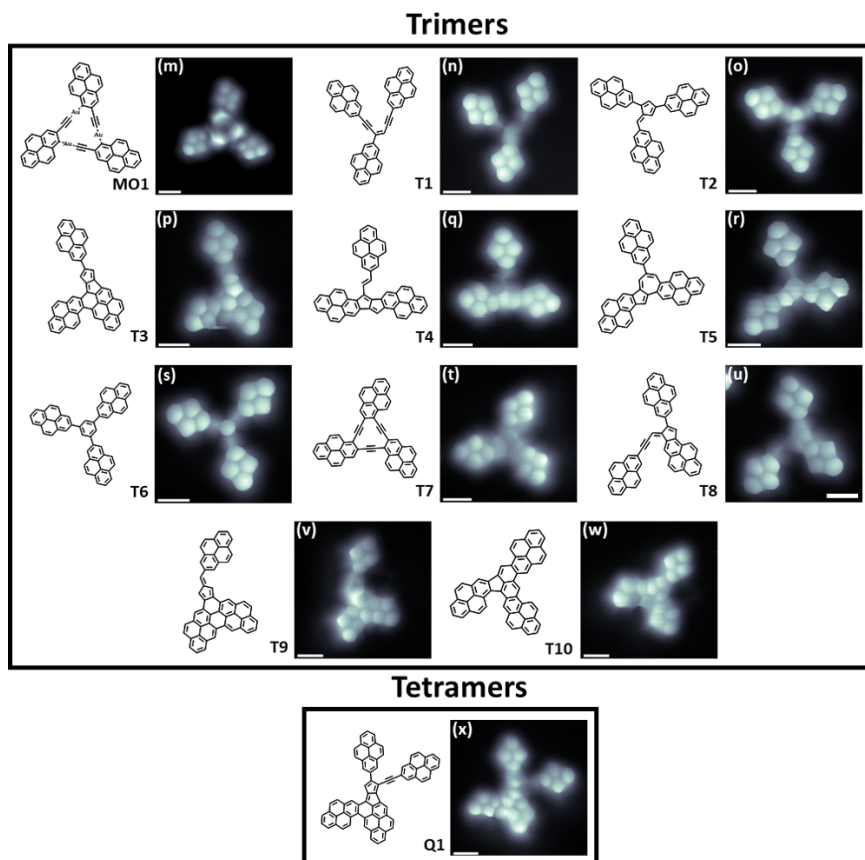
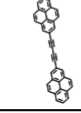
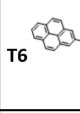
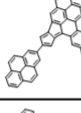

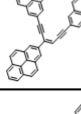
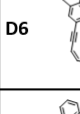
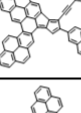
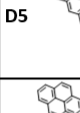
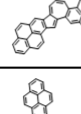
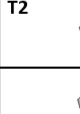
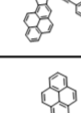
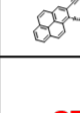
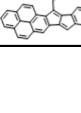


Figure 4.2.7: (i) Overview STM image at 4 K (50×50 nm, 55 pA, -1.5 V) of the sample that had been post-deposition annealed to 200 °C on Au(111). (ii) a-l) Chemical structures and BR-STM images (constant height, CO tip, 2-5 mV) of all of the identified molecules seen throughout this study. All scale bars are 500 pm.

BR-STM imaging proved itself to be vital in identifying many of these molecules, as their internal structures (especially when fused to a significant extent) were not always apparent from standard STM imaging. These molecules are observed after annealing to both 200 °C and 300 °C, in different proportions.

Product statistics

When examining the reaction products at both 200 °C and 300 °C, it becomes immediately apparent that several of them are related, a complete list of the regularly observed molecules and their abundances is provided in Table 4.2.1 and Table 4.2.2.

200°C Anneal					
Structure	% Molecules	% Pyrenes	Structure	% Molecules	% Pyrenes
D1 	36.3	26.5	T6 	1.8	2.0
T3 	11.7	12.9	D3 	2.1	1.6
T1 	11.4	12.5	D6 	1.8	1.3
Q1 	7.1	10.4	D5 	1.8	1.3
T5 	3.6	3.9	T2 	1.1	1.2
T8 	2.8	3.1	MO1 	0.4	0.4
T4 	2.8	3.1	OTHER	15.3	19.9

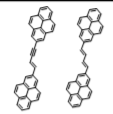
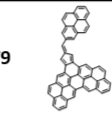
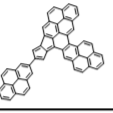
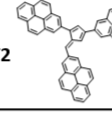
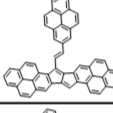
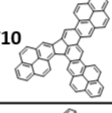
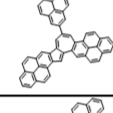
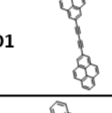
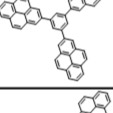
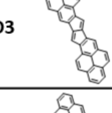
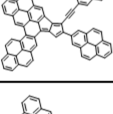
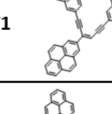
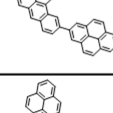
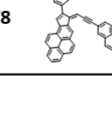
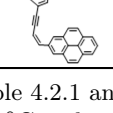
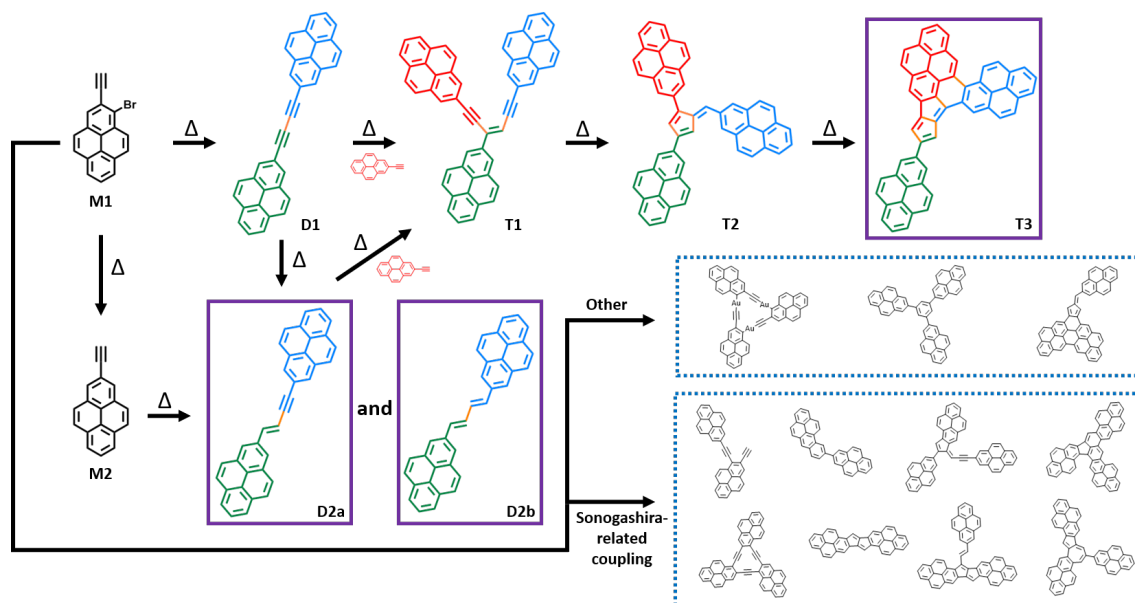
300°C Anneal					
Structure	% Molecules	% Pyrenes	Structure	% Molecules	% Pyrenes
D2 	23.7	16.5	T9 	2.1	2.2
T3 	15.5	16.2	T2 	1.5	1.6
T4 	7.3	7.6	T10 	1.5	1.6
T5 	6.1	6.3	D1 	2.1	1.5
T6 	4.0	4.1	D3 	0.9	0.6
Q1 	2.7	3.8	T1 	0.3	0.3
D5 	4.3	3.0	T8 	0.3	0.3
D6 	3.3	2.3	OTHER	24.3	32.1

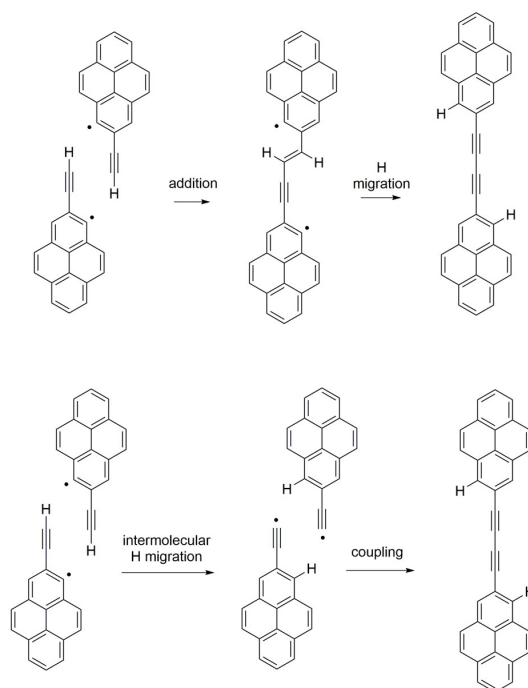
Table 4.2.1 and Table 4.2.2: The statistics for the abundance of the various observed products at both 200 °C and 300 °C annealing temperatures, each is presented with the percentage in terms of the total number of objects, as well as the total number of pyrene components. The two dimers observed at 300 °C have been grouped together due to the difficulty found in differentiating them *via* STM imaging. The third most common object at 200 °C is essentially no longer found at 300 °C, implying that many of them have fused to form the most common trimer or other objects. Any that only appeared once/were irregular structures (*e.g.* nanographenes from more extensive dehydrogenation reactions) are included in "OTHER".

The most common products observed at 200 °C are all part of the reaction path illustrated in Scheme 4.2.2: the Glaser-coupled dimer **D1** that is most commonly observed can be transformed to trimer **T1** upon the addition of a debrominated monomer, forming a *cis*-enediynes in a similar fashion to other works.^{146,182} The enediyne fragment of this trimer then cyclizes to form a 5-membered ring fulvene moiety (trimer **T2**, observed less commonly but shown in Fig. 4.2.7ii-o. This is remarkable, since in solution chemistry the most common cyclization of enediyne is through the Bergman cyclization to obtain a 6-membered ring.^{172,188} Thereafter, **T2** can cyclize further to form another 5- and 6-membered ring, rendering the fused trimer **T3** shown in Fig. 4.2.7ii-p with an integrated pentalene unit that, as will be seen below, has an important influence on the product's electronic properties.

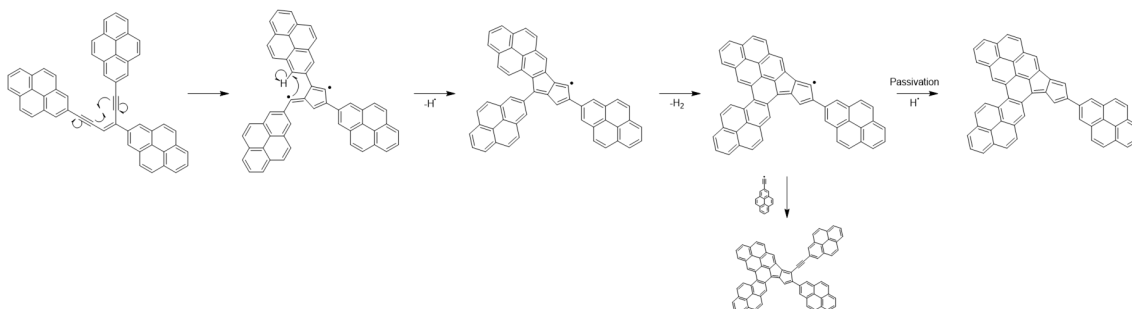


Scheme 4.2.2: The most common reaction pathways found when annealing 2-ethynyl-3-bromopyrene on Au(111) to 200 °C and 300 °C, along with a variety of other products that are also found. While the most abundant products involve an initial Glaser coupling, the formation of several minor products are associated to an initial Sonogashira coupling (shown here grouped together) and other reaction schemes such as cycloaddition. It is important to note that some of these products are derived from one another.

The addition of another monomer to **T3** leads to the tetramer **Q1** in Fig. 4.2.7ii-x. As expected, a subsequent annealing to higher temperature (300 °C) shifts the observed abundance distribution along the reaction path, decreasing that of the initial intermediates and increasing that of the more advanced product structures such as **T3**. Various possibilities for the reaction mechanisms along this general path are discussed in more detail Scheme 4.2.3 and Scheme 4.2.4.



Scheme 4.2.3: Possible routes to the formation of the Glaser coupled dimer, beginning with the brominated precursor. Hydrogen migration may take place before or after the initial formation of the dimer.



Scheme 4.2.4: A possible reaction mechanism to form the fused trimer **T3** from the *cis*-enediynes trimer **T1**. Also included is a suggestion for the origin of the tetramer **Q1**.

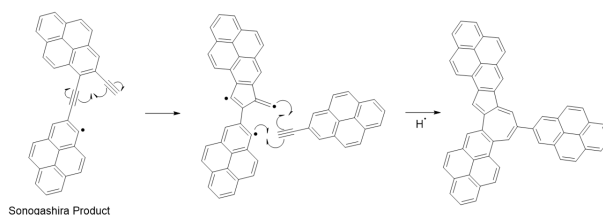
Remarkably, the two most common structures observed at 200 °C (**D1**) and 300 °C (**D2**) merely differ in their level of hydrogenation. Whereas **D1** is unambiguously the product of an initial Glaser coupling of **M1**, **D2** could be the result from a non-dehydrogenative head-to-head alkyne coupling of **M1** or from the hydrogenation of **D1**. However, the total absence of **D2** at lower temperatures and its evolution into the most common product at 300 °C, concomitant with an almost complete disappearance of **D1**, make the latter the only plausible scenario. The source of the hydrogen atoms required for this process may be the various other types of dehydrogenative reactions that are occurring elsewhere on the surface at that temperature.

Although the main products of the reactions of **M1** are all related to the initial Glaser-type coupling, many of the other products are in fact related to Sonogashira cross-coupling, as is indicated in the lower part of Scheme 4.2.2. Few examples of a simple single Sonogashira reaction to form a dimer (for example, molecule **D4** in Fig. 4.2.7ii-h) are observed, with the case of three molecules forming a cycle (**T7**, Fig. 4.2.7ii-t) being even more rare. A metal-organic trimer structure that may be a precursor to this was observed after annealing to 100 °C (Fig. 4.2.6), but the higher quantity of these structures, along with the reversibility of the C-Au bond, may indicate that many of them go on to form other structures at higher annealing temperatures.

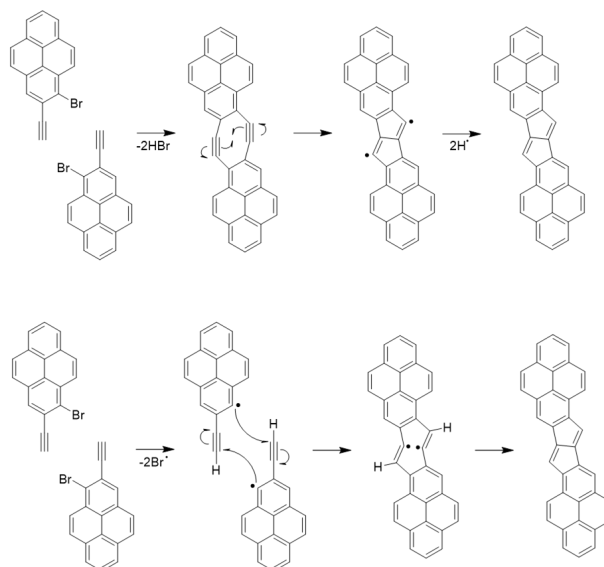
Nonetheless, other dimer and trimer structures that are the result of Sonogashira reactions are often observed. Trimer **T5** (Fig. 4.2.7ii-r), containing a 7-membered ring, is a relatively common product after annealing to both 200 °C and 300 °C. Similarly, a fused dimer linked by a pentalene unit (**D3**, Fig. 4.2.7ii-g) is the direct result of two Sonogashira-type reactions that may occur simultaneously and this dimer evolves into the trimer **T4** (Fig. 4.2.7ii-q) upon addition of another monomer. Possible reaction mechanisms for both of these are presented in Scheme 4.2.5 and Scheme 4.2.6.

Possible reaction mechanisms

It is important to note that there may be multiple pathways that yield the same product. For example, intermediates that possess radicals may be passivated before undergoing further radical mechanisms, but still eventually react to form the same or similar products *e.g.* through dehydrogenation reactions. In our case, as the various reaction intermediates are often observed in STM without any noticeable features that would correspond to surface-stabilized radicals (*e.g.* pointing down into the Au(111) surface with a darker appearance in BR-STM or the obvious presence of stabilizing metal adatoms), neither of the two routes can be ruled out. The almost complete disappearance of the *cis*-enediynes trimer **T1** after the 300 °C annealing fits well with this interpretation, as there was no indication of it possessing a radical when studied *via* BR-STM. Regardless of which may be the dominant pathway, it is worth remarking the unusually favoured fulvene formation (**T2**) in the enediynes cyclization, which subsequently evolves to form a pentalene unit.



Scheme 4.2.5: A possible mechanism for the formation of the trimer **T5** containing the 7-membered ring, starting from a simple Sonogashira product.

Scheme 4.2.6: Two possible mechanisms for the formation of the fused dimer **D3**.

It is important to note that there is a significant increase in the number of irregular structures (i.e. structures that were unique or not found regularly) that are observed upon increasing the annealing temperature from 200 °C to 300 °C. These are counted as "OTHER" in Tables 4.2.1 and 4.2.2, taking up 19.9% and 32.1% of the pyrenes respectively. An increase in this number at the higher temperature is not surprising, as an increased number of dehydrogenative couplings and cyclizations are expected, and there are many possible routes that such reactions may take to form a multitude of structures.

When analysing the initial reaction, the pronounced favouritism for the Glaser coupling is found to be in striking contrast to the observations with a closely related alkyne-functionalized pyrene (1-ethynylpyrene) on the same substrate, for which a non-dehydrogenative head-to-head alkyne coupling showed a remarkable prevalence, as proven by BR-STM (as seen in the previous section, ref. [42]).

Indeed, although there are several articles in which it is claimed that Glaser coupling has occurred, there are no examples in which high resolution BR-SPM has been used to clearly prove the existence of Glaser-coupled products after annealing molecules that only possess terminal alkynes on coinage metal surfaces. It may in fact be difficult for typical STM imaging modes to differentiate between the Glaser-coupled product (e.g. **D1** in this study) and the non-dehydrogenative coupling product (e.g. **D2a**) as the structural offset created by its double bond is relatively small when compared to the straight Glaser-coupled dimer. Theoretical calculations modelling the Glaser coupling on silver surfaces indeed show the reaction mechanism to start with an exothermic non-dehydrogenative head-to-head alkyne coupling, followed by an endothermic hydrogen abstraction.¹⁶⁹ It thus seems natural to expect the non-dehydrogenative alkyne coupling product to be dominant unless the Glaser coupling product can be obtained without hydrogen abstraction (e.g. with alkynyl bromides^{167,189}) or the hydrogen abstraction is facilitated (e.g. by nearby halogen atoms).¹⁹⁰

To further investigate this, we have synthesized the 2-ethynyl-pyrene precursor molecule without the attached bromine (monomer **M2**) and deposited it on an Au(111) surface. As shown in Fig. 4.2.8, the as-deposited molecules are clearly identified *via* BR-STM imaging as only possessing their terminal alkyne functional groups, which also direct their self-assembly into trimers at low coverages. Annealing this sample to 100 °C, 200 °C and 300 °C does not yield the Glaser-coupled dimer **D1** at any stage, instead only yielding dimers **D2a** and **D2b** and an assortment of other products (Fig. 4.2.8c and d).

It is worth mentioning here that all of the trimer products along the main reaction pathway in Scheme 4.2.2 are also found when annealing **M2**. Starting from **M2**, however, only dimers **D2a** and **D2b** form, with no examples of dimer **D1** observed. This implies that trimer **T1** and all of the following products can also be formed by the dimer **D2a**, further demonstrating that multiple reaction mechanisms may yield these main products. As expected, no Sonogashira-related products were observed when annealing monomer **M2**.

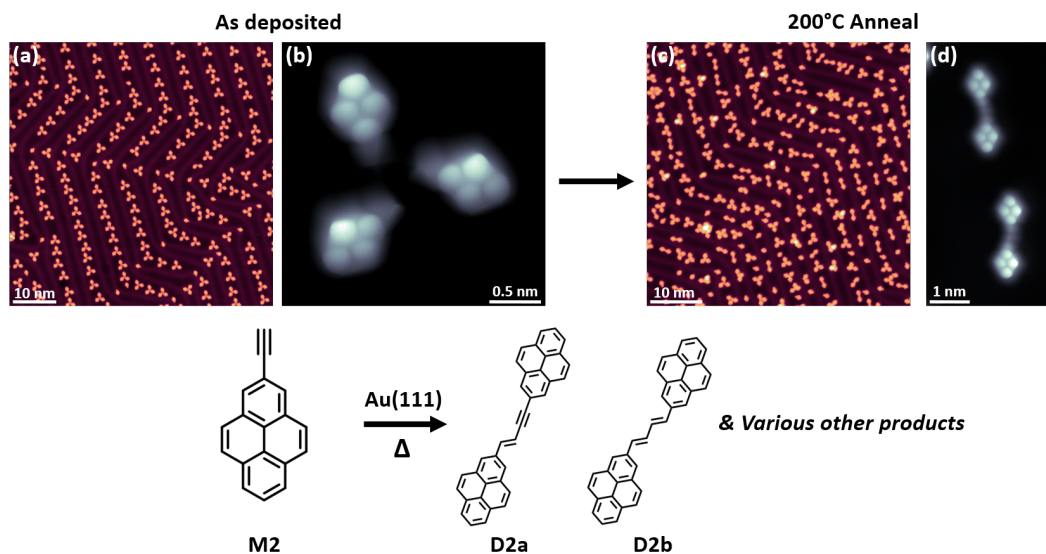


Figure 4.2.8: (a) and (b) Self-assembled trimers of 2-ethynyl-pyrene **M2** on Au(111) after deposition at room temperature. (c) and (d) The same sample after annealing to 200 °C. The only dimers observed have a clear offset in BR-STM imaging, indicating the formation of double bonds (**D2a** and **D2b**). No straight Glaser-coupled dimers were observed. The other main pathway products formed by the brominated precursor **M1** (**T1**, **T2** and **T3**) were also formed by **M2** upon annealing, indicating that **D2a** can also react further to form these molecules.

It must be noted that, besides the assignment by BR-STM, the various spectroscopic fingerprints discussed below also confirm this conclusion. It follows that the bromine must play a key role in the formation of **D1**, at least on the Au(111) substrate. We presume that the preference for Glaser-coupling observed in this work may be promoted by the presence of the neighbouring radical that is generated upon dehalogenation. Hydrogen migrations to the radical position (Scheme 4.2.3) allows the Glaser-coupling to occur without a formal loss of hydrogen and the aforementioned associated endothermic effect,¹⁶⁹ rendering it thermodynamically more favorable. It may also be the case that any locally co-adsorbed atomic bromine favours the Glaser coupling of terminal alkynes, reducing the activation energy by weakening the C-Br bond.¹⁹⁰ Neither of these explanations may be completely discounted without further studies.

The relationship between the chemical structure and the electronic structure of the products

The wide range of products obtained enables a systematic study of the relationship between chemical and electronic structure when considering the different linkages between pyrene moieties. We have thus performed scanning tunnelling spectroscopy measurements on several of the molecular species. Differential conductance spectra show clear peaks that correspond to the highest occupied and lowest unoccupied states of the molecules (HOMO and LUMO, respectively), from which the HOMO-LUMO gap has been determined. The measurements obtained on the reference monomer **M2**, as well as on a range of dimers and trimers, are presented in Fig. 4.2.9, with each category ordered in terms of the measured HOMO-LUMO gap, going from the largest to the smallest. When comparing the types of pyrene coupling to the observed trends in the energy gap, several conclusions can be drawn.

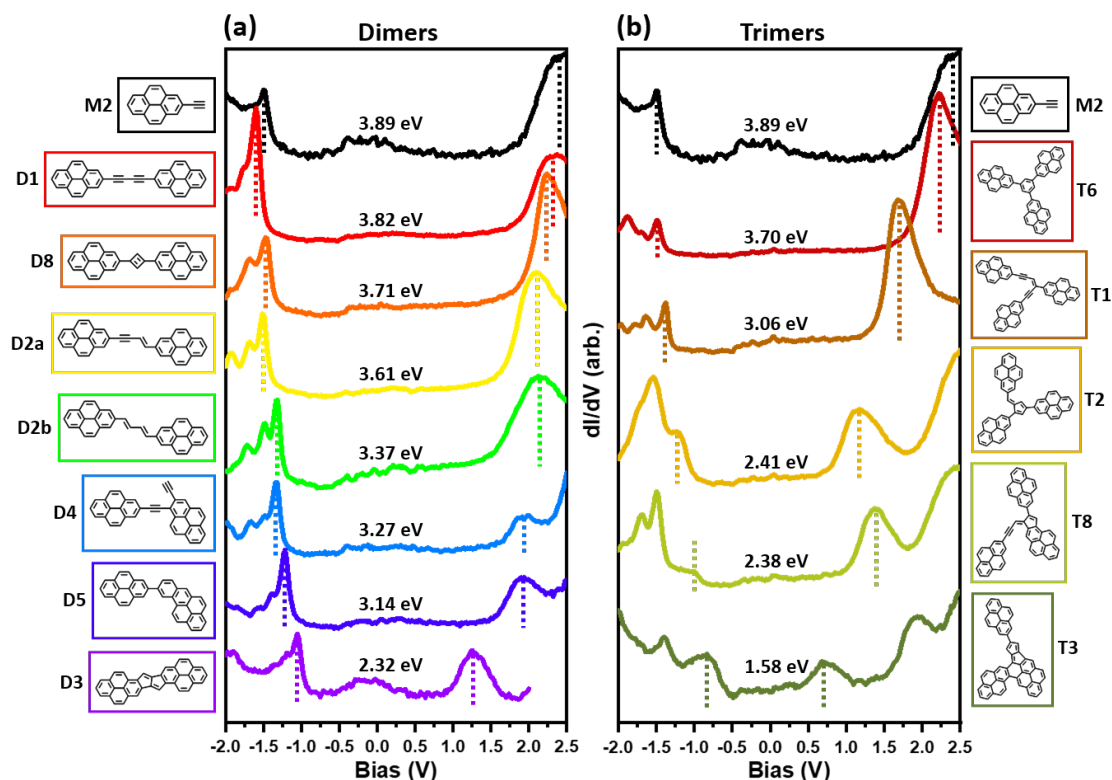


Figure 4.2.9: dI/dV point spectra of several different (a) dimers and (b) trimers that were observed after annealing the sample to 200 °C and 300 °C. For each molecule, the highest occupied and lowest unoccupied resonances are marked, with the corresponding HOMO-LUMO gap indicated. A clear shrinking of the HOMO-LUMO gap can be observed when increasing the level of coupling between the pyrene components.

Firstly, the formation of a Glaser-coupled dimer **D1** (Fig. 4.2.9a, red) does not appear to significantly alter the HOMO-LUMO gap when compared to a 2-ethynyl-pyrene monomer **M2**, despite a small rigid downshift in the electronic states of the molecule. Since the HOMO-LUMO gap of molecular materials is reduced as the conjugation and the associated electron delocalization increases,¹⁵² the formation of a single bond between the alkyne groups does not seem to be a particularly effective channel for conjugation. Changing one of the triple bonds into a double bond (**D2a**, Fig. 4.2.9a, yellow) reduces the energy gap by approximately 0.2 eV. This implies an increased level of conjugation with the double bond in comparison to the triple bond, resulting in a smaller HOMO-LUMO gap. A comparison may be drawn to the difference in energy gap between phenylacetylene and styrene, with a smaller gap predicted for the latter.¹⁹¹ The transformation of the remaining triple bond to a double bond in **D2b** (Fig. 4.2.9a, green) further lowers the energy gap by approximately another 0.2 eV. Imaging the spatial distribution of the frontier electronic states supports the better electronic coupling between the pyrenes in both **D2a** and **D2b**, which both display a notable intensity of the frontier electronic states over the linking conjugated double bond structures (Fig. 4.2.10). In stark contrast, the equivalent map on the Glaser-coupled dimer **D1** reveals a pronounced and wide node along the linking motif (Fig. 4.2.10), which can be rationalized as an anti-bonding scenario of the respective pyrene HOMO orbitals with a consequently weak coupling and very little difference made to the energy gap when compared to the monomer **M2**.

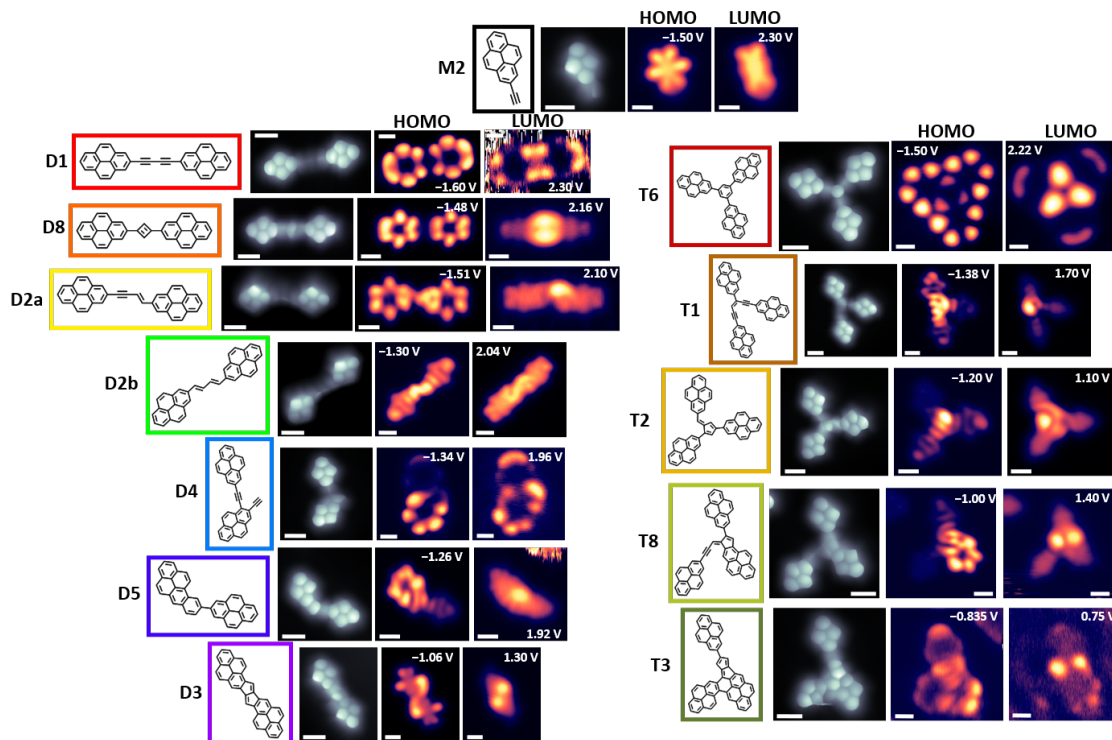


Figure 4.2.10: The chemical structures, BR-STM images, and dI/dV images of all of the species presented in Fig. 4.2.9. The dI/dV images of **D1**, **D4**, **T6** and **T3** were recorded in constant current mode, with the rest in constant height. All dI/dV images were recorded with a CO tip, with the exception of **M2**, **D3** and **T6**.

The dimer obtained *via* a Sonogashira reaction has a larger impact on the gap, with a reduction by approximately 0.6 eV relative to the monomer (**D4**, Fig. 4.2.9a, light blue). This reveals an increased level of conjugation when directly adding an alkyne group to this position on the pyrene ring, adjacent to the original alkyne group. The dI/dV images of this molecule at the HOMO and LUMO energies, presented in Fig. 4.2.10, show a clear difference between the two constituent pyrenes, with the majority of the intensity of both HOMO and LUMO (although more prominently the former) found over the pyrene with two alkyne groups attached to it.

In molecular structures displaying conjugated segments connected by more poorly conjugated linkages (*e.g.* with cross-conjugation), their HOMO-LUMO gap is typically determined by the largest of the conjugated segments.^{192,193} Our results can thus be qualitatively understood as a pyrene unit with two conjugated ethynyl groups (their conjugation is further promoted by their ortho positions) that consequently hosts the HOMO and LUMO, and a weaker conjugation to the second pyrene. If the two ethynyl groups cyclize to form the dimer **D5** (Fig. 4.2.9a, dark blue) the same scenario is further enhanced. The new ring is cata-fused, preventing the formation of an additional Clar sextet that would limit the electron delocalization outside the ring. Instead, the conjugation is increased, which is mirrored in a further reduction of the gap. As expected, the HOMO intensity remains mostly localized on the “extended pyrene” (Fig. 4.2.10).

The largest gap reduction for the dimers, down to 2.32 eV, is obtained in dimer **D3** (Fig. 4.2.9a, purple), in which the two pyrene units are linked by two 5-membered rings that make up a pentalene unit. The presence of non-benzenoid rings in polyaromatic hydrocarbons often leads to low gap values, occasionally even resulting in antiaromaticity or open-shell characters.^{194–196} It is thus not surprising to find **D3** as the lowest HOMO-LUMO gap dimer structure. The efficient electronic coupling between the two pyrenes and the associated electron delocalization is further corroborated by the conductance maps of the HOMO and LUMO, which are both extended over the whole structure and include strong intensity over the pentalene moiety.

Similar conclusions can be drawn from the analysis of trimer structures. Due to the larger molecular size, one would naively expect lower HOMO-LUMO gap values.¹⁸⁹ However, as seen with the dimers, this depends dramatically on the coupling motif. The symmetric [2+2+2] product trimer **T6** in Fig. 4.2.9b (dark red) has the largest energy gap among the trimers, with a value close to the monomer **M2**/Glaser-coupled dimer **D1**, implying a very small electronic coupling among the different pyrene units. The aromatic ring within the linking motif, not directly coupled to any of the pyrene units, limits the

electron delocalization outside the ring.¹⁹⁷ This can be rationalized when considering the Clar formula of the system, which displays a Clar sextet within the central ring. Any resonant structure with a double bond between the pyrene units and the central ring would display fewer Clar sextets, with an associated energetic cost.¹⁹⁸ In addition, the three pyrenes are linked to the central aromatic ring at meta positions, causing a cross-conjugation that further limits the electron delocalization.^{42,127,156} Altogether, the three attached pyrenes can almost be pictured as separate isolated "legs". A similar rationalization can also be used to explain the high energy gap of dimer **D8**.

Focusing on the *cis*-enediynes trimer **T1** (Fig. 4.2.9b, light brown), we find a substantially reduced HOMO-LUMO gap of 3.06 eV. In this case the coupling motif is such that, whilst one of the pyrene units is conjugated to the other two, these two are not conjugated with one another. Of the two linear conjugation paths along the coupling motif, one is longer than those discussed earlier, whereas the other is comparable to that discussed with **D2a**. As expected, the additional conjugated path to a third pyrene thus lowers the gap value below that of **D2a**. dI/dV imaging of the frontier states in Fig. 4.2.10 clearly shows a much higher intensity over this linking structure for both the highest occupied and lowest unoccupied states. Fusing the central *cis*-enediynes linkages into a conjugated fulvene structure significantly lowers the energy gap even further, as shown by **T2** with its much smaller energy gap of 2.41 eV. Again, dI/dV imaging of this molecule (Fig. 4.2.10) clearly demonstrates a strong association of the frontier resonances with the non-benzenoid connecting ring. If the five-membered ring is directly fused to one of the pyrene units (**T8**) the gap is also small, with the conductance maps again revealing a HOMO that is dominantly localized on the "extended pyrene" (Fig. 4.2.10).

The lowest HOMO-LUMO gap of all of the products studied is found for trimer **T3** (Fig. 4.2.9b, dark green), with a value of 1.58 eV. We find the following particularities in this structure: (i) the three pyrenes are conjugated with one another; (ii) two of the pyrenes are in fact fully fused by an aromatic ring generating a large polycyclic unit; (iii) the bonding motif again includes the antiaromatic pentalene moiety that indeed hosts much of the otherwise fully delocalized HOMO and LUMO signal in conductance maps (Fig. 4.2.10). Following a similar reasoning to the above, all of these contribute to a substantial lowering of the HOMO-LUMO gap and explain its particularly low value.

As we have clearly shown the effect of all of these different linkages, we hope that it can provide a reference for future works, in particular those that aim to form conjugated polymers or nanoribbons that are formed from similar components. Indeed, recent works have shown the critical role that the electronic coupling of different linking motifs have on the bandgap of organic polymers, which can be used to design structures with unprecedented low bandgap values.^{153,154} Controlling these linkages thus allows a precise control of the HOMO-LUMO gap of small molecules, as well as the engineering of polymeric conjugated systems with tunable bandgaps.

4.2.3 Conclusion

We have extensively examined the reaction pathways of a pyrene precursor with alkyne and bromine substituents at vicinal positions on the Au(111) surface. The precursor was found to favour Glaser coupling, followed by the formation of increasingly fused trimer structures at higher temperatures due to different cyclization reactions. We have clearly demonstrated, *via* the use of a non-brominated precursor, that the Glaser-coupled product can only be formed when there is also a C-Br group attached to the molecule. This may be due to a hydrogen migration that follows the debromination of the molecule, allowing a more thermodynamically favourable pathway to the Glaser-coupled dimer than to the non-dehydrogenative product. Many other products that resulted from Sonogashira-type coupling were also observed, as well as various intermediates. This wide variety of minor products allowed an extensive study of the electronic properties of different linkages between pyrene moieties, with clear relationships found between the formation of double bonds, new rings and the formation of antiaromatic pentalene motifs and a narrower HOMO-LUMO gap. We hope that this knowledge may help to guide the design of extended conjugated systems in the future, such that their band gaps may be more easily controlled according to our needs.

Chapter 5

Acene-based chemistry

5.1 On-surface synthesis of heptacene on Ag(001) from brominated and non-brominated tetrahydroheptacene precursors

For the work included in this section, sample preparation, SPM measurements and data analysis were performed in collaboration with Luciano Colazzo and Pawel Nita, DFT calculations were provided by Carlos García Fernández, Paula Abufager and Nicolás Lorente, and the precursor molecules were provided by Ruth Dorel and Antonio M. Echavarren.

5.1.1 Introduction

Acenes are a class of polycyclic aromatic hydrocarbons consisting of linearly fused benzene rings. Their interesting electronic properties have made them the subject of a vast number of experimental and theoretical studies.^{199,200} For example, pentacene has been integrated into several types of devices with remarkable success because of its particularly high charge carrier mobility.^{199,200} Acenes longer than pentacene are predicted to have even more promising properties,²⁰¹ but have been studied much less. This is directly related to their lower stability,^{202,203} which makes their synthesis by conventional wet chemistry much more challenging,²⁰⁴ and further limits their potential implementation into device structures. Indeed, the synthesis of non-substituted higher acenes has been until recently restricted to the photodecarbonylation of carbonyl-bridged precursors, and needs to be carried out in stabilizing inert matrices at cryogenic temperatures.^{205–207}

Among the reasons for such reduced stability is the increasing open-shell character predicted for acenes as they grow longer. According to calculations, partial diradical character starts appearing for hexacene, with a notable contribution of polyradical character for longer acenes like undecacene or dodecacene.^{208,209} That is, predictions associate every five to six rings with roughly two unpaired electrons.²¹⁰

On-surface chemistry under ultra-high vacuum (UHV) has appeared as an efficient way to overcome some of these limitations. Under the clean and controlled environment of UHV chambers, higher acenes have not only been successfully synthesized, but are also stable, allowing their subsequent characterization with surface science techniques. Following this approach, tetracene,²¹¹ hexacene,²¹² heptacene,^{213,214} octacene,²¹⁴ nonacene,^{38,214} decacene^{214,215} and undecacene²¹⁴ have been synthesized and characterized on Au(111). Pentacene and heptacene have also been synthesized on Ni(111)²¹⁶ and Ag(111),²¹⁷ respectively.

In this work, starting from two different precursors, we study the synthesis process of heptacene on Ag(001). Single molecule analysis by scanning tunneling microscopy (STM) and scanning tunneling spectroscopy (STS) has been applied to extract information on the structural and electronic properties of reactants, intermediates, and heptacene end-products.

5.1.2 Results and discussion

The precursors correspond to dibromo-tetrahydroheptacene (Br-**1**, Fig. 5.1.1a) and tetrahydroheptacene (**1**, Fig. 5.1.1d),²¹⁸ merely differing in the bromination (or its absence) at the central carbon ring. Deposition of the reactants on a surface held at room temperature (RT) and subsequently cooled to 4.3 K for their characterization results in samples as shown in Fig. 5.1.1.

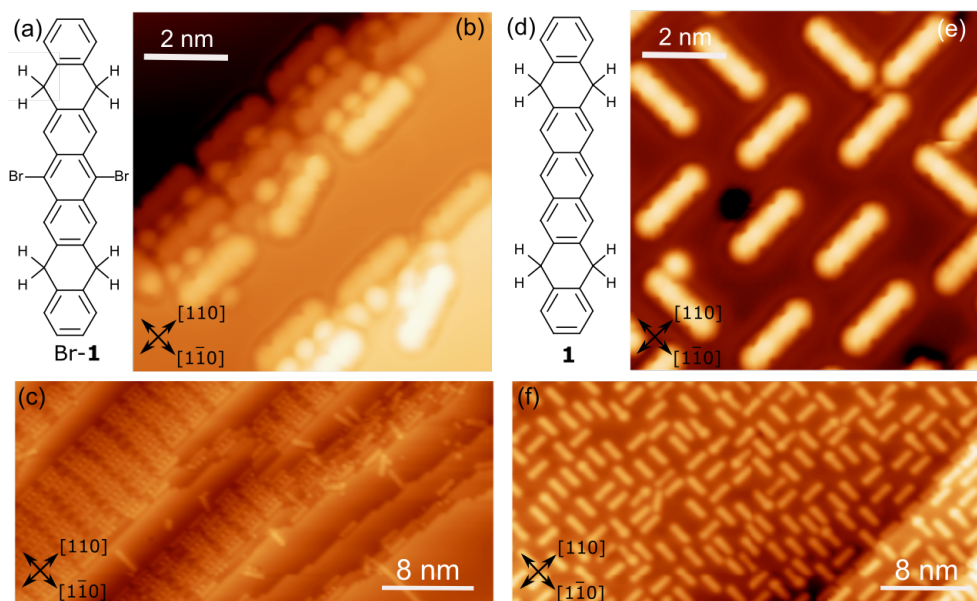


Figure 5.1.1: (a) Chemical structure of precursor Br-1 and representative small (b) and large (c) scale STM images of the surface after its deposition on Ag(001) held at RT [$U = 30$ mV/ $I = 70$ pA (b) and $U = 30$ mV/ $I = 100$ pA (c)]. (d) Chemical structure of reactant 1 and representative small (e) and large (f) scale STM images of the sample after its deposition on Ag(001) [$U = 35$ mV/ $I = 100$ pA (e) and $U = 600$ mV/ $I = 600$ pA (f)]

The samples with Br-1 (Fig. 5.1.1b and c) display two types of well-differentiated surface morphologies: reconstructed substrate regions with highly periodic monatomic steps along the compact [110] or [1-10] directions (Fig. 5.1.2) and flat Ag(001) terraces. Unless high coverages force the formation of close-packed layers all over the substrate, the molecules appear preferentially adsorbed on the reconstructed regions. All the molecules appear readily debrominated at RT.

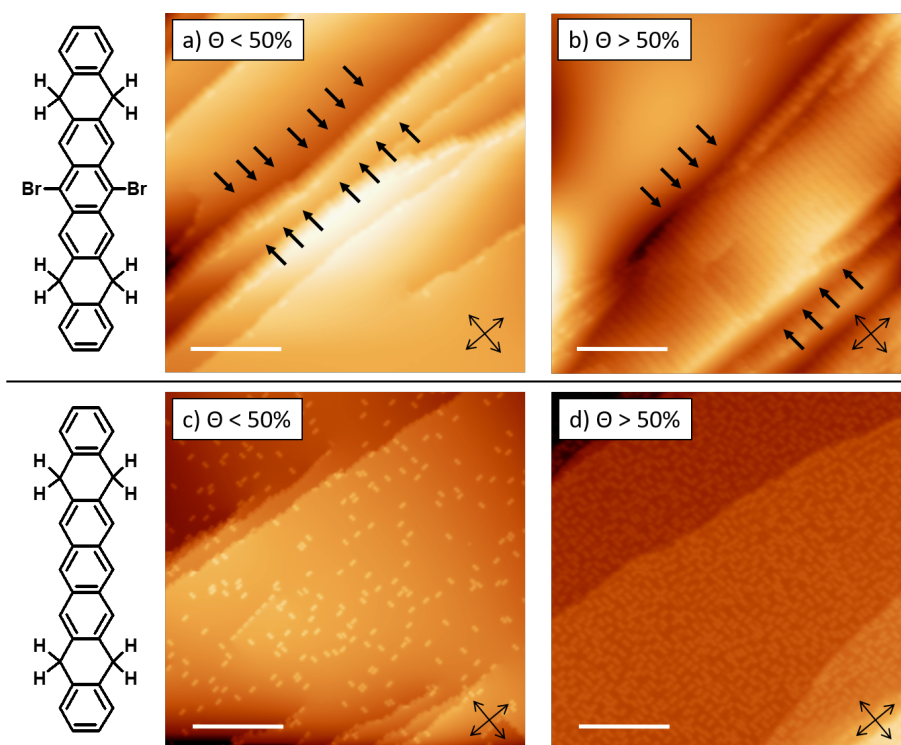


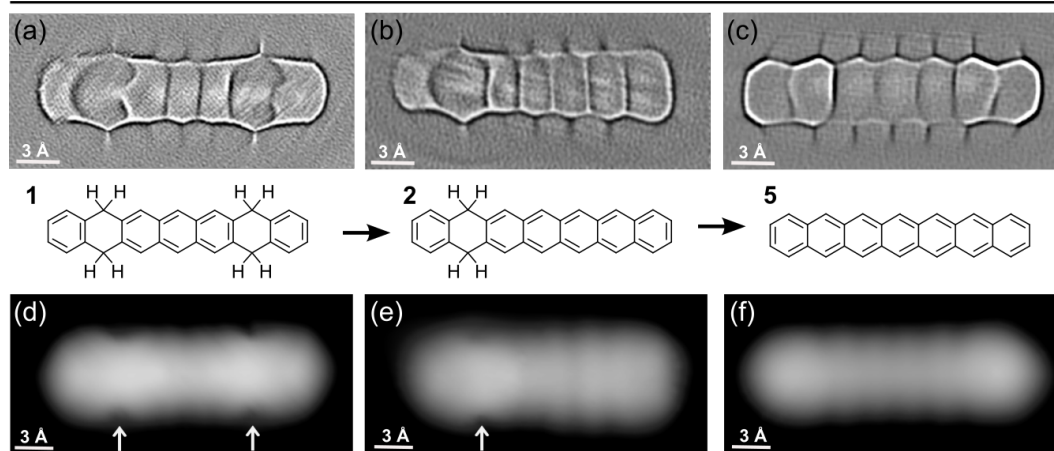
Figure 5.1.2: Comparison of the surface morphology variations resulting from the deposition of precursor Br-1 (top) and precursor 1 (bottom) on Ag(001) held at RT, for two different coverages: low (left) and high (right). (a-d) STM images [Scale bar 20 nm, $U = 1$ V, $I = 100$ pA]. Cross arrows represent the high symmetry [110] and [1-10] directions of the substrate. In (a) and (b) black arrows are a guide for the eye used to highlight the extension of the high density step regions at increasing coverages.

While this is similar to the findings with other brominated reactants on Ag(110),²¹⁹ it differs from the results on Ag(111),^{7,219} suggesting, as generally expected, a higher reactivity of less densely packed surfaces. Each reconstructed terrace fits one molecule and one to three neighbouring Br atoms. The molecules on subsequent terraces appear aligned with respect to one another and display long-range order domains.

Equivalent experiments with the non-halogenated reactant **1** lead to notably different results (Fig. 5.1.1d and f). In the absence of Br substituent, the molecules on the Ag(001) terraces align along the [110] or [1-10] directions, but cause neither a surface reconstruction nor show any kind of long-range order. We thus associate these two effects to Br-driven interactions, in line with previous reports of other brominated precursors on noble metal surfaces.^{33,220}

Upon heating, both kinds of reactants suffer dehydrogenation of the non-aromatic rings. In this process, hydrogens are lost pairwise, while on the organic scaffold the aromatization of the rings occurs as displayed in Fig. 5.1.3.

On-surface synthesis of heptacene



Methylene transposition intermediates



Figure 5.1.3: On-surface synthesis process of heptacene from Br-1, displaying the evolution of the molecule's chemical structure throughout the reaction with two, one, and no hydrogenated non-aromatic rings. The associated high resolution and constant height images revealing the bonding structures ($U = 2$ mV, Laplace filtered) are shown in panels (a), (b) and (c), respectively. Panels (d), (e) and (f) display the corresponding constant current STM images ($U = 30-50$ mV/ $I = 100$ pA), while (g), (h) and (i) display the intermediates involving methylene transposition. All images are recorded with CO-functionalized probes.

Focusing first on Br-1, a stepwise dehydrogenation is observed for the two rings. Although a detailed characterization of threshold temperatures was not performed, annealing of the samples to 180 °C caused the aromatization of one ring in most of the molecules (Fig. 5.1.4a), and a quasi-full transformation into heptacene was observed after annealing to 270 °C. The disparate activation temperatures evidence differences in the mechanisms of the first and second aromatization events, which may be affected e.g. by the potential remaining radicals generated upon dehalogenation. After aromatization of the first ring, the remaining non-aromatic ring easily shifts along the molecule (Fig. 5.1.3h-i). Its position can be distinguished through high-resolution constant height imaging using CO-functionalized tips, which features methylene functionalities on polyacenes as distinctly wider rings (Fig. 5.1.3a and b). Alternatively, an indentation-like contrast at low bias (highlighted with arrows in Fig. 5.1.3d-i), an increased apparent height at positive bias or a node at negative bias (Fig. 5.1.5) is observed at the hydrogenated rings by conventional constant current STM imaging.

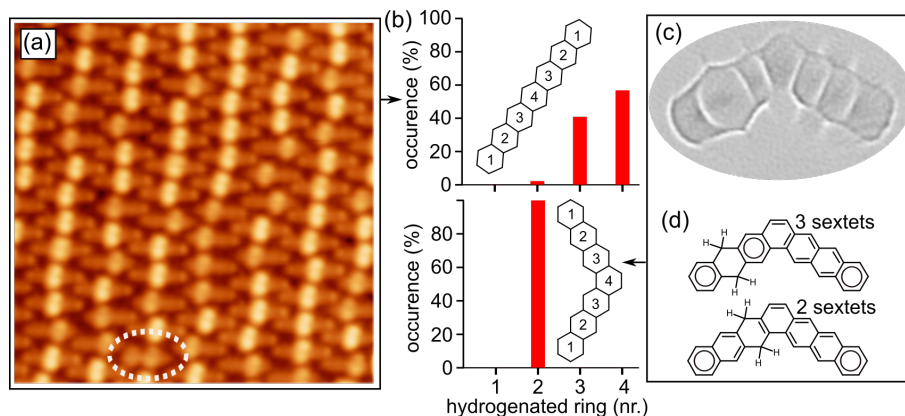


Figure 5.1.4: (a) STM image ($U = 1.7 \text{ V}/I = 186 \text{ pA}$) of a full monolayer sample of Br-1 after annealing to $180 \text{ }^\circ\text{C}$. The oval marks a tetrahydroheptacene molecule after a methylene migration (intermediate 1^*). (b) Histograms displaying the occurrence of differently positioned hydrogenated rings (numbered as in the insets of molecular structures) for dihydro intermediates of heptacene (top) and heptaphene (bottom). (c) Laplace-filtered constant height STM image ($U = 2 \text{ mV}$) of a heptaphene intermediate with a single hydrogenated ring. (d) Schematics revealing the maximized number of Clar sextets for dihydroheptaphene when hydrogenated at the second ring (compared below, e.g., with hydrogenation at the third ring).

A statistical analysis of the position of the hydrogenated ring reveals its tendency to shift toward the central part of the molecule (Fig. 5.1.4a and b). Since the hydrogenation breaks the conjugation along the molecule, intermediates **2-4** (Fig. 5.1.3) can be seen as made up by two coupled but independent acenes. Taking into account that the aromatic stabilization energy per π -electron as calculated from homodesmotic reactions is notably reduced as the number of annulated rings increases,²²¹ the shorter the acene segments to be combined are, the more stable the molecules are. As a result, their occurrence is the highest for **4**, followed by **3** and then by **2**, whose longest acene segments correspond to anthracene, tetracene and pentacene, respectively.

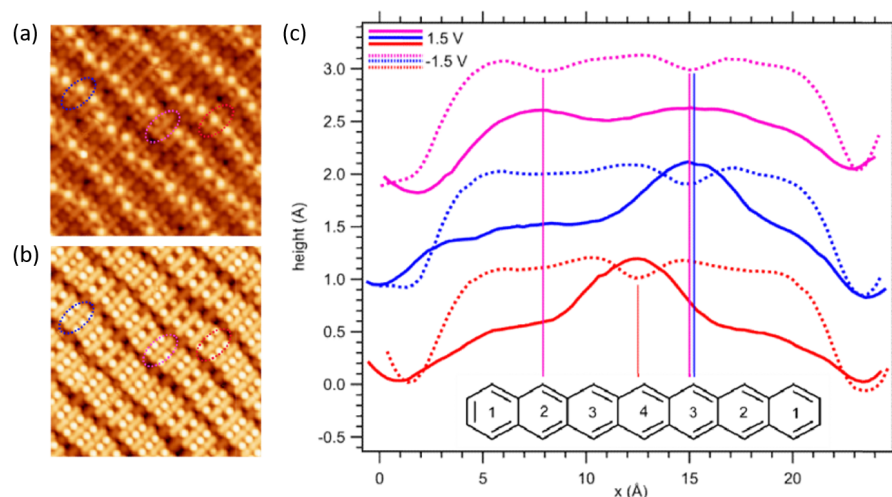


Figure 5.1.5: Conventional constant current STM imaging of heptacene intermediates at (a) 1.5 V (b) -1.5 V sample bias. The former displays protrusions at the hydrogenated ring, while the latter displays a node. Profiles on the surrounded molecules in (a) and (b) are further displayed in (c), put in relation with a molecular structure model. It can be seen how the same profiles on the same molecules display lobes or nodes at positive or negative bias, respectively, and the correspondence with the particular rings.

In fact, even those few molecules that retain tetrahydrogenation after this first annealing step (e.g. oval in Fig. 5.1.4a) display the hydrogenation preferentially at rings **2** and **3** on either side of the molecular center (intermediate 1^* , Fig. 5.1.3g), reducing the maximum conjugation length from an anthracene to a naphthalene segment. If heated to higher temperatures (e.g. $270 \text{ }^\circ\text{C}$), the remaining non-aromatic ring also gets dehydrogenated, rendering heptacene as end-product **5** (Fig. 5.1.3c and f).

Interestingly, the scenario changes substantially in the case of “kinked acene isomers” (Fig. 5.1.4c). Analyzing a sample containing minor amounts of tetrahydroheptaphene, we observed that, in contrast to

the linear counterparts, the saturation of the dihydro intermediates always remains at ring 2 (Fig. 5.1.4b). In this case, any hydrogen migration would reduce the number of Clar sextets in the molecule from three to two (Fig. 5.1.4d), corroborating that the stabilization energy per Clar sextet^{198,221} makes the configuration with the methylenes on ring 2 most favorable.

Also the non-halogenated precursor **1**, still following a similar reaction process as Br-**1**, displays notable differences. As opposed to the Br-**1** case displayed in Fig. 5.1.4a, a similar annealing to 180 °C results in an approximately 80:13:7 ratio of the tetrahydro, dihydro and heptacene species (Fig. 5.1.6). That is, at the same temperature, less molecules display any aromatization, and out of those that do, more aromatize fully into **5**. Besides, the formal methylene migration on reactants and dihydro-intermediates is much less common when starting from **1**. Thus, although the same tendency to minimize the conjugated acene segments through formal methylene migration was reported for closely related non-brominated tetrahydrononacene molecules on Au(111),³⁸ and although an analysis of the detailed mechanism involved in these chemical changes is beyond the scope of this work, it seems evident that the initial presence of radicals after dehalogenation facilitates the first aromatization and lowers the hydrogen transposition barriers.

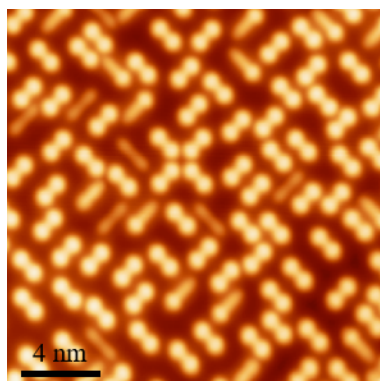


Figure 5.1.6: Constant current STM image of a Ag(001) sample after deposition of **1** and subsequent annealing to 180 °C. The tetrahydro, dihydro and fully aromatized molecular species can be discerned from their two bright lobes, one bright lobe, or no lobes together with a lower apparent height, respectively. [U = 1 V, I = 100 pA]

Within these experiments, we end up with a plethora of different but closely related molecules, offering a good opportunity to probe structure–property relations. At this stage it is important to note that, although with slight differences in the reaction process described above, the structural and electronic characterization performed on single molecules on Ag(001) terraces is similar regardless of whether **1** or Br-**1** is used. That is, we observe the products from a spontaneous hydrogenation of the radical sites resulting from the dehalogenation of Br-**1**. This is of key importance in the analysis and understanding of many surface-supported reactions under vacuum and may be rationalized taking into consideration that hydrogen makes up for most of the residual gas present in UHV chambers and may be additionally generated by nearby dehydrogenation events.

We have recorded dI/dV STS spectra on each of those different molecules for comparison. The results are summarized in Fig. 5.1.7a, placed in order according to the molecule’s longest conjugated segment, which is known to host most of the electron densities of the highest occupied molecular orbital (HOMO) and the lowest unoccupied molecular orbitals (LUMO) (Fig. 5.1.8).³⁸ Thus, we start from **1'**, displaying naphthalene as the largest conjugated segment, followed by **1** and **4** (anthracene), **3** (tetracene), **2** (pentacene) and **5** (heptacene).

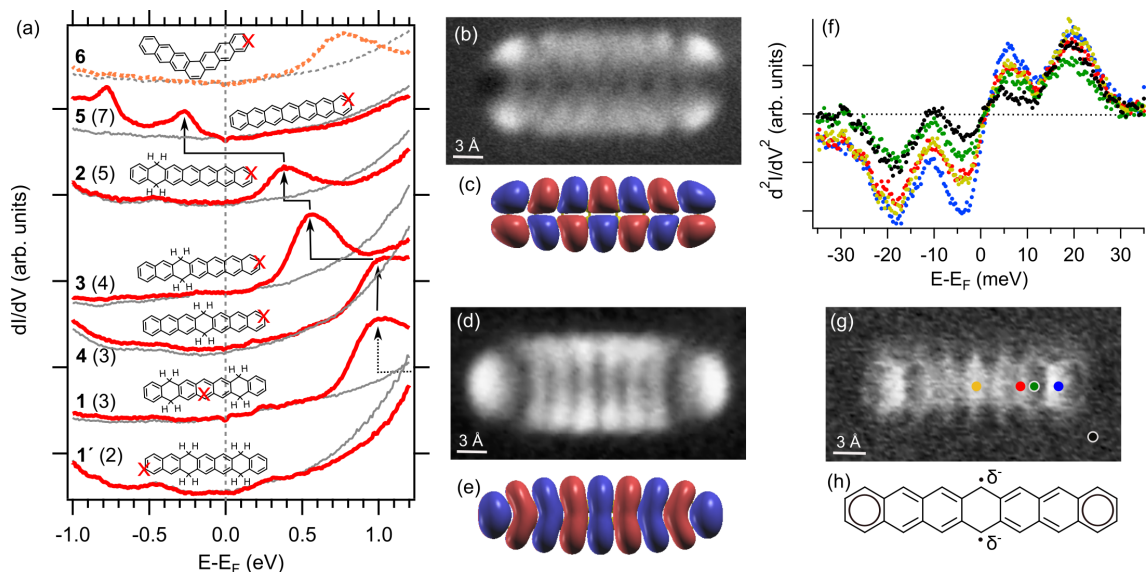


Figure 5.1.7: (a) dI/dV point spectra on reactants, intermediates and end-products, as well as heptaphene **6** (colored lines) at positions as marked on the accompanying models and the associated reference substrate spectra (grey lines). The number of rings in the longest conjugated segment is given in brackets and the LUMO position is marked with arrows. Conductance maps ($I = 180$ pA, $U_{osc} = 10$ mV, and $\nu = 341$ Hz) of **5** at -0.76 V (b) as well as at -0.25 V (d) and its calculated gas-phase wavefunction of the HOMO (c) and the LUMO (e). (f) d^2I/dV^2 spectra ($U_{osc} = 2$ mV and $\nu = 341$ Hz) at the positions marked in (g), revealing the frustrated translational and rotational modes of the CO on the functionalized tip at around 3 and 20 meV, respectively. (g) Inelastic electron tunneling spectroscopy map (const. z , $U_{osc} = 7$ mV, and $\nu = 341$ Hz) of **5** at 3.5 mV. (h) Schematic model of the open-shell heptacene structure, with the associated radicals partially stabilized by additional electron charges.

For the sake of comparison, we also add heptaphene (**6**), the fully conjugated kinked isomer of heptacene (**5**). The HOMO–LUMO gap is known to decrease with the size of acenes,^{38,207,214} as also reproduced with density functional theory calculations of these specific molecules (Fig. 5.1.8). Although experimentally we have only accessed the LUMO for most of the probed molecules, it can be nicely observed how it approaches the Fermi level as the largest conjugated segment increases in size from **1** to **2**. [The exception is **6**, whose additional Clar sextet with respect to **5** brings about an increased stability, a concomitant increase in its gap and thus a LUMO resonance at a higher energy. At this point, it is important to remark that the spectra of **2** showed a notable variability that will be analyzed in the next section of this chapter].

Following the same trend, the shift from **2** to **5** occurs by crossing the Fermi level, concurrently with the appearance of a second occupied resonance. Conductance maps at the corresponding energies (Fig. 5.1.7b and d) reveal their resemblance with the calculated gas-phase wavefunctions of the HOMO and LUMO (Fig. 5.1.7c and e), with slight differences in representations stemming from the mixed *s*- and *p*-wave character of the CO-functionalized probe used for the characterization.⁷⁵ These data are thus clear evidence of the charging of heptacene on Ag(001) by the filling of its former gas-phase LUMO.

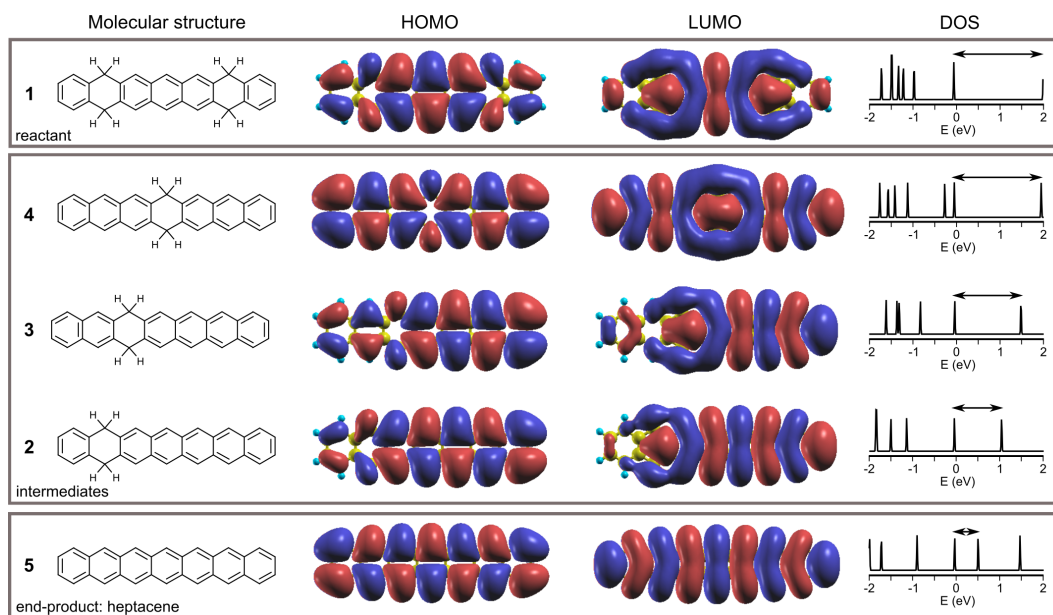


Figure 5.1.8: Molecular structure, calculated wavefunctions for gas-phase HOMO and LUMO of reactant, intermediates and product. The right-most column additionally displays the density of states of the respective molecules, with the HOMO level at 0 as reference, revealing how the LUMO shifts to higher energies (increasing the HOMO-LUMO gap, indicated by the arrows) as the longest conjugated segment (which is observed to host most of the HOMO and LUMO density of states) shortens. Interestingly, in line with the experimental observations (Fig. 5.1.7), the gap hardly changes from **1** to **4**, both featuring three rings as the longest conjugated segment.

Such important charge transfer suggests a strong molecule–substrate interaction,²²² as opposed to weakly interacting interfaces that rather display a Fermi-level pinning scenario.²²³ The strong interaction is proposed to be promoted by the partial open-shell character of heptacene, whose radicals could be stabilized by the additional electrons as schematically shown in Fig. 5.1.7h. Experimental findings hinting at this particular scenario are the spatial variations in the vibrations of CO at functionalized tips when performing inelastic electron tunneling spectroscopy (IETS).²²⁴ Such vibrations, and in particular the frustrated translational mode occurring at around 3 mV at the silver–CO–tip gap, are strongly dependent on the charge density of the probed sample and show the strongest intensity variations at the outer and central rings (Fig 5.1.7f and g), where the Clar sextets and the partial radical character are expected to be dominantly located.

5.1.3 Conclusion

We have studied the surface-supported synthesis of heptacene on Ag(001). The use of two different precursors has allowed us to learn about the effect of bromine atoms on the properties of molecules and substrates, as well as about the spontaneous hydrogenation of radical sites even under UHV. Spectroscopic analysis of the reactants, intermediates and end-products has evidenced a change in the energy-level alignment associated with the decreasing band gap of the molecules with increasing conjugation size. This trend ends with a charged heptacene, indicative of a strong interaction with the underlying Ag(001) substrate.

5.2 Electronic decoupling of polyacenes from the underlying metal substrate by sp^3 carbon atoms

For the work included in this section, sample preparation, SPM measurements and data analysis were performed in collaboration with Luciano Colazzo, calculations were provided by Roberto Robles and Nicolás Lorente, and the precursor molecules were provided by Ruth Dorel and Antonio M. Echavarren.

5.2.1 Introduction

The ultra-high vacuum environment and the atomically flat metallic surfaces used as substrates provide excellent conditions for molecular characterization of materials produced on surfaces,¹¹⁶ which can be performed at the single molecule level by scanning probe microscopy. However, when adsorbed on metallic surfaces, hybridization of the molecules with the substrate significantly modifies their properties and leads, at best, to a substantial broadening of the orbitals. Thus, a decoupling of the molecules from the underlying metal substrate becomes not only beneficial but often strictly necessary to characterize the intrinsic molecular properties. A notable example thereof are graphene nanoribbons, which do not show any evidence of their predicted spin-polarized states when adsorbed on metals, but show the associated correlations gaps as soon as they are electronically decoupled from the substrate.^{9,41} With this decoupling aim, a variety of methods have been applied. Examples include the intercalation of new species between metal and adsorbate (extensively used, *e.g.*, in graphene-based research),^{225–227} or the use of metal-supported insulating buffer layers as substrates.^{9,41,75,228} The chemical addition of bulky side groups to the molecular structure of interest, which can act as molecule–substrate spacers and thereby reduce their coupling strength, has also been proved successful.^{229–231} The efficiency of this self-decoupling strategy is generally poor due to the flexibility of the carbon backbones, which allows them coming close to the substrate by molecular deformations.²²⁹ Nevertheless, it has been sufficient, *e.g.*, to regain the functionality of molecular switches that is otherwise quenched by the stronger interaction with the substrate.²³² Herein, starting from the tetrahydroheptacene precursor used in the previous section, we report the decoupling of polyacenes from an underlying Ag(001) surface by exploiting the non-planarity of the organic backbone imposed by sp^3 -type functional groups. Interestingly, this approach could easily be extrapolated to other organic species and thereby allow important advances in timely research fields like carbon-based magnetism.^{10,78,233–237}

5.2.2 Results and discussion

Hydrogenated polyacene derivatives are stable molecules that can be easily deposited onto clean surfaces by sublimation under UHV conditions and have been used as starting reactants for their transformation into acenes by controlled dehydrogenation. As reported in the previous section (ref. [39]) and in ref. [38,214]. As can be discerned in Fig. 5.2.1a, b, the hydrogenated rings (imaged by scanning tunneling microscopy (STM) with CO-functionalized probes in the repulsive regime as larger rings (Fig. 5.2.1c, d)) feature sp^3 hybridized carbon atoms that break the conjugation along the molecule. It has been demonstrated that the energy gap between the highest occupied molecular orbital (HOMO) and lowest unoccupied molecular orbital (LUMO) of such molecules is ultimately determined by the longest conjugated acene segment, and is remarkably similar to the bandgap of acenes of the same length.^{38,39,214} That is, the dihydrogenated heptacene derivative displayed in Fig. 5.2.1b, d, which has been obtained from the controlled tip-induced dehydrogenation of 5,9,14,18-tetrahydroheptacene precursors (Fig. 5.2.1a, c),³⁹ features five rings as the longest conjugated segment and is characterized by a bandgap similar to that of pentacene.³⁹ Evidence of the similar electronic properties of 5,18-dihydroheptacene (hereafter referred as dihydroheptacene) and pentacene is provided in Fig. 5.2.1e–h, which display calculated low-energy states for the molecules adsorbed on Ag(001). In the case of pentacene, they strongly resemble the LUMO (Fig. 5.2.1e) and HOMO (Fig. 5.2.1g) of free-standing pentacene,⁷⁵ and the analogous calculations for dihydroheptacene (Fig. 5.2.1f, h) reveal a striking similarity. As such, dihydroheptacene can also be considered a “functionalized pentacene” (2,3-alkylpentacene).

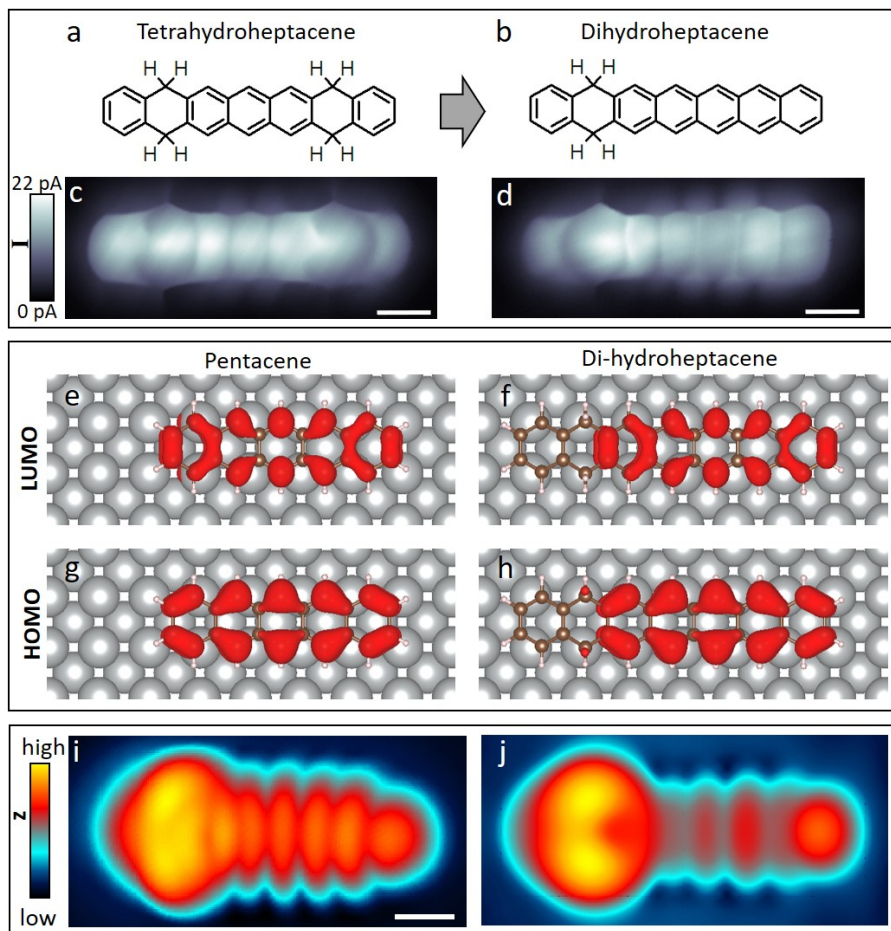


Figure 5.2.1: Chemical structure of 5,9,14,18-tetrahydroheptacene (a) and 5,18-dihydroheptacene (b). Constant height scanning tunneling microscopy (STM) images (sample bias $U = 2$ mV, scale bars = 3 \AA) with CO-functionalized probes of 5,9,14,18-tetrahydroheptacene (c) and 5,18-dihydroheptacene (d).

Calculated charge densities associated with the highest occupied (HOMO) and lowest unoccupied molecular orbital (LUMO) of pentacene (e, g) and 5,18-dihydroheptacene (f, h). Constant current STM image (imaging parameters: $U = 20$ mV, $I = 100$ pA, scale bar = 4 \AA) of 5,18-dihydroheptacene (i) and a simulated STM image of the 5,18-dihydroheptacene LUMO level (j). Note that the differences between experiment (i) and theory (j) arise from the s-wave probe used in the simulations vs. the p-wave character of the CO-functionalized probe used in the measurements.⁷⁵

Previous studies of pentacene on Ag(001) have shown the energy-level alignment to be such that the LUMO is aligned with the Fermi energy and consequently partially occupied with an estimated charge of 0.7 electrons.²³⁸ Any charge transfer-related magnetism is hindered by the substrate: the LUMO is substantially broadened by hybridization with the metal, and the high level of screening reduces electron correlations.^{81,239} In contrast, when the molecule is electronically decoupled from the underlying Ag(001) by a MgO bilayer, the integer charge transfer of one electron to pentacene confers the system a net spin $S = 1/2$ and two spin-split resonances of the former LUMO above and below the Fermi level (the singly occupied (SOMO) and singly unoccupied (SUMO) molecular orbitals, respectively).²³⁸

Focusing now on dihydroheptacene on Ag(001), the contrast in STM measurements at low bias values close to the Fermi level (Fig. 5.2.1i) resembles the simulated image of the molecular LUMO (Fig. 5.2.1j). This underlines again the similarities of dihydroheptacene with pentacene in terms of molecular bandgap and energy-level alignment, with the LUMO energy around E_F . However, it is important to note that there is a great variability in the scanning tunneling spectroscopy (STS) measurements of dihydroheptacene. Figure 5.2.2 shows some examples thereof.

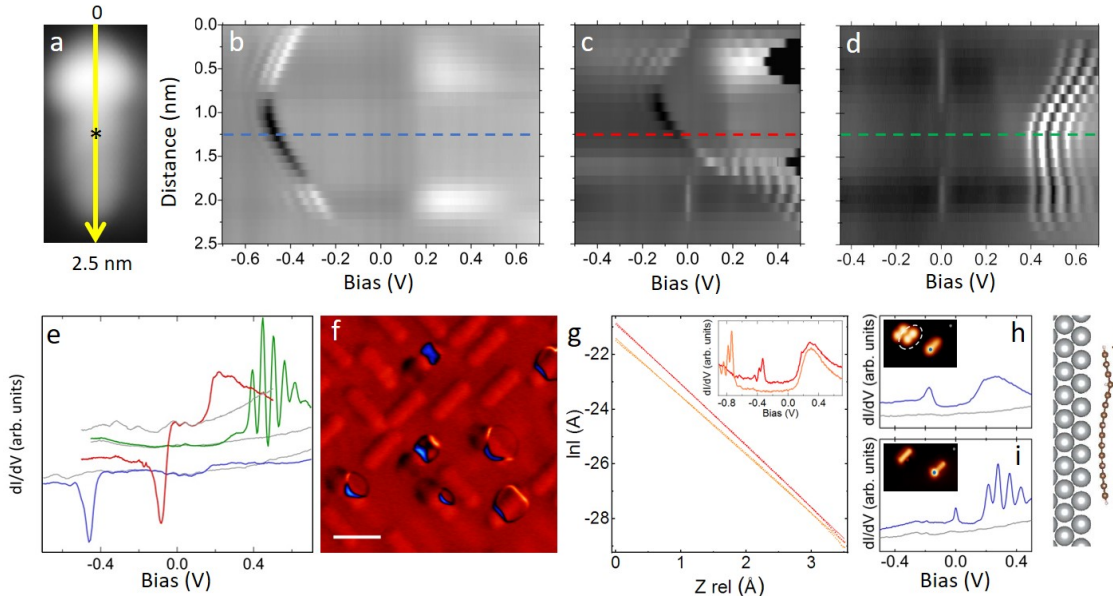


Figure 5.2.2: (a) Constant current scanning tunneling microscopy (STM) image of 5,18-dihydroheptacene. Stacked differential conductance (dI/dV) point spectra with color-coded signal (at each point the feedback loop is adjusted to sample bias (U) and current (I) tunneling parameters $U = 200$ mV, $I = 200$ pA (b), $U = 50$ mV, $I = 250$ pA (c), and $U = 50$ mV, $I = 100$ pA (d)). Each panel corresponds to measurements on different molecules sharing the same structure along a trajectory similar to that outlined by the yellow line in a. (e) Selected dI/dV point spectra extracted from b–d at the position of the dashed lines (colored accordingly in b–d) and the asterisk in a. (f) Constant current dI/dV map (imaging parameters $U = -80$ mV, $I = 200$ pA, scale bar = 2 nm) of a sample containing multiple molecular species including several 5,18-dihydroheptacene molecules. (g) Current (I) vs. the relative tip height distance z spectra on two different 5,18-dihydroheptacene molecules. The reference for z is the tip-sample distance at which the feedback was opened on either molecule, with tunneling parameters $U = 20$ mV, $I = 780$ pA for the red curve and $U = 20$ mV, $I = 388$ pA for the orange curve. The inset displays the associated dI/dV spectra on those same molecules. (h) dI/dV point spectrum on a 5,18-dihydroheptacene molecule (blue line) and a reference spectrum on the substrate (gray line) at the positions marked by accordingly colored points in the inset. (i) Similar dI/dV point spectra taken at the same positions after functionalizing the tip with the 5,9,14,18-tetrahydroheptacene molecule marked with the white oval in the inset of h. (j) Structure of 5,18-dihydroheptacene relaxed on Ag(001) as simulated by density functional theory. All dI/dV spectra and maps are acquired with a Lock-in frequency $\omega = 731$ Hz and amplitude $U_{osc} = 10$ mV, except $U_{osc} = 5$ mV for d.

Figure 5.2.2a shows a representative dihydroheptacene molecule, marking the typical trajectory along which we record dI/dV point spectra. Stacking their color-coded signals make up datasets like those shown in Fig. 5.2.2b–d, which correspond to three different molecules (further examples taken at constant constant height over the molecule are displayed in Fig. 5.2.3), although all of them sharing the same chemical structure displayed in Fig. 5.2.1b.

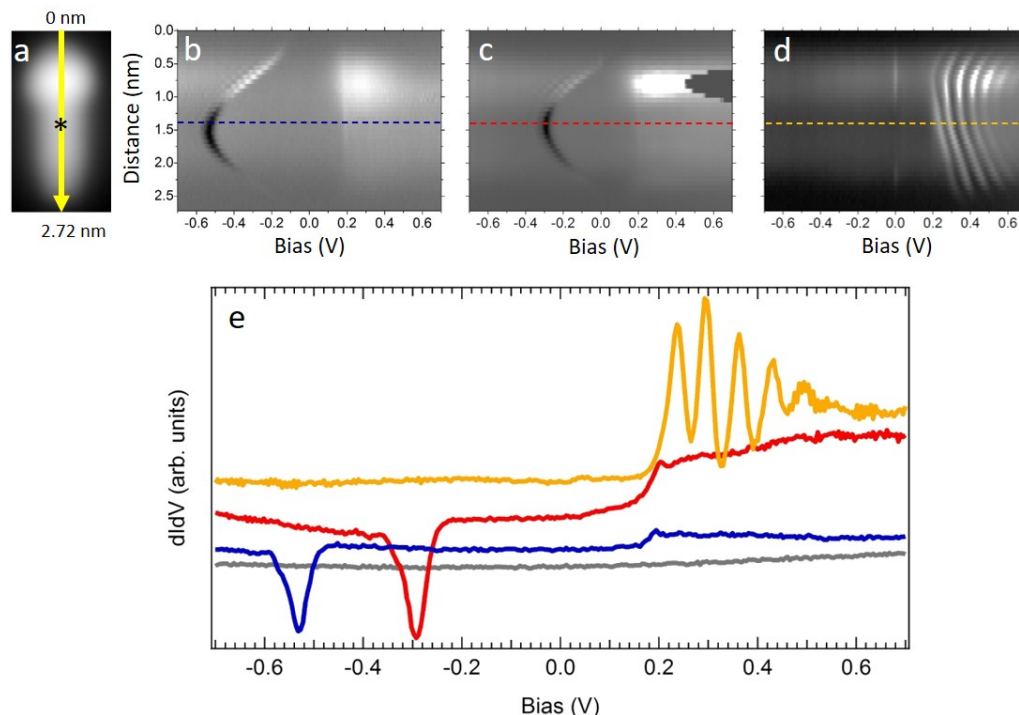


Figure 5.2.3: (a) Constant current image of dihydroheptacene, marking with the yellow line the typical trajectory along which the point spectra are acquired that make up the following panels. (b-d) Stacked point spectra with color-coded dI/dV signal obtained at constant height. The spatial coordinate in the vertical axis is plotted to approximately coincide with the yellow line in panel (a). Panels (b) and (c) correspond to measurements on two different molecules sharing the same structure, while panels (c) and (d) correspond to data acquired on the same molecule with two different tips. (e) Selected dI/dV point spectra extracted from panels (b-d) at the position of the correspondingly colored dashed lines and of the asterisk in panel (a), along with a typical reference spectrum measured on the Ag(001) surface next to the molecules (grey line). Feedback opened for the initial spectra on the surface at 700 mV and 70 pA. $U_{osc} = 5$ mV.

Sample spectra corresponding to the dashed lines (and to the position marked in Fig. 5.2.2a) are shown in Fig. 5.2.2e. Beyond their markedly different appearance, all datasets present sequences of sharp peaks that shift in position along the molecule. The narrow width of the peaks, their observation beyond the limits of the molecule with a ring-like appearance (*i.e.*, near the molecule but on the bare substrate, Fig. 5.2.2f), the electric field dependence of their energy alignment as evidenced by varying tip-sample distance (Fig. 5.2.4), varying supramolecular environment (Fig. 5.2.2f, g), or varying tips (Fig. 5.2.2h, i), all together provide unambiguous proof of their nature, namely so-called charging resonances (and associated vibronic satellites²⁴⁰) related to a double tunneling barrier.^{240, 241}

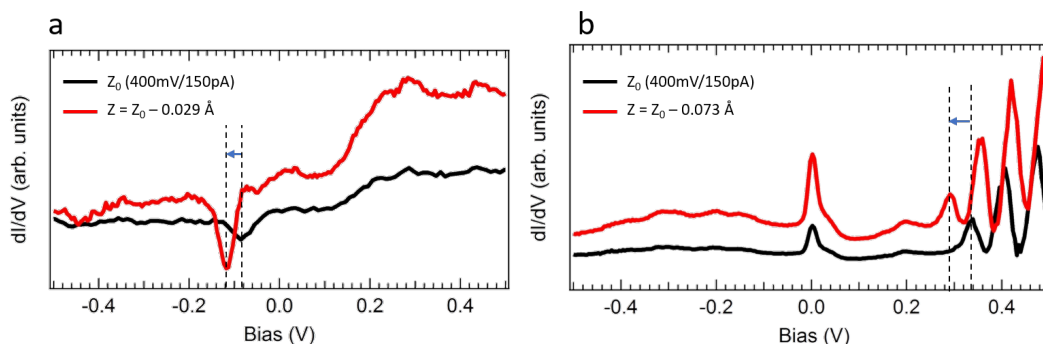


Figure 5.2.4: Selected point spectra displaying the charging resonances at negative (a) and positive (b) bias values, in each case measured at two different tip-sample distances. Regardless of whether the charging resonance appears at negative or positive bias, it shifts to lower energies as the tip-sample distance is reduced.

The presence of a double tunneling barrier implies an effective decoupling of the molecule from the

underlying substrate, which is neither expected from molecules in direct contact with transition metal surfaces nor observed for the closely related pentacene on Ag(001).

Here, the key to rationalizing this surprising finding is the presence of the hydrogenated sp^3 C atoms of dihydroheptacene. According to density functional theory (DFT) calculations, in the gas-phase the molecule presents a completely planar C backbone in which the two H atoms bound to each of the sp^3 C atoms protrude to either side of the plane. Upon adsorption on Ag(001), the symmetry is broken and the hydrogen atoms point toward the surface are repelled by steric repulsion. This causes a nonplanarity of the molecule as shown in Fig. 5.2.2j, which in turn sufficiently reduces its electronic coupling from the substrate to generate the double barrier in the tunneling process.

In a conventionally pictured double barrier at zero sample bias, there is no electric field across the tunneling junction (Fig. 5.2.5a, b). When a positive sample bias U is applied, an electric field is established and a fraction α of the associated potential drops across the barrier between substrate and molecule (Fig. 5.2.5c). As a consequence, the molecular orbitals shift up in energy with respect to the substrate's Fermi level by αU . There is a bias threshold U_{th} at which an occupied orbital initially with a binding energy BE can eventually cross the Fermi level ($\alpha U_{th} = BE$) and cause the transfer of an electron to the substrate (Fig. 5.2.5d). If the tip-sample distance is reduced (Fig. 5.2.5e), the fraction of voltage dropping across the tip-molecule barrier becomes larger, requiring lower bias values to reach the charge transfer threshold (Fig. 5.2.5f). A symmetrically opposite scenario would apply at negative sample bias.

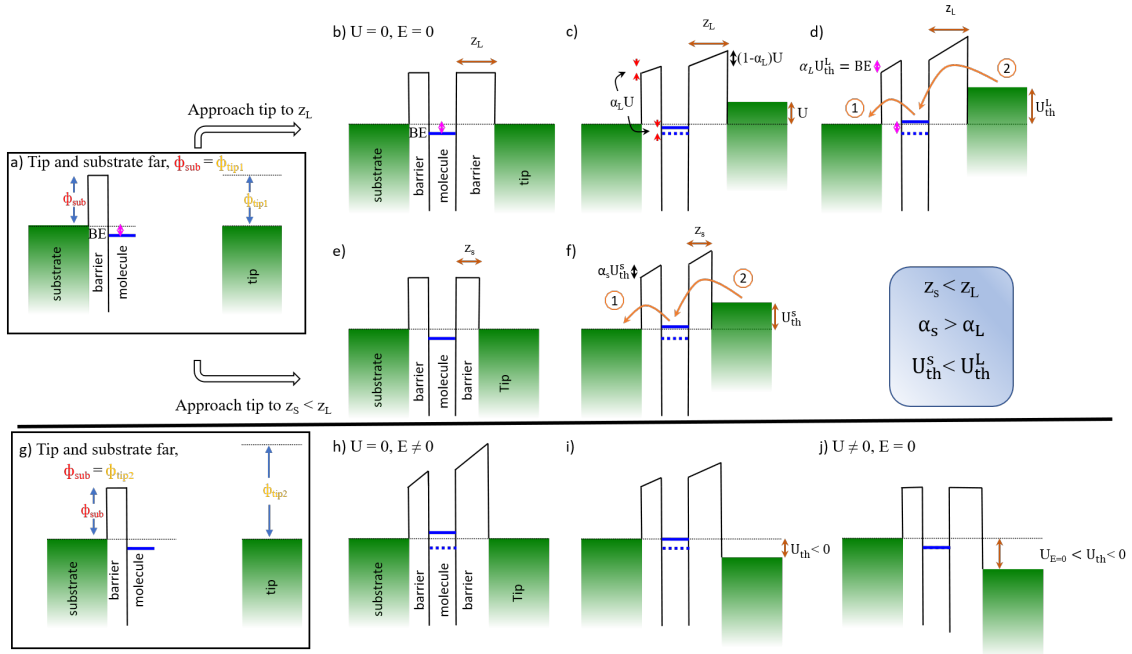


Figure 5.2.5: (a) The barrier's elements are a molecule with an occupied molecular orbital at a binding energy (BE) marked by a blue line, adsorbed on a substrate of workfunction ϕ_{sub} , and a tip of workfunction $\phi_{tip1} = \phi_{sub}$, which are initially far from one another. (b) Energy diagram after bringing the tip into a tunneling distance z_L of the molecule at zero bias U and zero electric field E and (c) after application of a sample bias U , displaying a potential drop of αU across the molecule-substrate barrier. (d) Diagram at the charging bias threshold U_{th}^L , at which a tunneling current sets in that is associated with an initial electron transfer from the occupied molecular orbital to the substrate (1), followed by an electron transfer from the tip to the transiently unoccupied orbital (2). (e) Comparative energy diagram with a smaller tip-molecule distance $z_s < z_L$ without and (f) with an applied bias that coincides with the charging threshold $U_{th}^s < U_{th}^L$ at which a similar electron tunneling scenario sets in as described for d. The associated proportionality of the potential drop across the molecule-substrate barrier α is larger for smaller tip-sample distances ($\alpha_s > \alpha_L$). (g) Double tunneling barrier elements featuring a tip with larger workfunction $\phi_{tip2} > \phi_{sub}$. (h) Electric field E and shift of the formerly occupied molecular orbital energy by $\alpha(\phi_{tip2} - \phi_{sub})$ to an energy above the Fermi level as the tip is approached to the sample even in the absence of an applied bias U . (i) Diagram at the negative sample bias threshold for the orbital's charging. (j) Diagram at the negative bias required to nullify the electric field E across the double tunneling barrier.

In our measurements, the charging resonances shift in the same direction (to lower sample bias values) when reducing the tip-sample distance (Fig. 5.2.4) and display the same concave curvature in the stacked spectra regardless of whether they appear at positive (Fig. 5.2.2d) or negative (Fig. 5.2.2b) bias. In fact, the curved charging resonance trajectory along the molecule often crosses the Fermi level (Fig. 5.2.2c).

This is inconsistent with the common assumption of a zero electric field at zero bias and instead implies that, at least in cases like Fig. 5.2.2b, c, the zero electric field condition occurs at negative sample bias, in particular more negative than the “charging peak parabola” onset. This is understood in a straightforward manner assuming different work functions for tip and sample (Fig. 5.2.5g), which establish a contact potential difference and the associated electric field when brought into tunneling distance (Fig. 5.2.5h). Under these circumstances, the charging threshold may indeed be observed at negative bias values (Fig. 5.2.5i) and the zero electric field bias (Fig. 5.2.5j) corresponds to that typically measured in Kelvin probe force microscopy, which in most of the cases differs from zero and varies with both tip and sample.²⁴²

We can thus now conclude that for this system, the charging resonance involves in all cases (whether at positive or negative bias values) the same molecular orbital, namely the LUMO. It is close in energy to E_F and can thus be easily brought across the substrate’s Fermi level by electric fields at the tunneling junction. At the time of the tunneling event across the tip-molecule barrier, the LUMO is empty or occupied at bias values above or below that of the charging resonance, respectively. For that reason, whenever the zero bias point coincides with a molecule in its charged state (occupied LUMO), an additional zero bias resonance appears in the spectra (Fig. 5.2.2c, d), but not if the molecule at zero bias is in its neutral state (Fig. 5.2.2b, c). As opposed to the charging resonances, this zero bias resonance does not shift for varying tip heights (Fig. 5.2.4b) and is a manifestation of the Kondo effect associated with the spin 1/2 of the molecule as a single electron occupies its gas-phase LUMO.^{243,244}

This is confirmed by its anomalously fast broadening with temperature, whose width evolution is in agreement with a Kondo temperature of 73 ± 2 K (see Fig. 5.2.6 and methods section). The presence of this Kondo resonance is further proof of the decoupling effect that the “pentacene functionalization” at C-2 and C-3 with sp^3 carbon atoms brings about. If that were not the case, a broader LUMO level and reduced electron correlations would cause an equal population of spin up and spin down LUMO orbitals,^{81,239} resulting in no net spin and no Kondo peak, as occurs with pristine pentacene.²³⁸ On the other hand, the Kondo resonance still implies a minor molecule–substrate coupling, since it relates to the screening of the molecular spin by the substrate electrons and would thus be absent for a more efficient decoupling as observed for pentacene on an insulating MgO buffer layer. We can thus conclude that on Ag(001), the “pentacene functionalization” by sp^3 carbon atoms results in sufficiently decoupled molecules to show charging resonances and stabilize a singly charged molecule with net spin 1/2, but with sufficient molecule–substrate interaction to reveal a Kondo resonance. In other words, more decoupled than pristine pentacene on Ag(001) but, as could be expected, less than pentacene on a MgO bilayer on Ag(001).

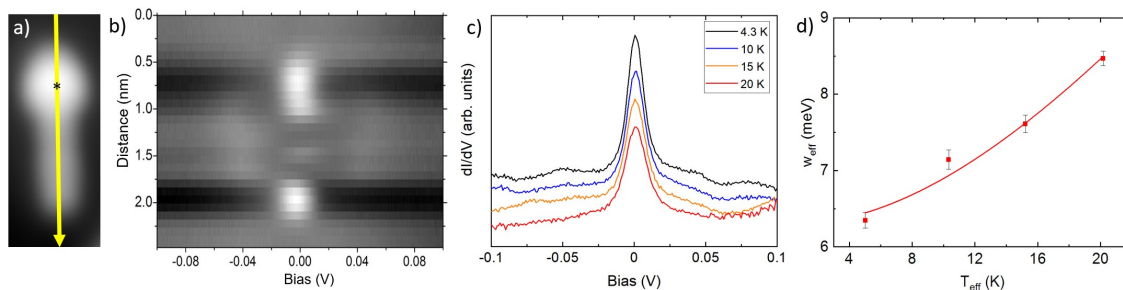


Figure 5.2.6: Constant current image of dihydroheptacene (a), marking with the yellow line the trajectory along which the point spectra are acquired that make up panel (b) when stacked into a color-coded map (Feedback opened at $U = 50$ mV / $I = 1$ nA, Lock-in $U_{osc} = 1$ mV). (c) dI/dV spectra of the Kondo resonance at varying temperatures taken at the position marked with an asterisk in panel (a) (Feedback opened at $U = 100$ mV / $I = 1$ nA, Lock-in $U_{osc} = 1$ mV). (d) Effective width of the zero-bias resonance as a function of the effective temperature (see details in Supplementary Note 1) and a fit to the Fermi-Liquid model (solid line) corresponding to a Kondo temperature of 732 K. The error bars correspond to the standard deviation scaled with square root of reduced Chi-square

A question that arises at this point, however, is where the large variability displayed by the charging resonances comes from. Being an electric field-driven effect, it largely depends on the tip, on the sample, as well as on the contact potential difference between them. Different tips (in terms of shape, but also tip apex functionalization)²⁴² will notably impact the electric field lines within the tunneling junction and thus the charging resonance appearance. By way of example, Fig. 5.2.2h shows the conductance spectrum obtained with a metallic tip on the “functionalized pentacene” molecule marked with a blue point in the inset. The charging peak appears at negative bias. Consequently, at zero bias the molecule is in its neutral state and no Kondo peak is observed. As the tip is functionalized by picking up the molecule marked with the white oval, the tip’s work function and the overall electric field at the tunneling junction change. As a result, a conductance spectrum taken on the same molecule as in panel (h) now shows the charging

resonances at positive bias (Fig. 5.2.2i). The molecule is therefore charged at zero bias at the time of the tunneling between tip and molecule, and consequently displays a Kondo peak.

However, not only the tip matters for the charging resonance appearance, but also inhomogeneities in the sample. The tunneling barrier and the electric field within the tunneling junction are also affected by the polarizability of a molecule's surroundings (neighboring molecules, surface, subsurface defects, etc.).^{223,244–247} Therefore, even with the same tip, molecules sharing the same structure may display different charging peaks.²⁴⁴ A conductance map measured at -80 mV on a variety of hydrogenated heptacene derivatives³⁹ displays, on each of the “functionalized pentacene” molecules, charging rings with different shapes and sizes that are even centered on different molecular positions (Fig. 5.2.2f). Similar changes are found for a same molecule after tip manipulation to another epitaxially equivalent substrate position. STS data acquired with the same tip on equivalent positions of different “functionalized pentacene” molecules are shown in Fig. 5.2.2g. The inset displays the dI/dV spectra, revealing charging resonances at very different bias values. Associated I vs. z curves taken at the same positions reveal the expected linear behavior when the current is plotted logarithmically, and notably different slopes (Fig. 5.2.2i). The slopes correlate with the effective barrier at the tunneling junction, which is typically associated with an average of tip and sample workfunction.²⁴⁸ The tip being the same, we can conclude that the change in the effective barrier relates to local inhomogeneities in the substrate²⁴⁴ and/or local supramolecular environment,^{223,245–247} resulting in this particular case in a 0.51 eV larger effective tunneling barrier and 0.4 V lower charging bias threshold for the molecule associated with the red curves.

When the charging resonances occur at positive bias, they appear everywhere as a sharp maximum (Fig. 5.2.2d). Interestingly, the charging resonances at negative bias instead show a location-dependent appearance, namely as a peak near the molecular ends and as a dip around the “pentacene” segment's center or on the substrate (Fig. 5.2.2b, c). The same effect can be observed in conductance maps of the charging rings. When they appear at positive bias, the charging rings (and their concentric vibronic satellites) are imaged everywhere as a conductance increase (Fig. 5.2.7a, b). Instead, charging rings at negative bias are imaged with a reduced conductance signal on the substrate, an even stronger reduction around the “pentacene” segment's center, and with an increased conductance signal near its ends (Fig. 5.2.7c, d).

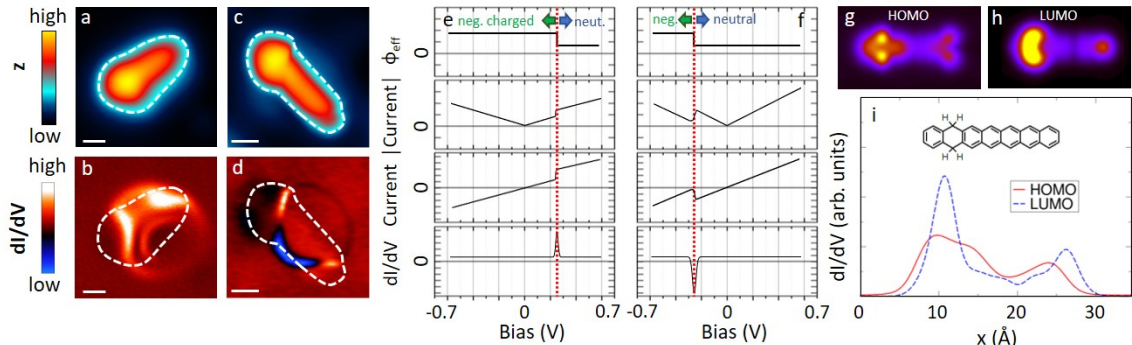


Figure 5.2.7: Constant current scanning tunneling microscopy (STM) (a) and simultaneously acquired differential conductance (dI/dV) signal (b) of a 5,18-dihydroheptacene molecule displaying the charging resonances at positive bias (tunneling parameters in a, b; sample bias $U = 615$ mV, current $I = 80$ pA, lock-in bias oscillation $U_{osc} = 10$ mV); and equivalent STM (c) and dI/dV (d) measurements for a molecule displaying the charging resonances negative bias (c, d; $U = -80$ mV, $I = 200$ pA, lock-in bias oscillation $U_{osc} = 10$ mV). The periphery of the molecule as imaged by constant current STM is marked with a white dashed line and superimposed on the dI/dV images for comparison. The associated scale bars correspond to 5 Å in all four images and the color scales are displayed on the left. Schematic graphs of the expected current modulus, current, and dI/dV signal evolution associated with the effective tunneling barrier modification ϕ_{eff} as a molecule reaches its charging threshold (marked by a red dotted line) at positive (e) and negative bias (f). Simulated dI/dV maps at 10 Å above the molecular plane at the highest occupied (HOMO) (g) and lowest unoccupied molecular orbital (LUMO) (h) energies. (i) Comparative cross section of the calculated dI/dV signal along the long molecular axis at 10 Å above the molecular plane (the molecular structure inset is drawn to scale for guidance).

We rationalize these findings as follows. As an adsorbate becomes charged with an electron (hole) from the surface, that charge redistribution causes an interfacial dipole that increases (decreases) the effective tunneling barrier. In our experiments, at bias values below that of the charging resonance, the tunneling process between tip and molecule involves a molecular species charged with an extra electron. Such charge

transfer causes an interface dipole that increases the tunneling barrier and thus reduces the associated tunneling current. As the molecule becomes neutral at higher bias values, the barrier decreases and the tunneling current increases. While at positive bias values, this increase in current results in a sharp peak in the dI/dV signal (Fig. 5.2.7e), a similar increase of the tunneling intensity at negative bias appears as a dip (Fig. 5.2.7f). Taking these considerations into account we would expect the charging resonances to appear everywhere as dips at negative bias and as peaks at positive bias.

However, there is an additional effect to consider. In a singly charged molecule, the lowest energy states are the SOMO and the SUMO, both of them related to the gas-phase LUMO. Instead, for a neutral molecule the frontier orbitals are the HOMO and the LUMO. That is, the unoccupied frontier states for charged and neutral molecules share the same wavefunction symmetry and spatial distribution of the gas-phase LUMO. Thus, for positive bias values on either side of the charging resonance, the orbitals involved in the tunneling (whether resonantly or only through the electronic state's tails) are always dominantly LUMO related.

Focusing on the occupied states, the frontier orbital for charged and neutral molecules relate to the gas-phase LUMO and HOMO, respectively. Thus, for negative bias values, on either side of the charging resonance, two different orbitals with disparate wavefunction symmetry and spatial distribution are involved in the tunneling process. Their decay perpendicular to the surface plane (Fig. 5.2.7g, h) and consequently the tunneling transmission function between tip and molecule is locally very different. At the same tip height, it is the HOMO that provides a larger transmission in the central region of the "functionalized pentacene", while it is the LUMO on the outer sides of the molecule (Fig. 5.2.7i). This has a strong impact on the measured conductance as the charging resonance is crossed, while ramping up the bias and the orbital dominating the tunneling process changes from the gas-phase LUMO to the gas-phase HOMO: the conductance signal near the molecular ends increases, whereas it decreases near the center of the "pentacene" segment.

This effect is convoluted with that described earlier of the different tunneling barrier at either side of the charging resonance. At negative bias, the latter imprints a dip-like appearance to the charging resonances on the substrate nearby the molecules (Fig. 5.2.7d). As the tip moves onto the molecules and the molecular orbitals become directly involved in the tunneling process, the modified tunneling transmission promotes the dip on the central region of the molecule (Fig. 5.2.7d). In contrast, on the outer regions of the molecule it reduces the current as the charging threshold is crossed, compensating and even reverting the effect of the lower effective tunneling barrier on neutral molecules, thus finally appearing as a dI/dV peak in those regions.

5.2.3 Conclusion

Besides providing an understanding of why charging resonances appear as peaks or dips depending on the polarity and spatial location on the molecules, we have characterized the critical effect of sp^3 carbon atoms along the backbone of acene derivatives on their electronic decoupling from the supporting substrates. The non-planarity imposed by the sp^3 carbon atoms drives an electronic decoupling from the underlying substrate that has been shown to be sufficient to establish a double tunneling barrier and stabilize a singly charged molecule holding a net spin $S = 1/2$. Importantly, although the experiments have been performed on hydrogenated heptacene molecules, this concept may be transposed to many other polyaromatic hydrocarbons of great scientific interest.

5.3 From starphenes to non-benzenoid linear conjugated polymers by substrate templating

For the work included in this section, sample preparation, SPM measurements and data analysis were performed in collaboration with James Lawrence and Alejandro Berdonces-Layunta, calculations were provided by Pedro Brandimarte and Daniel Sánchez-Portal, and the precursor molecules were provided by Fátima García, Dolores Pérez, and Diego Peña.

5.3.1 Introduction

Performed on well-defined surfaces and under ultra-high-vacuum conditions, on-surface methods have been shown to allow for the synthesis of materials unachievable by conventional wet chemistry alone.^{233, 235, 249} One such example are higher acenes, whose open-shell character—as discussed earlier in this chapter—increases as the number of fused benzene rings grows.^{208, 210} This compromises their stability and makes their synthesis challenging.²⁰⁴ One way to overcome the stability limitations is an inert environment like ultra-high-vacuum,^{38, 215} which has indeed allowed the synthesis of the longest acenes to date.¹² However, the synthesis of even longer acenes still remains an open challenge in spite of its notable interest from both fundamental and application oriented viewpoints, the limiting case being the narrowest possible zigzag-oriented graphene nanoribbons.^{9, 250}

In addition to the homogeneous infinite polyacene, other linear acene-based polymers display similarly attractive properties, which can range *e.g.* from ultra-low band gaps¹⁵⁴ to spin-polarized bands.¹⁵¹ In fact, even finite acene-based molecules attract great interest, as for example in the case of starphenes.^{151, 251} All of the aforementioned structures may potentially be obtained by on-surface synthesis from the reactant **m1** displayed in Fig. 5.3.2a. It includes two halogen atoms and two methyl groups on either side of the anthracene backbone. Both types of functionalization are included among the first groups whose thermal activation was demonstrated to work in “on-surface synthesis” experiments, leading to the controlled and reproducible covalent coupling of reactants.^{252, 253} A cross-coupling between the two different groups of the reactant would result in homogeneous polyacene (Fig. 5.3.2a), whereas homo-coupling would rather result in other acene-based structures like those outlined in Fig. 5.3.2a for the Ullmann coupling case. We have performed on-surface synthesis experiments with the reactant **m1** on two different substrates, namely Au(111) and Au(110). By scanning tunneling microscopy and spectroscopy (STM and STS) we analyze the chemical structure and electronic properties of the reaction products. Because the C-Br bond is activated at lower temperatures than C-H, Ullmann homo-coupling dominates the initial reaction steps independently of the substrate. As depicted in Fig. 5.3.2a, the reaction products can include reactant molecules that are either at an angle (*e.g.* **s1**) or collinearly oriented (*e.g.* **d2**). Importantly, the substrate symmetry determines the reaction outcome: whereas on the flat hexagonal Au(111) surface the reaction products include both linear and non-linear (“two-dimensional”) molecules with a pronounced favoritism for molecular trimers (**s1**), on the 2×1 Au(110) reconstruction its linear trenches act as templates that limit the reaction products to collinearly fused reactants (*e.g.* **d2**). That is, the substrate templating can be used to steer the reaction outcome and the product’s azimuthal alignment.

5.3.2 Results and discussion

The deposition of **m1** has been performed onto Au(111) and Au(110) substrates held at RT. Under such conditions, the molecules remain intact on both surfaces and self-assemble into structures as shown in Fig. 5.3.1. On Au(111), the molecules show a remarkable tendency to form three-fold symmetric trimers (Fig. 5.3.1b) in which the molecules are aligned along the [1-10] and its two equivalent substrate directions, with the halogen-functionalized side facing towards the trimer’s center (Fig. 5.3.1c).

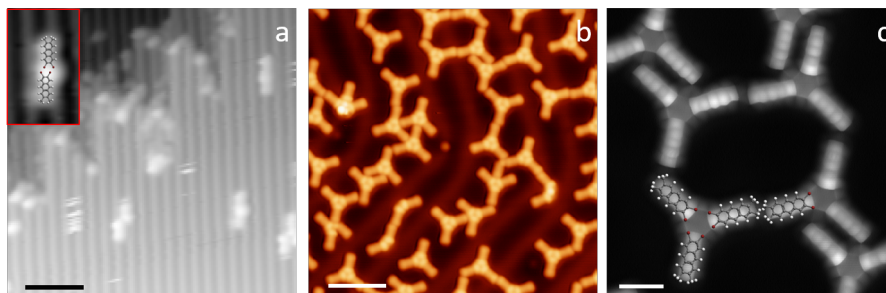


Figure 5.3.1: As deposited molecules: a) STM topography image of the precursor molecules on Au(110) with the molecular model in the inset, b) STM topography image for the molecules on Au(111) and c) constant height STM image with CO-functionalized tip for molecules on Au(111). STM imaging parameters: a) -500 mV/70 pA, b) -500 mV/50 pA, c) 10 mV. Scale bar: a-b) 4 nm, c) 1 nm.

The driving force for such self-assembly is thus the formation of type I halogen bonds.¹⁸⁴ In contrast, on Au(110) the molecules are uniaxially aligned parallel to the 2×1 surface reconstruction. The intact molecules adsorb preferentially on top of the reconstruction's Au rows, with the halogenated side facing each other, although the opposite halogen-to-methyl alignment can also be observed occasionally (Fig. 5.3.1a). Interestingly, as shown in Fig. 5.3.2b,c, the preferred molecules' relative alignment on either substrate is perpetuated as the intermolecular covalent coupling reactions are thermally activated. The carbon-halogen bonds display a lower activation temperature than carbon-hydrogen, causing the initial reactions to be dominated by Ullmann coupling, whose products are depicted in Fig. 5.3.2a.

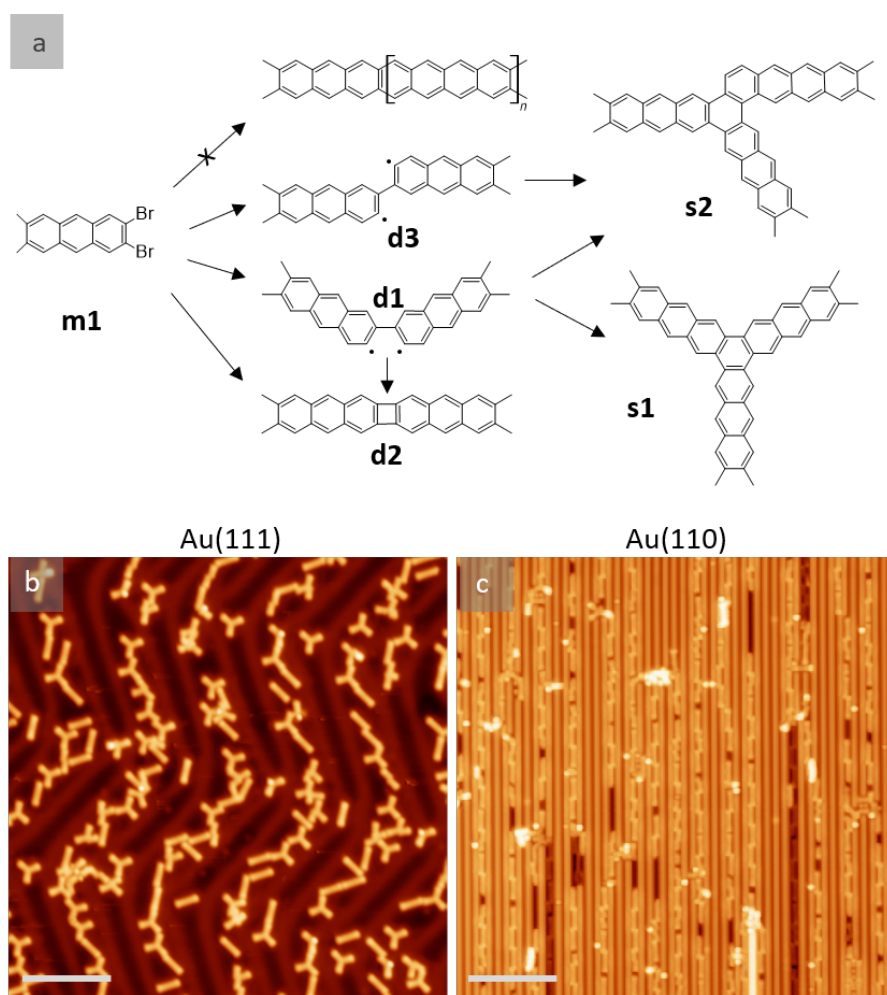


Figure 5.3.2: a) Scheme of the covalently coupled structures on Au(111) and their possible reaction routes, STM overview images of the of the samples on b) Au(111) and c) on Au(110) both after annealing to 525 K. STM imaging parameters: b) -500 mV/ 50 pA, 40 mV/50 pA. Scale bar is 8 nm for b and c.

Only at higher temperatures in the range of 525 K do the methyl groups become activated, leading to the intermolecular coupling of the previously formed Ullmann coupling products (Fig. 5.3.2b-c).

In the following, we analyze in detail the initial reactions observed after annealing to only 425 K. A representative large-scale image after sub-monolayer deposition of **m1** on Au(111) followed by an annealing treatment is shown in Fig. 5.3.3a. The compendium of all observed covalently coupled products is represented in Fig. 5.3.3b-f (some apparently more complex structures observed in Fig. 5.3.3a are just some of these products interacting non-covalently with additional unreacted monomers), and their relative abundance is shown in the histograms of Fig. 5.3.3g,h.

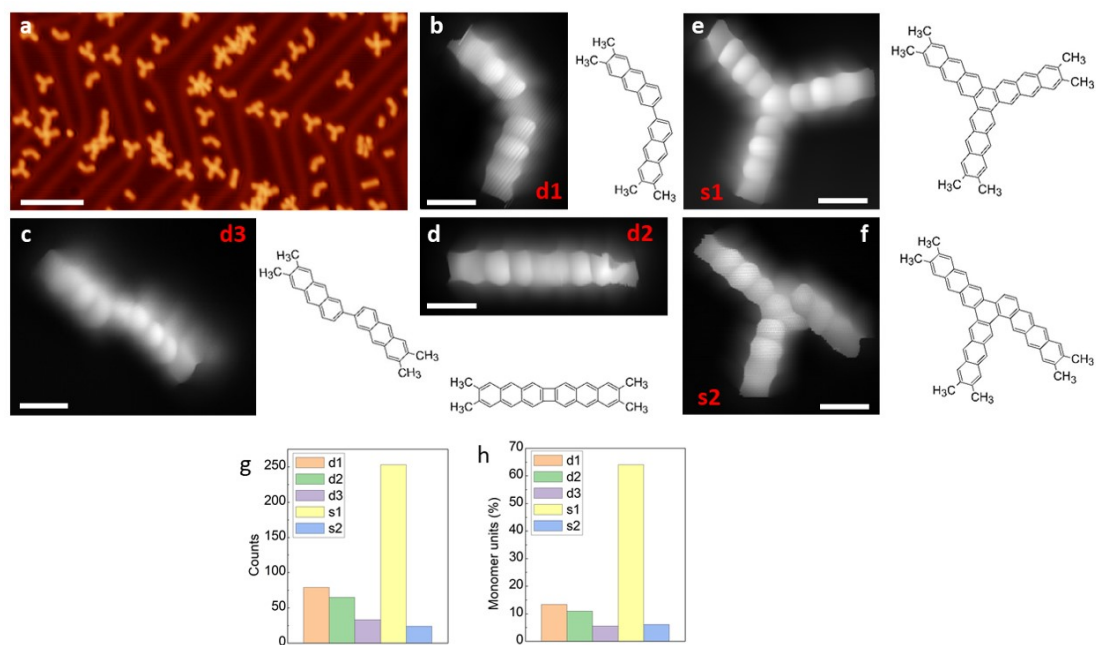


Figure 5.3.3: a) Representative STM overview image of the sample on Au(111) after annealing to 425 K, b-f) constant height STM images with CO-functionalized tip of the covalently linked products and their associated chemical structures, g) statistics of the occurrence for each of the five structures h) monomers units conversion statistics. STM Imaging parameters: a) 500 mV/100 pA, b,c and f) 5 mV, e,d) 10 mV. Scale bar: b) 8 nm, b-f) 5 Å.

Among the products we observe two dimers linked by a single covalent bond that is either on the same molecular side, resulting in a structure with the two acene moieties at an angle of approximately 120 degrees (**d1**, Fig. 5.3.3b), or on opposite sides, resulting in a staggered structure of two collinearly oriented acene moieties (**d3**, Fig. 5.3.3c). The other observed dimer presents two bonds linking the two reactants, forming a four-membered ring in between the anthracene moieties (**d2**, Fig. 5.3.3d). This product may evolve from **d1** by a second bond formation that quenches its remaining radicals, or be the result of a concerted formation of two bonds from two activated **m1** monomers.

Whereas the two new bonds formed with **d2** quench all the four radicals generated with the homolytic cleavage of the halogens of two reactant molecules, the single-bond formation of **d1** and **d3** quenches only two of them. Whether in the observed dimers the remaining radicals are passivated by H of unknown origin (*e.g.* residual H from the UHV chamber) or not remains unknown, but at least no obvious bonding of the σ -radical to the Au substrate is apparent from a molecular tilt that would in principle be associated with it. In any case, structures **d1** and **d3** with remaining radicals are very reactive species that presumably act as precursors for the formation of trimers. Taking the most common dimer **d1** as starting point, the natural addition of a third activated **m1** monomer quenching all radicals would form a three-fold symmetric methyl-terminated [7]-starphene molecule (**s1**, Fig. 5.3.3e). However, an alternative scenario including a hydrogen migration may result in an asymmetric starphene molecule (**s2**, Fig. 5.3.3f). The latter may also be obtained from **d3** under the same conditions: the addition of an activated **m1** monomer and an associated H migration (Fig. 5.3.2a). The product's relative abundance, however, shows that among the dimers the most common is **d1**, while in total numbers there is a dramatic preference for **s1**. The stepwise evolution of **m1** to **d1** and to **s1**, or alternatively a concerted trimerization of **m1** to **s1** thus appear as the presumably most favorable pathways.

It is interesting to compare the electronic properties of the various structures, all consisting of different coupling motifs of the same precursor unit. As reference we thus take the precursor unit. Scanning tunneling spectroscopy measurements on the as-deposited molecules, however, are hindered by their limited stability. Whereas well-defined resonances associated with the occupied states can be observed (Fig. 5.3.4), at positive bias values around 2 eV there is always a sudden jump in the conductance associated with the molecule's chemical changes, in particular with their debromination. The unoccupied molecular orbitals of **m1** are expected to be around those energies and the instability may be actually promoted by the population of the LUMO level upon tunneling. In any case, a proper characterization of the unoccupied orbitals is thus hindered. However, such instability is no longer present in debrominated monomer molecules. Also in this case we can observe a clear resonance from the HOMO level, although shifted by about 0.29 eV towards the Fermi level to an energy of -1.34 eV (Fig. 5.3.4). Halogenation of molecules is a commonly applied method to increase their ionization potential and electron affinity.^{254, 255}

We thus associate the observed shift with the disappearance of the halogens effect as its bond to the molecule is broken. The advantage is that the LUMO resonance can now be nicely resolved as well, with its maximum at an energy of 2.05 eV, resulting in a HOMO-LUMO gap of 3.39 eV. The molecule under study consists of a conjugated anthracene backbone with two additional methyl groups. The sp^3 conjugation of the latter severely limits their contribution to the low energy π -orbitals, (as reported in section 5.2 [57] and in other works^{38,39}) making the molecule's electronic properties comparable to those of pristine anthracene. Anthracene's reported HOMO-LUMO gap is indeed only minorly larger ($E_{gap} \approx 3.6$ eV),¹² and the frontier orbital's appearance²⁵⁶ very similar to that of the frontier orbitals of the hydrogen-passivated **m1** (Figure 5.3.4 h-k).

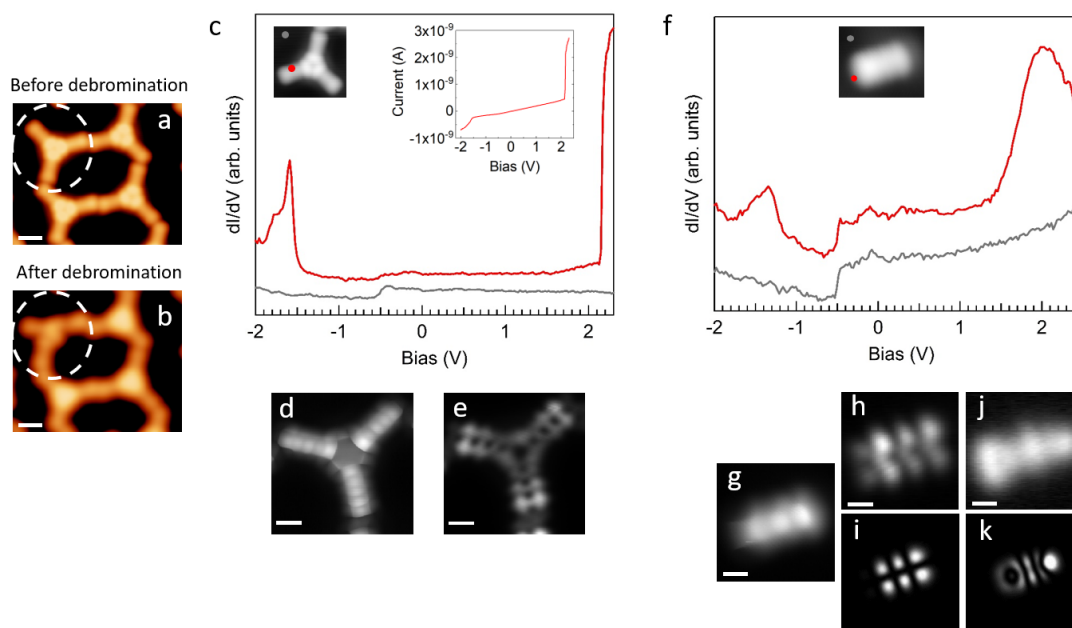


Figure 5.3.4: Electronic properties of the monomer on Au(111). a-b) STM topography images of the monomer before and after tip-induced debromination, c) differential conductance spectra on the brominated monomer at the positions shown in the inset image, inset curve is the corresponding current trace. d) constant height STM image with CO-functionalized tip of a trimer consisting of halogen-assembled monomers, e) corresponding constant height dI/dV map at -1.630 V. f) Differential conductance spectra of the monomer after debromination at the positions shown in the inset image, g) constant height image with CO-terminated tip at 10 of the debrominated monomer, corresponding constant height dI/dV maps at h) -1.340 V and j) 2.050 V, i-k) simulations for the maps in h-j respectively. STM imaging parameters: a) -0.520 V/50 pA, b) -0.500 V/50 pA, d) 10 mV, g) 5 mV. Scale bar: a-b) 1 nm, d-e) 5 Å, g,h,j) 3 Å.

The measurements, however, show a stronger than expected contribution is observed at the methyl positions. Here it needs to be remembered that the density functional theory calculations are performed for gas-phase molecules, according to which the molecule presents a completely planar C backbone with the two H atoms bound to each of the sp^3 C atoms protruding to either side of the plane. Upon adsorption on Au(111) the symmetry is broken and the hydrogen atoms pointing towards the surface are repelled by steric repulsion. This causes the sp^3 carbons atoms to lie higher up (farther from the surface), a distortion that is still noticeable at the nearest sp^2 hybridized carbon atoms of the “anthracene segment” and may even help in decoupling electronically the molecules from the substrate.⁵⁷ This topographic effect translates into a larger STM signal at the higher C atoms and thus into the apparently stronger-than-expected contribution of the methyl groups to the frontier molecular orbitals.

As two such monomers are linked by a single bond into **d1**, both the HOMO and LUMO shift toward the Fermi level to -1.05 eV and 1.82 eV, respectively (Figure 5.3.5). The HOMO-LUMO gap thus shrinks notably to 2.87 eV, as expected from a bonding motif that maintains the conjugation at the inter-monomer level and thus results in an overall extension of the electron conjugation and delocalization.²⁵⁷ A similar coupling with a single bond but with the monomers in a collinear and staggered position (**d3**) results in an only slightly larger gap of 2.97 eV (Figure 5.3.5) with the HOMO and LUMO at -1.12 eV and 1.85 eV, respectively. As the two monomers become linked with two covalent bonds that form a new four membered ring at the junction (**d2**), the changes in the frontier orbital energies is not so pronounced either. The HOMO remains at -1.14 eV and the LUMO displays a downward shift to 1.66 eV, which results in

a gap of 2.8 eV (Figure 5.3.5). This implies a change of only 70 meV with respect to **d1**, which can be understood as having a relatively similar electron delocalization in both cases.

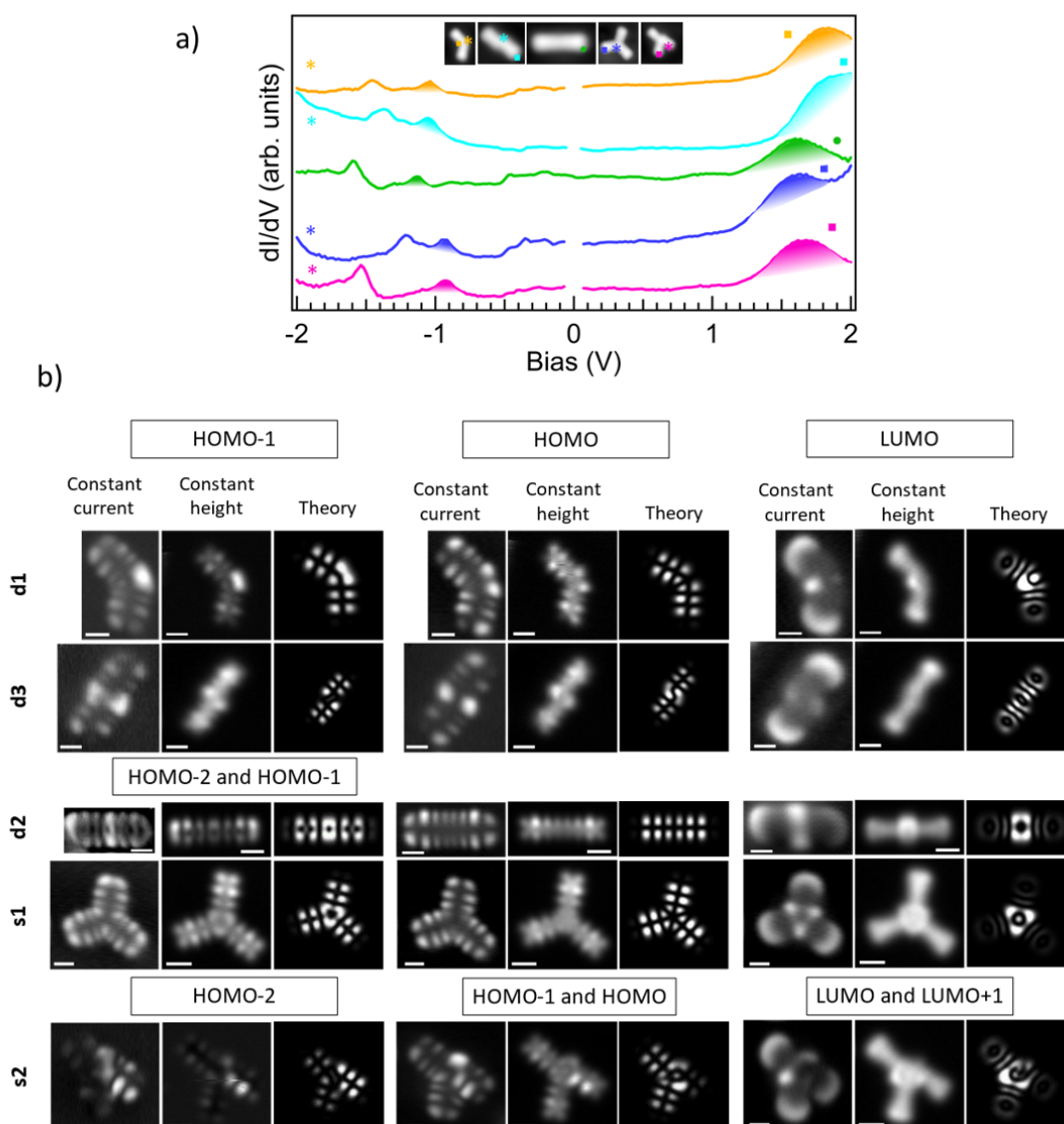


Figure 5.3.5: a) Differential conductance point spectra of the five covalently coupled structures on Au(111), the inset with the color code show where each of the spectra is taken on the molecule. b) Constant height and constant current dI/dV maps of the frontier molecular orbitals of the five covalently bonded products on Au(111) comparing experimental data to theory for each. Scale bar is 6 Å.

The overall appearance of the HOMO and LUMO molecular orbitals in the dI/dV experimentally observed maps and wavefunctions calculations features a nodal plane along the long axis of each acene segment at the HOMO energies, and banana-like intensities perpendicular to the acene segment's long axis at the LUMO energy. Closely related acene-based systems indeed show similar electronic features.^{39,258} This is valid for the products on Au(111) as in Figure 5.3.5 as well as for those obtained on Au(110) surface (discussed later on).

Note that there is an intensity variation at position of the 4-membered rings and at the coupling junctions. Still the experimental data show a nice agreement to those anticipated by theory, as shown in Figure 5.3.5b) comparing the frontier orbitals mapped by different STM scanning modes compare to theory for the five covalently coupled products on Au(111) surface. With the particularity of **s2** molecule mapping discussed in the next paragraph.

As the molecules form trimers, the electron delocalization is expected to increase further and thus the gap to shrink accordingly. That is indeed the case. For the methyl-terminated [7]-starphene molecule **s1**, whereas the LUMO remains hardly unchanged at 1.64 eV, the HOMO level shifts upward to -0.94 eV and

thus closes the semiconducting gap to 2.58 eV. Also here the conductance maps at the HOMO and LUMO energy agree nicely with density functional theory calculations (Figure 5.3.5), keeping in mind that the main discrepancies relate, as in the case of the dimers, to the deviations from planarity as the molecules adsorb on the Au(111) surface. That is, the highest position of the methyl groups and the concomitant increase in height of the nearest sp^2 carbon atoms cause the DOS lobes on the latter to appear strongest, as well as the appearance of additional unexpectedly strong lobes at the positions of the former (Figure 5.3.5). The calculated wavefunctions of HOMO and LUMO on each of the arms of **s1** look extremely similar to those of **m1** (Figure 5.3.4). However, the conjugation and electronic coupling between the arms becomes evident from the decreased gap, which implies a substantial electron delocalization over the whole structure.

It is interesting to compare the symmetric **s1** molecule with the asymmetric **s2** molecule. Although both are closely related, in the case of **s2** theory predicts the HOMO and HOMO-1 to be quasi-degenerate, and the same applies to the LUMO and LUMO+1. Indeed, their superposition provides a substantially better match to the experimentally measured conductance maps at the energies of the frontier orbitals than if compared to HOMO and LUMO alone (Figure 5.3.5 and Figure 5.3.6). Nevertheless, the experimentally observed gap of **s2** is, within our experimental resolution, equal to that of **s1**.

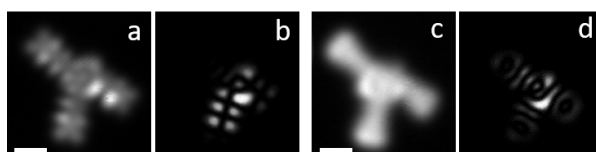


Figure 5.3.6: Constant height dI/dV maps of **s2** as compared to the calculated maps at the exact HOMO and LUMO energies: a) experimentally mapped HOMO, b) simulation at HOMO energy, c) experimentally mapped LUMO and d) simulation at LUMO energy. Scale bar is 6 Å for a and c.

As advanced in the beginning of this section, on Au(110) the situation is completely different. As occurs on Au(111), the initial reactions are dominated by Ullmann coupling. However, the action of the highly anisotropic Au(110) surface as template limits the reaction products to structures composed of collinear reactant molecules, which in turn limits the possible Ullmann coupling products to **d2** and **d3**. Out of these two structures **d3** is much less common. Henceforth we will thus only focus on structures hierarchically built from **d2**. To covalently couple **d2** molecules the methyl groups need first to be activated. This requires higher temperatures than the Ullmann coupling, namely in the order of 525 K. Whereas on Au(111) such temperature treatment results in highly disordered polymers (Figure 5.3.2b), the uniaxial monomer alignment on Au(110) drives a polymerization of **d2** molecules into regular non-benzenoid one-dimensional polymers (Figure 5.3.7).

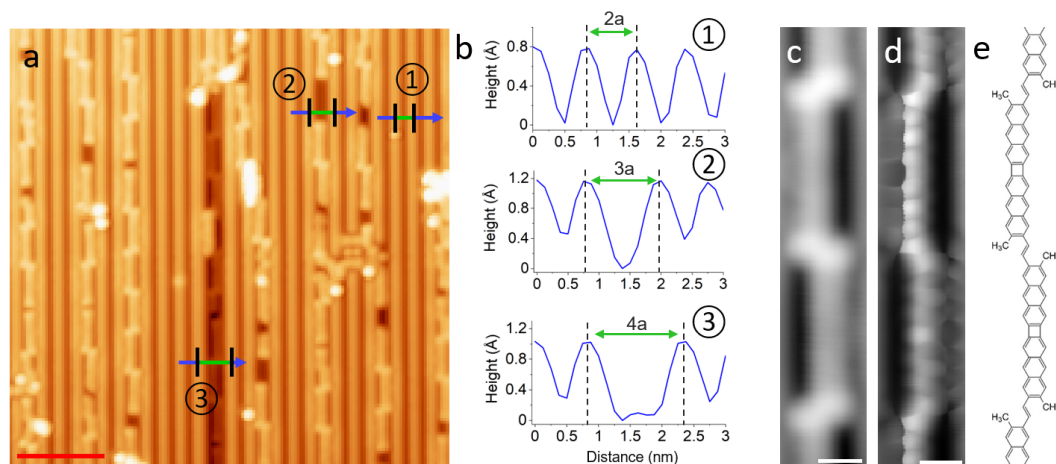


Figure 5.3.7: a) Representative STM overview image of the sample on Au(110) after annealing to 525 K, b) profile lines corresponding to those marked in image a, c-d) STM topography image of the polymer product, d) corresponding constant height image with CO-functionalized tip, e) chemical structure of the product. STM imaging parameters: c) 50 mV/50 pA, d) 5 mV. Scale bar: a) 4 nm, c-d) 5 Å.

As a first observation, it becomes evident that the polymers always adsorb within trenches of the reconstructed substrate surface. As prepared, the Au(110) is characterized by a 2×1 reconstruction in which neighboring rows of Au atoms are separated by twice the Au lattice constant $a = 4.07$ Å.²⁵⁹ Such

reconstruction can be observed in the clean substrate regions of Figure 5.3.7a, and its periodicity is shown in the top profile of Figure 5.3.7b marked with (1). However, although the mere “as deposited” **m1** reactants don’t cause any changes to it (Figure 5.3.1), the surface in vicinity of the polymers changes into a 3×1 (marked with (2) in Figure 5.3.7a-b) or occasionally also a 4×1 (marked with (3) in Figure 5.3.7a-b) reconstruction as the sample is annealed, with the polymers always embedded within the widened trenches. Figure 5.3.7c shows a representative constant current image of the dominant reaction product. Its building unit is clearly recognized as **d2**, but the inter-unit coupling is not trivial to determine even from high-resolution images with CO-functionalized probes in the repulsive interaction regime (Figure 5.3.7d), in part due to the non-planarity of the polymer carbon backbone within the reconstruction trenches.

We have considered five different linking motifs (Figure 5.3.8) and could determine the structure displayed in Figure 5.3.7e as the actual product because it is the only one reproducing the electronic properties of the polymers that are described below. The two lobes of enhanced contrast at either side of the junction in constant current images are thus assigned to the remaining sp^3 methyl groups and their increased height as occurred with the molecular structures on Au(111).

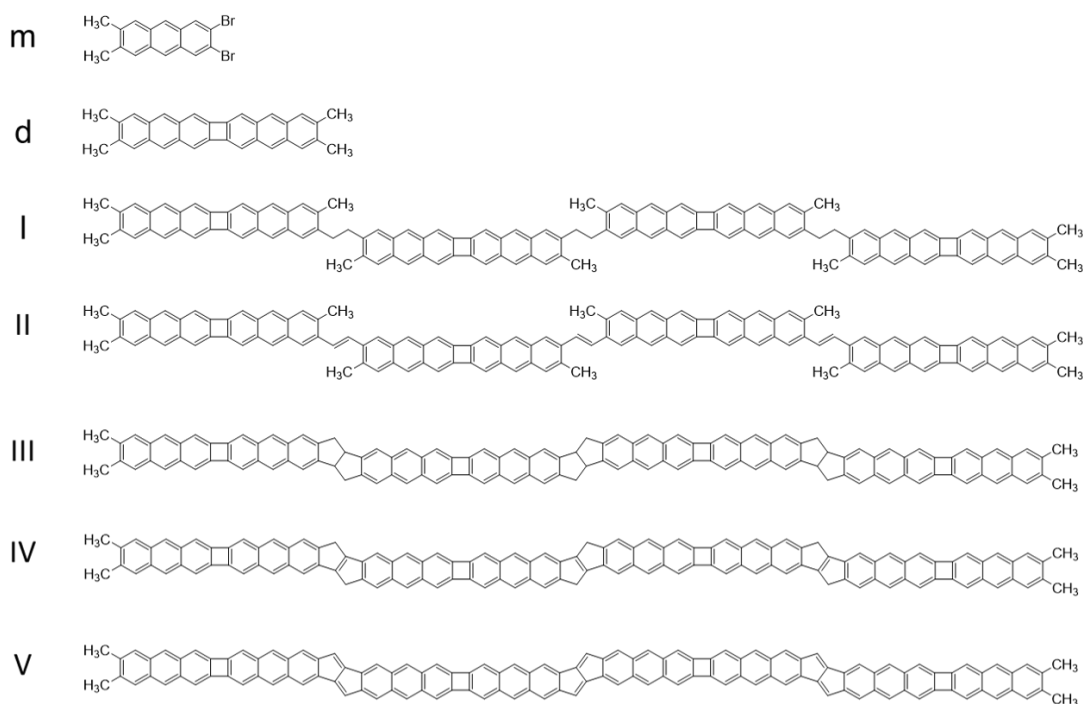


Figure 5.3.8: Chemical structure of the precursor molecule **m**), **d2** dimer **d**), I-V) possible coupling motifs of **d2**.

Figure 5.3.9a displays differential conductance point spectra obtained on an oligomer composed of four **d2** units shown in the inset. The spectra display a pronounced location-dependent signal, as presented with two examples (blue and red curves) obtained at the accordingly colored points in the inset (the pink curve is the reference spectrum on the substrate). In either case the spectra reveal broad resonances both for the occupied and unoccupied states. Conductance maps of occupied and unoccupied states are reminiscent of the HOMO and LUMO of **d2** (Figure 5.3.5), with a series of lobes along the molecular sides for the former and a large dominating signal at the position of the four-membered ring for the latter. The signal is additionally modulated by an asymmetry along the long molecular axis due to the alternating tilt of the different **d2** units, whose side nearest to the Au row delimiting the trench is higher and thus appears with a stronger contrast.

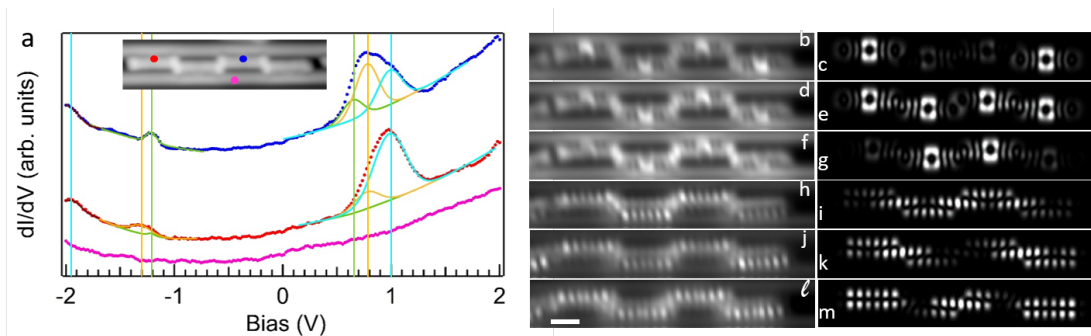


Figure 5.3.9: a) Differential conductance point spectra of a tetramer of **d2** with the positions on the tetramer shown by the color code, magenta represents reference spectrum taken on Au(110) surface. Dotted lines represent experimental data, solid lines are fits explained in the text. Constant height dI/dV maps of the LUMO+2 b-c), LUMO+1 d-e) LUMO f-g), HOMO h-i) HOMO-1 j-k) HOMO-2 l-m). Experiment and theory results are in the left and right columns, respectively. Experimental maps are scanned with a Cl-functionalized tip. STM imaging parameters: b) 0.985 V d) 0.780 V, f) 0.650 V, h) -1.200 V, j) -1.380 V l) -1.920 V. Scale bar is 9 Å and applies to all experimental maps.

Interestingly, conductance maps at different energies within the range of those broad resonances show a markedly different appearance. Focusing on the unoccupied states, as the energy is increased the maps show an increased signal first on the two central 4-membered rings (Figure 5.3.9f), then homogeneously distributed over the four 4-membered rings of the tetramer (Figure 5.3.9d), and finally on the 4-membered rings of the two outer units (Figure 5.3.9b). In contrast, as we move away from the Fermi energy for the occupied states, the signal is first strongest on the two central units (Figure 5.3.9h), then on the outer units (Figure 5.3.9j) and then appears homogeneously distributed over the four units (Figure 5.3.9l).

The same findings, although with increased contrast, are obtained from constant current conductance maps (Figure 5.3.10e). DFT calculations on a free-standing tetramer reveal the DOS of the first three occupied and unoccupied states to have exactly the same distribution (the discrepancies between theory and experiment can all be accounted for by the substrate-driven alternating tilt of the **d2** units in the experiment and the planar structure in the calculations).

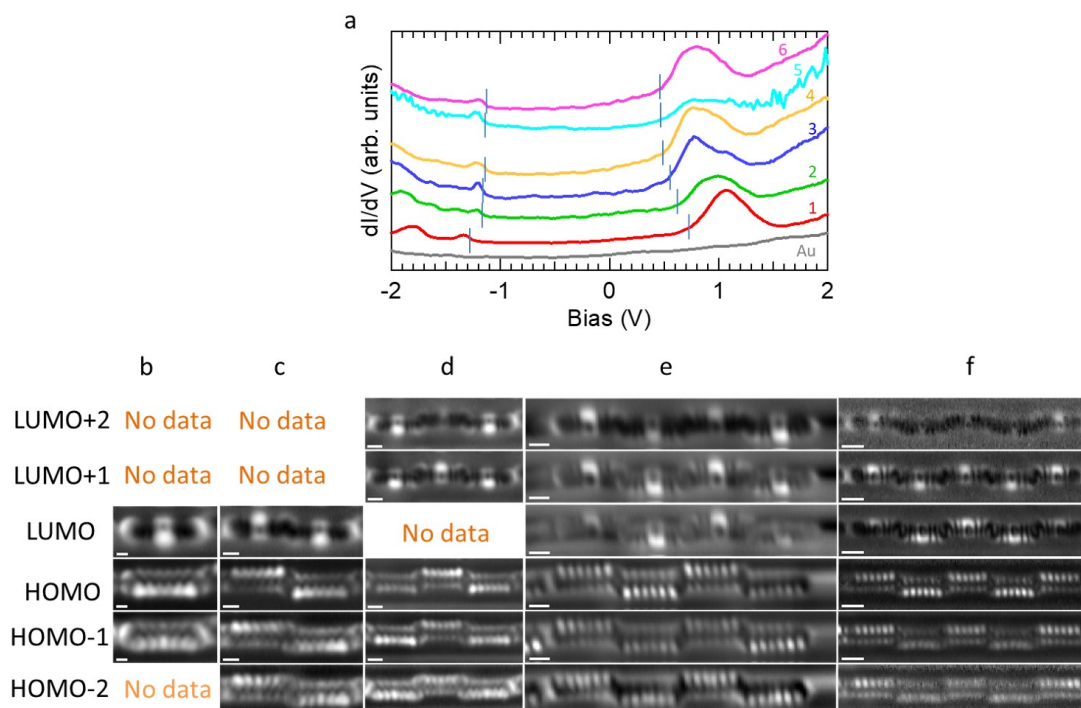


Figure 5.3.10: a) dI/dV point spectra of 1 to 6 conjugated dimer **d2** structures on Au(110), gray is the reference spectrum on the surface, vertical lines on each spectrum represents the onset of the frontier molecular orbitals. HOMO-2 to LUMO+2 constant current dI/dV mapping of b) monomer c) dimer d) trimer e) tetramer f) pentamer of conjugated **d2**. Scale bar b) 3 Å, c) 5 Å, d-e) 6 Å, f) 9 Å. Pentamer in panel f is imaged with a CO-functionalized tip.

We thus conclude that the broad resonances observed in the spectra correspond to a convolution of multiple orbitals. We have deconvoluted the various states fitting the spectra with a back-ground and six Gaussian resonances, displayed with green, orange and sky blue colored lines as their energy departs from the Fermi level for both occupied and unoccupied states (Figure 5.3.9a). The fits of both spectra show the six resonances at the same energies (additionally marked by accordingly colored vertical lines) but a varying intensity that follows the orbital's distribution measured experimentally and confirmed by theory (Fig. 5.3.9b-m).

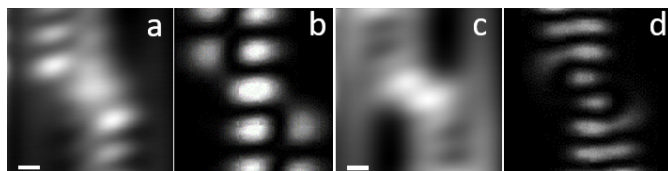


Figure 5.3.11: A close-up constant height dI/dV mapping at the junction between **d2** dimers. a) At the HOMO energy and b) the calculated HOMO map, c) at the LUMO energy and d) the calculated LUMO map. STM imaging parameters: a) -1.200 V, c) 0.650 V. Scale bar is 2 Å for a and c.

This overall nice agreement, along with the excellently matching DOS from experiment and calculations at the inter-unit junctions (Figure 5.3.11), proves our structural assignment for the linking motif. Besides, annealing to even higher temperatures at which additional cyclo-dehydrogenation events can be triggered, rendered different types of junctions that have instead been assigned to some of the other considered coupling motifs (Figure 5.3.8 IV and V) by comparison of their measured and calculated low-energy orbitals (Figure 5.3.12).

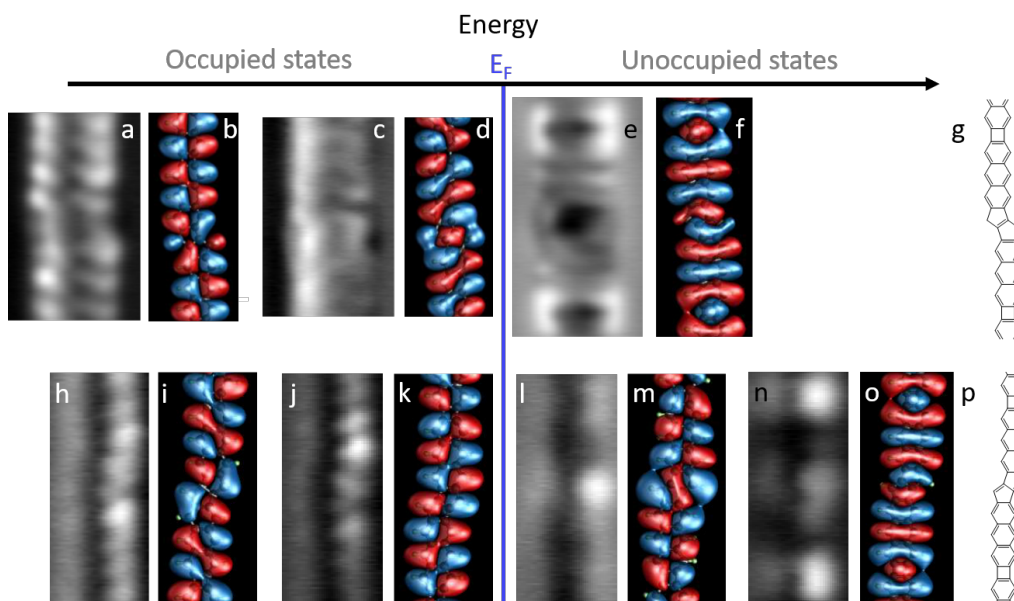


Figure 5.3.12: Constant current dI/dV mapping of the polymers obtained after annealing to 560 K, a-f) showing the HOMO-1 to LUMO maps (in grey scale) with the associated wavefunction calculations for the structure in g), h-o) showing the HOMO-1 to LUMO+1 maps with the associated calculations for the structure in g).

The resulting oligomers being conjugated structures, the HOMO-LUMO gap is expected to scale inversely with the molecular size. We have analyzed that behavior comparing oligomers with lengths from one single **d2** unit to six of them (Figure 5.3.10a). The spectra indeed reveal the onset of the occupied and unoccupied frontier states to approach the Fermi level as the length increases, although with only negligible changes for lengths of four and more units. The conductance maps of the low energy orbitals (Figure 5.3.10b-f) show the same intensity distribution regardless of the oligomer length: the unoccupied orbitals are most intense first on the central units, then all over the structure and thereafter on the outer units, whereas the occupied orbitals are most intense first on the central unit, then on the outer units and then all over the structure.

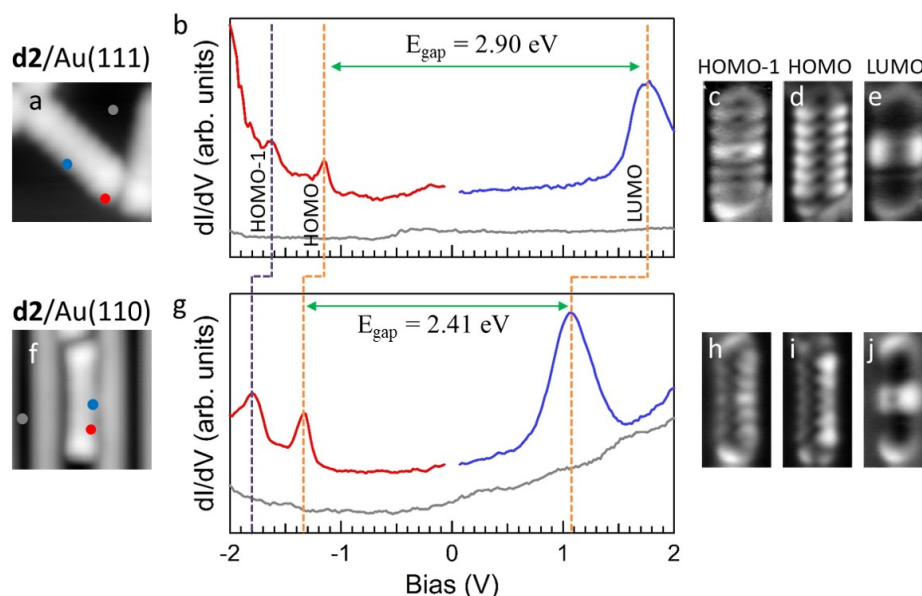


Figure 5.3.13: Comparing the electronic appearance of **d2** on Au(111) and on Au(110), a) STM topography image of **d2** on Au(111), showing the position of the spectra in b, b) differential conductance spectra of **d2** on Au(111), c-e) constant current dI/dV maps of **d2** on Au(111) taken with CO-functionalized tip, f) STM topography image of **d2** on Au(110), g) differential conductance spectra of **d2** on Au(110), h-j) constant current dI/dV maps of **d2** on Au(110). STM imaging parameters: a) -1160 mV/ 50 pA, c) -1630 mV/ 300 pA, d) -1160 mV/ 300 pA, e) 1760 mV/ 300 pA, f) 50 mV/ 50 pA, h) -1800 mV/ 400 pA, i) -1340 mV/ 400 pA, j) 1140 mV/ 400 pA.

It is also interesting to compare the measured electronic properties of adsorbates as a function of the underlying substrate. Within this work, the common product on which to perform such comparison is **d2**, and the associated data are displayed in Figure 5.3.13. On both surfaces, the dI/dV spectra reveal clear resonances for the HOMO-1, HOMO and LUMO orbitals. However, there are substantial differences between the two gold surfaces. Taking the data on Au(111) as reference, we see a substantial downward shift in the energy of all molecular orbitals of molecules adsorbed on Au(110). This effect could in principle be ascribed to the different workfunction of the two gold surfaces, which is lower by about 170 meV for Au(110).²⁶⁰

In an ideal vacuum level pinning scenario, as expected for weakly interacting molecule-substrate interfaces,²²³ this would translate into a rigid downward shift of all molecular orbitals by that amount. However, whereas the HOMO and HOMO-1 indeed shift rigidly by that same amount, the LUMO shifts substantially more, resulting in a reduction of the HOMO-LUMO gap by nearly 0.5 eV. We hypothesize that, although maintaining a weak adsorbate-substrate electronic coupling and thus showing no obvious changes in the conductance maps of the orbitals, the larger shift of the LUMO may result from a slightly increased hybridization of the unoccupied molecular orbitals with the undercoordinated (and thus more reactive) Au atoms that form the rows of the Au(110) reconstruction and cause the molecule's tilting.

5.3.3 Conclusion

In conclusion, we have analyzed the reactivity of acene-based precursor molecules functionalized with halogen atoms and methyl groups on two substrates of different symmetry. Whereas on the two-dimensional Au(111) surface the molecules show a marked preference for the formation of "two-dimensional" starphene molecules, on Au(110) the one-dimensional trenches of its reconstruction act as template and limit the product structures to those conformed by collinearly fused precursors, which end up polymerizing into one-dimensional non-benzenoid conjugated polymers.

We further provide a detailed characterization of the interesting electronic properties of each of the observed products, as well as a comparison of those properties for the same molecule on either substrate. This work thus constitutes a substantial advance in the controlled synthesis and the characterization of to date only scarcely investigated organic products of great scientific interest, as applies both to starphenes and to non-benzenoid conjugated polymers.

Appendix A

List of publications

A.1 Derived from this thesis

1. Luciano Colazzo, Mohammed S. G. Mohammed, Ruth Dorel, Pawel Nita, Carlos García Fernández, Paula Abufager, Nicolás Lorente, Antonio Echavarren and Dimas G. de Oteyza; "On-surface synthesis of heptacene on Ag(001) from brominated and non-brominated tetrahydroheptacene precursors;" (Chemical Communications, 2018, <https://doi.org/10.1039/C8CC04402C>)
2. Luciano Colazzo, Mohammed S. G. Mohammed, Aurelio Gallardo, Zakaria M. Abd El-Fattah, José A. Pomposo, Pavel Jelinek and Dimas G. de Oteyza; "Controlling the stereospecific bonding motif of Au–thiolate links;" (Nanoscale, 2019, <https://doi.org/10.1039/C9NR04383G>)
3. Mohammed S. G. Mohammed, Luciano Colazzo, Aurelio Gallardo, José A. Pomposo, Pavel Jelínek and Dimas G. de Oteyza; "Steering alkyne homocoupling with on-surface synthesized metal-organic complexes;" (Chemical Communications, 2020, <https://doi.org/10.1039/D0CC03779F>)
4. Mohammed S. G. Mohammed, Luciano Colazzo, Roberto Robles, Ruth Dorel, Antonio M. Echavarren, Nicolás Lorente and Dimas G. de Oteyza; "Electronic decoupling of polyacenes from the underlying metal substrate by sp^3 carbon atoms;" (Communications Physics, 2020, <https://doi.org/10.1038/s42005-020-00425-y>)
5. James Lawrence, Mohammed S. G. Mohammed, Alejandro Berdonces-Layunta, Dulce Rey, Diego Peña, and Dimas G. de Oteyza; "Reassessing alkyne coupling reactions while studying the electronic properties of diverse pyrene linkages at surfaces;" (submitted)
6. Mohammed S. G. Mohammed, James Lawrence, Fátima García, Pedro Brandimarte, Alejandro Berdonces-Layunta, Dolores Pérez, Daniel Sánchez-Portal, Diego Peña, and Dimas G. de Oteyza; "From starphenes to non-benzenoid linear conjugated polymers by substrate templating;" (in preparation)

A.2 Other publications

1. Ignacio Piquero-Zulaica, Aran Garcia-Lekue, Luciano Colazzo, Claudio K. Krug, Mohammed S. G. Mohammed, Zakaria M. Abd El-Fattah, J. Michael Gottfried, Dimas G. de Oteyza, J. Enrique Ortega and Jorge Lobo-Checa; "Electronic structure tunability by periodic meta-ligand spacing in one-dimensional organic semiconductors;" (ACS Nano, 2018, <https://doi.org/10.1021/acsnano.8b06536>)
2. Néstor Merino-Díez, Alejandro Pérez Paz, Jingcheng Li, Manuel Vilas-Varela, James Lawrence, Mohammed S. G. Mohammed, Alejandro Berdonces-Layunta, Ana Barragán, Jose Ignacio Pascual, Jorge Lobo-Checa, Diego Peña and Dimas G. de Oteyza; "Hierarchy in the halogen activation during surface-promoted Ullmann coupling;" (ChemPhysChem 2019, <https://doi.org/10.1002/cphc.201900633>)
3. Roberto Costantini, Luciano Colazzo, Laura Batini, Matus Stredansky, Mohammed S. G. Mohammed, Simona Achilli, Luca Floreano, Guido Fratesi, Dimas G. de Oteyza and Albano Cossaro; "Keto-enol tautomerization drives the self-assembly of leucoquinizarin on Au(111);" (Chemical Communications, 2020, <https://doi.org/10.1039/C9CC09915H>)
4. James Lawrence, Pedro Brandimarte, Alejandro Berdonces-Layunta, Mohammed S. G. Mohammed, Abhishek Grewal, Christopher C. Leon, Daniel Sánchez-Portal and Dimas G. de Oteyza; "Probing

- the magnetism of topological end-states in 5-armchair graphene nanoribbons;" (ACS Nano, 2020, <https://doi.org/10.1021/acsnano.9b10191>)
5. Néstor Merino-Díez, Mohammed S. G. Mohammed, Jesús Castro-Esteban, Luciano Colazzo, Alejandro Berdonces-Layunta, James Lawrence, J. Ignacio Pascual, Dimas G. de Oteyza and Diego Peña; "Transferring axial molecular chirality through a sequence of on-surface reactions;" (Chemical Science, 2020, <https://doi.org/10.1039/D0SC01653E>)
 6. Tao Wang, Yu Pan, Wenzhao Zhang, James Lawrence, Mohammed S. G. Mohammed, Jianmin Huang, Lin Feng, Alejandro Berdonces-Layunta, Dong Han, Qian Xu, Xiaojun Wu, Steven L. Tait, Dimas G. de Oteyza and Junfa Zhu; "On-surface synthesis of five-membered carbon ring from a terminal alkynyl bromide: a [4+1] annulation;" (Journal of Physical Chemistry Letters, 2020, <https://doi.org/10.1021/acs.jpcllett.0c01483>)
 7. Alejandro Berdonces-Layunta, James Lawrence, Shayan Edalatmanesh, Jesús Castro-Esteban, Tao Wang, Mohammed S. G. Mohammed, Luciano Colazzo, Diego Peña, Pavel Jelinek, and Dimas de Oteyza; "The chemical stability of graphene nanoribbon zigzag edges;" (submitted)

Bibliography

- [1] K. S. Novoselov, A. K. Geim, S. V. Morozov, D. Jiang, Y. Zhang, S. V. Dubonos, I. V. Grigorieva, and A. A. Firsov, "Electric field effect in atomically thin carbon films," *science*, vol. 306, no. 5696, pp. 666–669, 2004.
- [2] S. Morozov, K. Novoselov, M. Katsnelson, F. Schedin, D. Elias, J. A. Jaszczak, and A. Geim, "Giant intrinsic carrier mobilities in graphene and its bilayer," *Physical review letters*, vol. 100, no. 1, p. 016602, 2008.
- [3] Y. Hernandez, V. Nicolosi, M. Lotya, F. M. Blighe, Z. Sun, S. De, I. McGovern, B. Holland, M. Byrne, Y. K. Gun'Ko, *et al.*, "High-yield production of graphene by liquid-phase exfoliation of graphite," *Nature nanotechnology*, vol. 3, no. 9, pp. 563–568, 2008.
- [4] X.-Y. Wang, A. Narita, and K. Müllen, "Precision synthesis versus bulk-scale fabrication of graphenes," *Nature Reviews Chemistry*, vol. 2, no. 1, pp. 1–10, 2017.
- [5] L. A. Ponomarenko, F. Schedin, M. I. Katsnelson, R. Yang, E. W. Hill, K. S. Novoselov, and A. K. Geim, "Chaotic dirac billiard in graphene quantum dots," *Science*, vol. 320, no. 5874, pp. 356–358, 2008.
- [6] J. Cai, P. Ruffieux, R. Jaafar, M. Bieri, T. Braun, S. Blankenburg, M. Muoth, A. P. Seitsonen, M. Saleh, X. Feng, *et al.*, "Atomically precise bottom-up fabrication of graphene nanoribbons," *Nature*, vol. 466, no. 7305, pp. 470–473, 2010.
- [7] D. G. de Oteyza, A. García-Lekue, M. Vilas-Varela, N. Merino-Díez, E. Carbonell-Sanroma, M. Corso, G. Vasseur, C. Rogero, E. Guitian, J. I. Pascual, *et al.*, "Substrate-independent growth of atomically precise chiral graphene nanoribbons," *ACS nano*, vol. 10, no. 9, pp. 9000–9008, 2016.
- [8] A. Kimouche, M. M. Ervasti, R. Drost, S. Halonen, A. Harju, P. M. Joensuu, J. Sainio, and P. Liljeroth, "Ultra-narrow metallic armchair graphene nanoribbons," *Nature communications*, vol. 6, p. 10177, 2015.
- [9] P. Ruffieux, S. Wang, B. Yang, C. Sánchez-Sánchez, J. Liu, T. Dienel, L. Talirz, P. Shinde, C. A. Pignedoli, D. Passerone, *et al.*, "On-surface synthesis of graphene nanoribbons with zigzag edge topology," *Nature*, vol. 531, no. 7595, pp. 489–492, 2016.
- [10] J. Lawrence, P. Brandimarte, A. Berdonces-Layunta, M. S. Mohammed, A. Grewal, C. C. Leon, D. Sanchez-Portal, and D. G. de Oteyza, "Probing the magnetism of topological end states in 5-armchair graphene nanoribbons," *ACS nano*, vol. 14, no. 4, pp. 4499–4508, 2020.
- [11] L. Talirz, H. Sode, T. Dumslaff, S. Wang, J. R. Sanchez-Valencia, J. Liu, P. Shinde, C. A. Pignedoli, L. Liang, V. Meunier, *et al.*, "On-surface synthesis and characterization of 9-atom wide armchair graphene nanoribbons," *ACS nano*, vol. 11, no. 2, pp. 1380–1388, 2017.
- [12] F. Eisenhut, T. Kuhne, F. García, S. Fernández, E. Guitián, D. Pérez, G. Trinquier, G. Cuniberti, C. Joachim, D. Peña, *et al.*, "Dodecacene generated on surface: Reopening of the energy gap," *ACS nano*, vol. 14, no. 1, pp. 1011–1017, 2019.
- [13] S. Thussing, S. Flade, K. Eimre, C. A. Pignedoli, R. Fasel, and P. Jakob, "Reaction Pathway toward Seven-Atom-Wide Armchair Graphene Nanoribbon Formation and Identification of Intermediate Species on Au(111)," *The Journal of Physical Chemistry C*, vol. 124, no. 29, pp. 16009–16018, 2020.
_eprint: <https://doi.org/10.1021/acs.jpcc.0c04596>.
- [14] J. Van Der Lit, M. P. Boneschanscher, D. Vanmaekelbergh, M. Ijäs, A. Uppstu, M. Ervasti, A. Harju, P. Liljeroth, and I. Swart, "Suppression of electron–vibron coupling in graphene nanoribbons contacted via a single atom," *Nature communications*, vol. 4, no. 1, pp. 1–6, 2013.
- [15] N. Merino-Díez, M. S. Mohammed, J. Castro-Esteban, L. Colazzo, A. Berdonces-Layunta, J. Lawrence, J. I. Pascual, D. G. de Oteyza, and D. Peña, "Transferring axial molecular chirality through a sequence of on-surface reactions," *Chemical Science*, 2020.
- [16] G. Otero, G. Biddau, C. Sánchez-Sánchez, R. Caillard, M. F. López, C. Rogero, F. J. Palomares, N. Cabello, M. A. Basanta, J. Ortega, *et al.*, "Fullerenes from aromatic precursors by surface-catalysed cyclodehydrogenation," *Nature*, vol. 454, no. 7206, pp. 865–868, 2008.

- [17] Z. Cai, M. Liu, L. She, X. Li, J. Lee, D.-X. Yao, H. Zhang, L. Chi, H. Fuchs, and D. Zhong, "Linear alkane c c bond chemistry mediated by metal surfaces," *ChemPhysChem*, vol. 16, no. 7, pp. 1356–1360, 2015.
- [18] A. L. Pinardi, G. Otero-Irurueta, I. Palacio, J. I. Martinez, C. Sanchez-Sanchez, M. Tello, C. Rogero, A. Cossaro, A. Preobrajenski, B. Gómez-Lor, *et al.*, "Tailored formation of n-doped nanoarchitectures by diffusion-controlled on-surface (cyclo) dehydrogenation of heteroaromatics," *ACS nano*, vol. 7, no. 4, pp. 3676–3684, 2013.
- [19] J. R. Sanchez-Valencia, T. Dienel, O. Gröning, I. Shorubalko, A. Mueller, M. Jansen, K. Amsharov, P. Ruffieux, and R. Fasel, "Controlled synthesis of single-chirality carbon nanotubes," *Nature*, vol. 512, no. 7512, pp. 61–64, 2014.
- [20] G. Otero-Irurueta, J. Martínez, R. Bueno, F. Palomares, H. Salavagione, M. Singh, J. Méndez, G. Ellis, M. López, and J. Martín-Gago, "Adsorption and coupling of 4-aminophenol on pt (111) surfaces," *Surface science*, vol. 646, pp. 5–12, 2016.
- [21] E. Lewis, M. Marcinkowski, C. Murphy, M. Liriano, A. Therrien, A. Pronschinske, and E. Sykes, "Controlling selectivity in the ullmann reaction on cu (111)," *Chemical Communications*, vol. 53, no. 55, pp. 7816–7819, 2017.
- [22] L. E. Dinca, J. M. MacLeod, J. Lipton-Duffin, C. Fu, D. Ma, D. F. Perepichka, and F. Rosei, "Tailoring the reaction path in the on-surface chemistry of thienoacenes," *The Journal of Physical Chemistry C*, vol. 119, no. 39, pp. 22432–22438, 2015.
- [23] C.-X. Wang, Q. Jin, C.-H. Shu, X. Hua, Y.-T. Long, and P.-N. Liu, "Dehydrogenative homocoupling of tetrafluorobenzene on pd (111) via para-selective c-h activation," *Chemical Communications*, vol. 53, no. 47, pp. 6347–6350, 2017.
- [24] C. R. Larrea and C. J. Baddeley, "Fabrication of a high-quality, porous, surface-confined covalent organic framework on a reactive metal surface," *ChemPhysChem*, vol. 17, no. 7, pp. 971–975, 2016.
- [25] C. Guo, Y. Wang, M. Kittelmann, L. Kantorovitch, A. Kuhnle, and A. Floris, "Mechanisms of covalent dimerization on a bulk insulating surface," *The Journal of Physical Chemistry C*, vol. 121, no. 18, pp. 10053–10062, 2017.
- [26] F. Para, F. Bocquet, L. Nony, C. Loppacher, M. Féron, F. Cherioux, D. Z. Gao, F. F. Canova, and M. B. Watkins, "Micrometre-long covalent organic fibres by photoinitiated chain-growth radical polymerization on an alkali-halide surface," *Nature Chemistry*, vol. 10, no. 11, pp. 1112–1117, 2018.
- [27] A. Richter, M. Vilas-Varela, D. Peña, R. Bechstein, and A. Kühnle, "Homocoupling of terminal alkynes on calcite (10.4)," *Surface Science*, vol. 678, pp. 106–111, 2018.
- [28] J. Eichhorn, D. Nieckarz, O. Ochs, D. Samanta, M. Schmittel, P. J. Szabelski, and M. Lackinger, "On-surface ullmann coupling: the influence of kinetic reaction parameters on the morphology and quality of covalent networks," *ACS nano*, vol. 8, no. 8, pp. 7880–7889, 2014.
- [29] A. Riss, A. P. Paz, S. Wickenburg, H.-Z. Tsai, D. G. De Oteyza, A. J. Bradley, M. M. Ugeda, P. Gorman, H. S. Jung, M. F. Crommie, *et al.*, "Imaging single-molecule reaction intermediates stabilized by surface dissipation and entropy," *Nature chemistry*, vol. 8, no. 7, pp. 678–683, 2016.
- [30] L. Dong, P. N. Liu, and N. Lin, "Surface-activated coupling reactions confined on a surface," *Accounts of chemical research*, vol. 48, no. 10, pp. 2765–2774, 2015.
- [31] L. Dong, S. Wang, W. Wang, C. Chen, T. Lin, J. Adisojoso, and N. Lin, "Transition metals trigger on-surface ullmann coupling reaction: intermediate, catalyst and template," in *On-Surface Synthesis*, pp. 23–42, Springer, 2016.
- [32] J. Bjork, F. Hanke, and S. Stafstrom, "Mechanisms of halogen-based covalent self-assembly on metal surfaces," *Journal of the American Chemical Society*, vol. 135, no. 15, pp. 5768–5775, 2013.
- [33] N. Merino-Díez, J. Lobo-Checa, P. Nita, A. Garcia-Lekue, A. Basagni, G. Vasseur, F. Tiso, F. Sedona, P. K. Das, J. Fujii, *et al.*, "Switching from reactant to substrate engineering in the selective synthesis of graphene nanoribbons," *The journal of physical chemistry letters*, vol. 9, no. 10, pp. 2510–2517, 2018.
- [34] D. G. de Oteyza, P. Gorman, Y.-C. Chen, S. Wickenburg, A. Riss, D. J. Mowbray, G. Etkin, Z. Pedramrazi, H.-Z. Tsai, A. Rubio, *et al.*, "Direct imaging of covalent bond structure in single-molecule chemical reactions," *Science*, vol. 340, no. 6139, pp. 1434–1437, 2013.
- [35] F. Mohn, B. Schuler, L. Gross, and G. Meyer, "Different tips for high-resolution atomic force microscopy and scanning tunneling microscopy of single molecules," *Applied Physics Letters*, vol. 102, no. 7, p. 073109, 2013.
- [36] B. Schuler, S.-X. Liu, Y. Geng, S. Decurtins, G. Meyer, and L. Gross, "Contrast formation in kelvin probe force microscopy of single π -conjugated molecules," *Nano letters*, vol. 14, no. 6, pp. 3342–3346, 2014.

- [37] S.-W. Hla, L. Bartels, G. Meyer, and K.-H. Rieder, "Inducing all steps of a chemical reaction with the scanning tunneling microscope tip: towards single molecule engineering," *Physical Review Letters*, vol. 85, no. 13, p. 2777, 2000.
- [38] R. Zuzak, R. Dorel, M. Krawiec, B. Such, M. Kolmer, M. Szymonski, A. M. Echavarren, and S. Godlewski, "Nonacene generated by on-surface dehydrogenation," *ACS nano*, vol. 11, no. 9, pp. 9321–9329, 2017.
- [39] L. Colazzo, M. S. Mohammed, R. Dorel, P. Nita, C. G. Fernández, P. Abufager, N. Lorente, A. M. Echavarren, and D. G. De Oteyza, "On-surface synthesis of heptacene on ag (001) from brominated and non-brominated tetrahydroheptacene precursors," *Chemical Communications*, vol. 54, no. 73, pp. 10260–10263, 2018.
- [40] I. Swart, T. Sonleitner, J. Niedenfuhr, and J. Repp, "Controlled lateral manipulation of molecules on insulating films by stm," *Nano letters*, vol. 12, no. 2, pp. 1070–1074, 2012.
- [41] S. Wang, L. Talirz, C. A. Pignedoli, X. Feng, K. Müllen, R. Fasel, and P. Ruffieux, "Giant edge state splitting at atomically precise graphene zigzag edges," *Nature communications*, vol. 7, no. 1, pp. 1–6, 2016.
- [42] M. S. Mohammed, L. Colazzo, A. Gallardo, J. A. Pomposo, P. Jelínek, and D. G. de Oteyza, "Steering alkyne homocoupling with on-surface synthesized metal–organic complexes," *Chemical Communications*, 2020.
- [43] J. A. Lipton-Duffin, O. Ivasenko, D. Perepichka, and F. Rosei, "Synthesis of polyphenylene molecular wires by surface-confined polymerization," *small*, vol. 5, no. 5, pp. 592–597, 2009.
- [44] M. Bieri, M.-T. Nguyen, O. Groning, J. Cai, M. Treier, K. Ait-Mansour, P. Ruffieux, C. A. Pignedoli, D. Passerone, M. Kastler, *et al.*, "Two-dimensional polymer formation on surfaces: insight into the roles of precursor mobility and reactivity," *Journal of the American Chemical Society*, vol. 132, no. 46, pp. 16669–16676, 2010.
- [45] M. Di Giovannantonio, J. I. Urgel, U. Beser, A. V. Yakutovich, J. Wilhelm, C. A. Pignedoli, P. Ruffieux, A. Narita, K. Mullen, and R. Fasel, "On-surface synthesis of indenofluorene polymers by oxidative five-membered ring formation," *Journal of the American Chemical Society*, vol. 140, no. 10, pp. 3532–3536, 2018.
- [46] N. Merino-Díez, A. Pérez Paz, J. Li, M. Vilas-Varela, J. Lawrence, M. S. Mohammed, A. Berdonces-Layunta, A. Barragán, J. I. Pascual, J. Lobo-Checa, *et al.*, "Hierarchy in the halogen activation during surface-promoted ullmann coupling," *ChemPhysChem*, vol. 20, no. 18, pp. 2305–2310, 2019.
- [47] A. Basagni, F. Sedona, C. A. Pignedoli, M. Cattelan, L. Nicolas, M. Casarin, and M. Sambri, "Molecules–oligomers–nanowires–graphene nanoribbons: a bottom-up stepwise on-surface covalent synthesis preserving long-range order," *Journal of the American Chemical Society*, vol. 137, no. 5, pp. 1802–1808, 2015.
- [48] G. Borin Barin, A. Fairbrother, L. Rotach, M. Bayle, M. Paillet, L. Liang, V. Meunier, R. Hauert, T. Dumsclaff, A. Narita, *et al.*, "Surface-synthesized graphene nanoribbons for room temperature switching devices: substrate transfer and ex situ characterization," *ACS applied nano materials*, vol. 2, no. 4, pp. 2184–2192, 2019.
- [49] A. Basagni, G. Vasseur, C. A. Pignedoli, M. Vilas-Varela, D. Pena, L. Nicolas, L. Vitali, J. Lobo-Checa, D. G. de Oteyza, F. Sedona, *et al.*, "Tunable band alignment with unperturbed carrier mobility of on-surface synthesized organic semiconducting wires," *Acs Nano*, vol. 10, no. 2, pp. 2644–2651, 2016.
- [50] G. Binnig, H. Rohrer, C. Gerber, and E. Weibel, "Surface studies by scanning tunneling microscopy," *Physical review letters*, vol. 49, no. 1, p. 57, 1982.
- [51] C. Herbschleb, P. Van Der Tuijn, S. Roobol, V. Navarro, J. Bakker, Q. Liu, D. Stoltz, M. Cañas-Ventura, G. Verdoes, M. Van Spronsen, *et al.*, "The reactorstm: Atomically resolved scanning tunneling microscopy under high-pressure, high-temperature catalytic reaction conditions," *Review of Scientific Instruments*, vol. 85, no. 8, p. 083703, 2014.
- [52] J. Tersoff and D. Hamann, "Theory and application for the scanning tunneling microscope," *Physical review letters*, vol. 50, no. 25, p. 1998, 1983.
- [53] J. Bardeen, "Tunnelling from a many-particle point of view," *Physical Review Letters*, vol. 6, no. 2, p. 57, 1961.
- [54] N. Lang, "Spectroscopy of single atoms in the scanning tunneling microscope," *Physical Review B*, vol. 34, no. 8, p. 5947, 1986.
- [55] A. Selloni, P. Carnevali, E. Tosatti, and C. Chen, "Voltage-dependent scanning-tunneling microscopy of a crystal surface: Graphite," in *Scanning Tunneling Microscopy*, pp. 168–171, Springer, 1985.
- [56] N. Noei, A. Weismann, and R. Berndt, "Apparent tunneling barrier height and local work function of atomic arrays," *Beilstein journal of nanotechnology*, vol. 9, no. 1, pp. 3048–3052, 2018.

- [57] M. S. G. Mohammed, L. Colazzo, R. Robles, R. Dorel, A. M. Echavarren, N. Lorente, and D. G. de Oteyza, "Electronic decoupling of polyacenes from the underlying metal substrate by sp³ carbon atoms," *Communications Physics*, vol. 3, Sep 2020.
- [58] L. Gross, F. Mohn, N. Moll, P. Liljeroth, and G. Meyer, "The chemical structure of a molecule resolved by atomic force microscopy," *Science*, vol. 325, no. 5944, pp. 1110–1114, 2009.
- [59] T. Chutora, B. de la Torre, P. Mutombo, J. Hellerstedt, J. Kopeček, P. Jelínek, and M. Švec, "Nitrous oxide as an effective afm tip functionalization: a comparative study," *Beilstein journal of nanotechnology*, vol. 10, no. 1, pp. 315–321, 2019.
- [60] H. Mönig, D. R. Hermoso, O. Díaz Arado, M. Todorović, A. Timmer, S. Schüer, G. Langewisch, R. Pérez, and H. Fuchs, "Submolecular Imaging by Noncontact Atomic Force Microscopy with an Oxygen Atom Rigidly Connected to a Metallic Probe," *ACS Nano*, vol. 10, no. 1, pp. 1201–1209, 2016.
- [61] D. Yesilpinar, B. S. Lammers, A. Timmer, S. Amirjalayer, H. Fuchs, and H. Mönig, "High resolution noncontact atomic force microscopy imaging with oxygen-terminated copper tips at 78 k," *Nanoscale*, vol. 12, no. 5, pp. 2961–2965, 2020.
- [62] K. Iwata, S. Yamazaki, P. Mutombo, P. Hapala, M. Ondráček, P. Jelínek, and Y. Sugimoto, "Chemical structure imaging of a single molecule by atomic force microscopy at room temperature," *Nature communications*, vol. 6, no. 1, pp. 1–7, 2015.
- [63] C. Chiutu, A. Sweetman, A. Lakin, A. Stannard, S. Jarvis, L. Kantorovich, J. Dunn, and P. Moriarty, "Precise orientation of a single c60 molecule on the tip of a scanning probe microscope," *Physical review letters*, vol. 108, no. 26, p. 268302, 2012.
- [64] N. Hauptmann, F. Mohn, L. Gross, G. Meyer, T. Frederiksen, and R. Berndt, "Force and conductance during contact formation to a c60 molecule," *New Journal of Physics*, vol. 14, no. 7, p. 073032, 2012.
- [65] A. Sweetman, S. P. Jarvis, H. Sang, I. Lekkas, P. Rahe, Y. Wang, J. Wang, N. R. Champness, L. Kantorovich, and P. Moriarty, "Mapping the force field of a hydrogen-bonded assembly," *Nature communications*, vol. 5, no. 1, pp. 1–7, 2014.
- [66] R. Temirov, S. Soubatch, O. Neucheva, A. Lassise, and F. Tautz, "A novel method achieving ultra-high geometrical resolution in scanning tunnelling microscopy," *New Journal of Physics*, vol. 10, no. 5, p. 053012, 2008.
- [67] G. Kichin, C. Weiss, C. Wagner, F. S. Tautz, and R. Temirov, "Single molecule and single atom sensors for atomic resolution imaging of chemically complex surfaces," *Journal of the American Chemical Society*, vol. 133, no. 42, pp. 16847–16851, 2011.
- [68] P. Hapala, G. Kichin, C. Wagner, F. S. Tautz, R. Temirov, and P. Jelínek, "Mechanism of high-resolution stm/afm imaging with functionalized tips," *Physical Review B*, vol. 90, no. 8, p. 085421, 2014.
- [69] P. Hapala, R. Temirov, F. S. Tautz, and P. Jelínek, "Origin of high-resolution iets-stm images of organic molecules with functionalized tips," *Physical review letters*, vol. 113, no. 22, p. 226101, 2014.
- [70] O. Krejčí, P. Hapala, M. Ondráček, and P. Jelínek, "Principles and simulations of high-resolution stm imaging with a flexible tip apex," *Physical Review B*, vol. 95, no. 4, p. 045407, 2017.
- [71] J. Tersoff and D. R. Hamann, "Theory of the scanning tunneling microscope," *Physical Review B*, vol. 31, no. 2, p. 805, 1985.
- [72] C. J. Chen, *Introduction to scanning tunneling microscopy*, vol. 4. Oxford University Press on Demand, 1993.
- [73] C. J. Chen, "Theory of scanning tunneling spectroscopy," *Journal of Vacuum Science & Technology A: Vacuum, Surfaces, and Films*, vol. 6, no. 2, pp. 319–322, 1988.
- [74] C. J. Chen, "Tunneling matrix elements in three-dimensional space: The derivative rule and the sum rule," *Physical Review B*, vol. 42, no. 14, p. 8841, 1990.
- [75] L. Gross, N. Moll, F. Mohn, A. Curioni, G. Meyer, F. Hanke, and M. Persson, "High-resolution molecular orbital imaging using a p-wave stm tip," *Physical Review Letters*, vol. 107, no. 8, p. 086101, 2011.
- [76] Z. Li, K. Schouteden, V. Iancu, E. Janssens, P. Lievens, C. Van Haesendonck, and J. I. Cerdá, "Chemically modified stm tips for atomic-resolution imaging of ultrathin nacl films," *Nano Research*, vol. 8, no. 7, pp. 2223–2230, 2015.
- [77] F. Olsson, N. Lorente, and M. Persson, "Stm images of molecularly and atomically chemisorbed oxygen on silver," *Surface science*, vol. 522, no. 1-3, pp. L27–L35, 2003.
- [78] S. Mishra, D. Beyer, R. Berger, J. Liu, O. Groning, J. I. Urgel, K. Mullen, P. Ruffieux, X. Feng, and R. Fasel, "Topological defect-induced magnetism in a nanographene," *Journal of the American Chemical Society*, vol. 142, no. 3, pp. 1147–1152, 2020.

- [79] Y.-h. Zhang, S. Kahle, T. Herden, C. Stroh, M. Mayor, U. Schlickum, M. Ternes, P. Wahl, and K. Kern, "Temperature and magnetic field dependence of a kondo system in the weak coupling regime," *Nature communications*, vol. 4, no. 1, pp. 1–6, 2013.
- [80] J. Girovsky, J. Nowakowski, M. E. Ali, M. Baljovic, H. R. Rossmann, T. Nijs, E. A. Aeby, S. Nowakowska, D. Siewert, G. Srivastava, *et al.*, "Long-range ferrimagnetic order in a two-dimensional supramolecular kondo lattice," *Nature communications*, vol. 8, no. 1, pp. 1–8, 2017.
- [81] M. Ternes, A. J. Heinrich, and W.-D. Schneider, "Spectroscopic manifestations of the kondo effect on single adatoms," *Journal of Physics: Condensed Matter*, vol. 21, no. 5, p. 053001, 2008.
- [82] R. G. Nuzzo and D. L. Allara, "Adsorption of bifunctional organic disulfides on gold surfaces," *Journal of the American Chemical Society*, vol. 105, no. 13, pp. 4481–4483, 1983.
- [83] R. G. Nuzzo, B. R. Zegarski, and L. H. Dubois, "Fundamental studies of the chemisorption of organosulfur compounds on gold (111). implications for molecular self-assembly on gold surfaces," *Journal of the American Chemical Society*, vol. 109, no. 3, pp. 733–740, 1987.
- [84] M. W. Beulen, B.-H. Huisman, P. A. van der Heijden, F. C. van Veggel, M. G. Simons, E. M. Biemond, P. J. de Lange, and D. N. Reinhoudt, "Evidence for nondestructive adsorption of dialkyl sulfides on gold," *Langmuir*, vol. 12, no. 26, pp. 6170–6172, 1996.
- [85] Z. Yang, I. Engquist, J.-M. Kauffmann, and B. Liedberg, "Thiocholesterol on gold: A nanoporous molecular assembly," *Langmuir*, vol. 12, no. 7, pp. 1704–1707, 1996.
- [86] A. Dakkouri, D. Kolb, R. Edelstein-Shima, and D. Mandler, "Scanning tunneling microscopy study of l-cysteine on au (111)," *Langmuir*, vol. 12, no. 11, pp. 2849–2852, 1996.
- [87] G. E. Poirier, "Characterization of organosulfur molecular monolayers on au (111) using scanning tunneling microscopy," *Chemical reviews*, vol. 97, no. 4, pp. 1117–1128, 1997.
- [88] R. W. Carpick and M. Salmeron, "Scratching the surface: fundamental investigations of tribology with atomic force microscopy," *Chemical reviews*, vol. 97, no. 4, pp. 1163–1194, 1997.
- [89] M. Azubel and R. D. Kornberg, "Synthesis of water-soluble, thiolate-protected gold nanoparticles uniform in size," *Nano letters*, vol. 16, no. 5, pp. 3348–3351, 2016.
- [90] F. Ghorbani, N. Attaran-Kakhki, and A. Sazgarnia, "The synergistic effect of photodynamic therapy and photothermal therapy in the presence of gold-gold sulfide nanoshells conjugated indocyanine green on hela cells," *Photodiagnosis and photodynamic therapy*, vol. 17, pp. 48–55, 2017.
- [91] C. J. Ackerson, P. D. Jadzinsky, J. Z. Sexton, D. A. Bushnell, and R. D. Kornberg, "Synthesis and bioconjugation of 2 and 3 nm-diameter gold nanoparticles," *Bioconjugate chemistry*, vol. 21, no. 2, pp. 214–218, 2010.
- [92] M.-C. Bowman, T. E. Ballard, C. J. Ackerson, D. L. Feldheim, D. M. Margolis, and C. Melander, "Inhibition of hiv fusion with multivalent gold nanoparticles," *Journal of the American Chemical Society*, vol. 130, no. 22, pp. 6896–6897, 2008.
- [93] D. A. Giljohann, D. S. Seferos, W. L. Daniel, M. D. Massich, P. C. Patel, and C. A. Mirkin, "Gold nanoparticles for biology and medicine," *Angewandte Chemie International Edition*, vol. 49, no. 19, pp. 3280–3294, 2010.
- [94] Y. Bai, Y. Zhou, H. Liu, L. Fang, J. Liang, and S. Xiao, "Glutathione-stabilized fluorescent gold nanoclusters vary in their influences on the proliferation of pseudorabies virus and porcine reproductive and respiratory syndrome virus," *ACS Applied Nano Materials*, vol. 1, no. 2, pp. 969–976, 2018.
- [95] D. A. Boyd, "Sulfur and its role in modern materials science," *Angewandte Chemie International Edition*, vol. 55, no. 50, pp. 15486–15502, 2016.
- [96] C. Zeng, Y. Chen, C. Liu, K. Nobusada, N. L. Rosi, and R. Jin, "Gold tetrahedra coil up: Kekulé-like and double helical superstructures," *Science advances*, vol. 1, no. 9, p. e1500425, 2015.
- [97] J. R. Reimers, M. J. Ford, A. Halder, J. Ulstrup, and N. S. Hush, "Gold surfaces and nanoparticles are protected by au (0)-thiyl species and are destroyed when au (i)-thiolates form," *Proceedings of the National Academy of Sciences*, vol. 113, no. 11, pp. E1424–E1433, 2016.
- [98] T. Kamra, S. Chaudhary, C. Xu, L. Montelius, J. Schnadt, and L. Ye, "Covalent immobilization of molecularly imprinted polymer nanoparticles on a gold surface using carbodiimide coupling for chemical sensing," *Journal of colloid and interface science*, vol. 461, pp. 1–8, 2016.
- [99] T. A. Su, M. Neupane, M. L. Steigerwald, L. Venkataraman, and C. Nuckolls, "Chemical principles of single-molecule electronics," *Nature Reviews Materials*, vol. 1, no. 3, pp. 1–15, 2016.
- [100] A. B. Serrano-Montes, D. Jimenez de Aberasturi, J. Langer, J. J. Giner-Casares, L. Scarabelli, A. Herero, and L. M. Liz-Marzan, "A general method for solvent exchange of plasmonic nanoparticles and self-assembly into sers-active monolayers," *Langmuir*, vol. 31, no. 33, pp. 9205–9213, 2015.
- [101] A. Lombardi, M. K. Schmidt, L. Weller, W. M. Deacon, F. Benz, B. de Nijs, J. Aizpurua, and J. J. Baumberg, "Pulsed molecular optomechanics in plasmonic nanocavities: from nonlinear vibrational instabilities to bond-breaking," *Physical Review X*, vol. 8, no. 1, p. 011016, 2018.

- [102] C. Goldmann, R. Lazzari, X. Paquez, C. Boissière, F. Ribot, C. Sanchez, C. Chanéac, and D. Portehault, "Charge transfer at hybrid interfaces: plasmonics of aromatic thiol-capped gold nanoparticles," *ACS nano*, vol. 9, no. 7, pp. 7572–7582, 2015.
- [103] Y. Xue, X. Li, H. Li, and W. Zhang, "Quantifying thiol–gold interactions towards the efficient strength control," *Nature communications*, vol. 5, no. 1, pp. 1–9, 2014.
- [104] H. Häkkinen, "The gold–sulfur interface at the nanoscale," *Nature chemistry*, vol. 4, no. 6, p. 443, 2012.
- [105] O. Voznyy, J. J. Dubowski, J. T. Yates Jr, and P. Maksymovych, "The role of gold adatoms and stereochemistry in self-assembly of methylthiolate on au (111)," *Journal of the American Chemical Society*, vol. 131, no. 36, pp. 12989–12993, 2009.
- [106] P. Maksymovych and J. T. Yates Jr, "Au adatoms in self-assembly of benzenethiol on the au (111) surface," *Journal of the American Chemical Society*, vol. 130, no. 24, pp. 7518–7519, 2008.
- [107] H. Walch, J. Dienstmaier, G. Eder, R. Gutzler, S. Schlogl, T. Sirtl, K. Das, M. Schmittel, and M. Lackinger, "Extended two-dimensional metal–organic frameworks based on thiolate–copper coordination bonds," *Journal of the American Chemical Society*, vol. 133, no. 20, pp. 7909–7915, 2011.
- [108] A. Rastgoo-Lahrood, N. Martsinovich, M. Lischka, J. Eichhorn, P. Szabelski, D. Nieckarz, T. Strunskus, K. Das, M. Schmittel, W. M. Heckl, *et al.*, "From au–thiolate chains to thioether sierpinski triangles: The versatile surface chemistry of 1, 3, 5-tris (4-mercaptophenyl) benzene on au (111)," *Acs Nano*, vol. 10, no. 12, pp. 10901–10911, 2016.
- [109] J. Lobo-Checa, M. Matena, K. Müller, J. H. Dil, F. Meier, L. H. Gade, T. A. Jung, and M. Stöhr, "Band formation from coupled quantum dots formed by a nanoporous network on a copper surface," *Science*, vol. 325, no. 5938, pp. 300–303, 2009.
- [110] S. Wang, W. Wang, L. Z. Tan, X. G. Li, Z. Shi, G. Kuang, P. N. Liu, S. G. Louie, and N. Lin, "Tuning two-dimensional band structure of cu (111) surface-state electrons that interplay with artificial supramolecular architectures," *Physical Review B*, vol. 88, no. 24, p. 245430, 2013.
- [111] F. Klappenberger, D. Kuhne, W. Krenner, I. Silanes, A. Arnau, F. J. Garcia de Abajo, S. Klyatskaya, M. Ruben, and J. V. Barth, "Dichotomous array of chiral quantum corrals by a self-assembled nanoporous kagomé network," *Nano letters*, vol. 9, no. 10, pp. 3509–3514, 2009.
- [112] F. Klappenberger, D. Kühne, W. Krenner, I. Silanes, A. Arnau, F. G. de Abajo, S. Klyatskaya, M. Ruben, and J. Barth, "Tunable quantum dot arrays formed from self-assembled metal-organic networks," *Physical review letters*, vol. 106, no. 2, p. 026802, 2011.
- [113] K. Müller, M. Enache, and M. Stöhr, "Confinement properties of 2d porous molecular networks on metal surfaces," *Journal of Physics: Condensed Matter*, vol. 28, no. 15, p. 153003, 2016.
- [114] M. Yu, H. Ascolani, G. Zampieri, D. Woodruff, C. Satterley, R. G. Jones, and V. Dhanak, "The structure of atomic sulfur phases on au (111)," *The Journal of Physical Chemistry C*, vol. 111, no. 29, pp. 10904–10914, 2007.
- [115] B. Min, A. Alemozafar, M. Biener, J. Biener, and C. Friend, "Reaction of au (111) with sulfur and oxygen: scanning tunneling microscopic study," *Topics in Catalysis*, vol. 36, no. 1-4, pp. 77–90, 2005.
- [116] S. Clair and D. G. de Oteyza, "Controlling a chemical coupling reaction on a surface: tools and strategies for on-surface synthesis," *Chemical reviews*, vol. 119, no. 7, pp. 4717–4776, 2019.
- [117] C. K. Krug, Q. Fan, F. Fillsack, J. Glowatzki, N. Trebel, L. J. Heuplick, T. Koehler, and J. M. Gottfried, "Organometallic ring vs. chain formation beyond kinetic control: steering their equilibrium in two-dimensional confinement," *Chemical Communications*, vol. 54, no. 70, pp. 9741–9744, 2018.
- [118] Q. Fan, J. Dai, T. Wang, J. Kuttner, G. Hilt, J. M. Gottfried, and J. Zhu, "Confined synthesis of organometallic chains and macrocycles by cu–o surface templating," *ACS nano*, vol. 10, no. 3, pp. 3747–3754, 2016.
- [119] Q. Fan, T. Wang, J. Dai, J. Kuttner, G. Hilt, J. M. Gottfried, and J. Zhu, "On-surface pseudo-high-dilution synthesis of macrocycles: principle and mechanism," *ACS nano*, vol. 11, no. 5, pp. 5070–5079, 2017.
- [120] Y. Yang and L. Fan, "High-resolution xps study of decanethiol on au (111): Single sulfur–gold bonding interaction," *Langmuir*, vol. 18, no. 4, pp. 1157–1164, 2002.
- [121] T. Ishida, M. Hara, I. Kojima, S. Tsuneda, N. Nishida, H. Sasabe, and W. Knoll, "High resolution x-ray photoelectron spectroscopy measurements of octadecanethiol self-assembled monolayers on au (111)," *Langmuir*, vol. 14, no. 8, pp. 2092–2096, 1998.
- [122] D. A. Hutt, E. Cooper, and G. J. Leggett, "Structure and mechanism of photooxidation of self-assembled monolayers of alkylthiols on silver studied by xps and static sims," *The Journal of Physical Chemistry B*, vol. 102, no. 1, pp. 174–184, 1998.

- [123] D. G. Castner, K. Hinds, and D. W. Grainger, "X-ray photoelectron spectroscopy sulfur 2p study of organic thiol and disulfide binding interactions with gold surfaces," *Langmuir*, vol. 12, no. 21, pp. 5083–5086, 1996.
- [124] L. J. Cristina, G. Ruano, R. Salvarezza, and J. Ferron, "Thermal stability of self-assembled monolayers of n-hexanethiol on au (111)-(1×1) and au (001)-(1×1)," *The Journal of Physical Chemistry C*, vol. 121, no. 50, pp. 27894–27904, 2017.
- [125] D. Nilsson, S. Watcharinyanon, M. Eng, L. Li, E. Moons, L. S. Johansson, M. Zharnikov, A. Shaporenko, B. Albinsson, and J. Mårtensson, "Characterization of self-assembled monolayers of oligo (phenyleneethynylene) derivatives of varying shapes on gold: Effect of laterally extended π -systems," *Langmuir*, vol. 23, no. 11, pp. 6170–6181, 2007.
- [126] J. Noh, E. Ito, K. Nakajima, J. Kim, H. Lee, and M. Hara, "High-resolution stm and xps studies of thiophene self-assembled monolayers on au (111)," *The Journal of Physical Chemistry B*, vol. 106, no. 29, pp. 7139–7141, 2002.
- [127] I. Piquero-Zulaica, A. Garcia-Lekue, L. Colazzo, C. K. Krug, M. S. Mohammed, Z. M. Abd El-Fattah, J. M. Gottfried, D. G. de Oteyza, J. E. Ortega, and J. Lobo-Checa, "Electronic structure tunability by periodic meta-ligand spacing in one-dimensional organic semiconductors," *ACS nano*, vol. 12, no. 10, pp. 10537–10544, 2018.
- [128] N. Merino-Díez, A. Garcia-Lekue, E. Carbonell-Sanroma, J. Li, M. Corso, L. Colazzo, F. Sedona, D. Sánchez-Portal, J. I. Pascual, and D. G. de Oteyza, "Width-dependent band gap in arm-chair graphene nanoribbons reveals fermi level pinning on au (111)," *ACS nano*, vol. 11, no. 11, pp. 11661–11668, 2017.
- [129] I. Piquero-Zulaica, J. Lobo-Checa, A. Sadeghi, Z. M. Abd El-Fattah, C. Mitsui, T. Okamoto, R. Pawlak, T. Meier, A. Arnau, J. E. Ortega, *et al.*, "Precise engineering of quantum dot array coupling through their barrier widths," *Nature communications*, vol. 8, no. 1, pp. 1–6, 2017.
- [130] T. M. Figueira-Duarte and K. Mullen, "Pyrene-based materials for organic electronics," *Chemical reviews*, vol. 111, no. 11, pp. 7260–7314, 2011.
- [131] A. C. McKinlay, R. E. Morris, P. Horcajada, G. Férey, R. Gref, P. Couvreur, and C. Serre, "Biomofs: metal–organic frameworks for biological and medical applications," *Angewandte Chemie International Edition*, vol. 49, no. 36, pp. 6260–6266, 2010.
- [132] R. Ricco, W. Liang, S. Li, J. J. Gassensmith, F. Caruso, C. Doonan, and P. Falcaro, "Metal–organic frameworks for cell and virus biology: a perspective," *ACS nano*, vol. 12, no. 1, pp. 13–23, 2018.
- [133] P. Li, J. Li, X. Feng, J. Li, Y. Hao, J. Zhang, H. Wang, A. Yin, J. Zhou, X. Ma, *et al.*, "Metal-organic frameworks with photocatalytic bactericidal activity for integrated air cleaning," *Nature communications*, vol. 10, no. 1, pp. 1–10, 2019.
- [134] N. A. Mohamed, R. P. Davies, P. D. Lickiss, B. Ahmetaj-Shala, D. M. Reed, H. H. Gashaw, H. Saleem, G. R. Freeman, P. M. George, S. J. Wort, *et al.*, "Chemical and biological assessment of metal organic frameworks (mofs) in pulmonary cells and in an acute in vivo model: relevance to pulmonary arterial hypertension therapy," *Pulmonary circulation*, vol. 7, no. 3, pp. 643–653, 2017.
- [135] M. P. Suh, H. J. Park, T. K. Prasad, and D.-W. Lim, "Hydrogen storage in metal–organic frameworks," *Chemical reviews*, vol. 112, no. 2, pp. 782–835, 2012.
- [136] H. W. Langmi, J. Ren, B. North, M. Mathe, and D. Bessarabov, "Hydrogen storage in metal-organic frameworks: a review," *Electrochimica Acta*, vol. 128, pp. 368–392, 2014.
- [137] M. Ding, R. W. Flaig, H.-L. Jiang, and O. M. Yaghi, "Carbon capture and conversion using metal–organic frameworks and mof-based materials," *Chemical Society Reviews*, vol. 48, no. 10, pp. 2783–2828, 2019.
- [138] H. Li, K. Wang, Y. Sun, C. T. Lollar, J. Li, and H.-C. Zhou, "Recent advances in gas storage and separation using metal–organic frameworks," *Materials Today*, vol. 21, no. 2, pp. 108–121, 2018.
- [139] J. Qiu, X. Zhang, Y. Feng, X. Zhang, H. Wang, and J. Yao, "Modified metal-organic frameworks as photocatalysts," *Applied Catalysis B: Environmental*, vol. 231, pp. 317–342, 2018.
- [140] Y. Li, H. Xu, S. Ouyang, and J. Ye, "Metal–organic frameworks for photocatalysis," *Physical Chemistry Chemical Physics*, vol. 18, no. 11, pp. 7563–7572, 2016.
- [141] F. Klappenberger, Y.-Q. Zhang, J. Bjork, S. Klyatskaya, M. Ruben, and J. V. Barth, "On-surface synthesis of carbon-based scaffolds and nanomaterials using terminal alkynes," *Accounts of chemical research*, vol. 48, no. 7, pp. 2140–2150, 2015.
- [142] L. Colazzo, M. S. Mohammed, A. Gallardo, Z. M. Abd El-Fattah, J. A. Pomposo, P. Jelínek, and D. G. de Oteyza, "Controlling the stereospecific bonding motif of au–thiolate links," *Nanoscale*, vol. 11, no. 33, pp. 15567–15575, 2019.
- [143] D. G. de Oteyza, A. Perez Paz, Y.-C. Chen, Z. Pedramrazi, A. Riss, S. Wickenburg, H.-Z. Tsai, F. R. Fischer, M. F. Crommie, and A. Rubio, "Noncovalent dimerization after enediyne cyclization on au (111)," *Journal of the American Chemical Society*, vol. 138, no. 34, pp. 10963–10967, 2016.

- [144] L. L. Patera, S. Sokolov, J. Z. Low, L. M. Campos, L. Venkataraman, and J. Repp, "Resolving the unpaired-electron orbital distribution in a stable organic radical by kondo resonance mapping," *Angewandte Chemie International Edition*, vol. 58, no. 32, pp. 11063–11067, 2019.
- [145] I. Fernandez-Torrente, S. Monturet, K. Franke, J. Fraxedas, N. Lorente, and J. Pascual, "Long-range repulsive interaction between molecules on a metal surface induced by charge transfer," *Physical review letters*, vol. 99, no. 17, p. 176103, 2007.
- [146] H.-Y. Gao, J.-H. Franke, H. Wagner, D. Zhong, P.-A. Held, A. Studer, and H. Fuchs, "Effect of metal surfaces in on-surface glaser coupling," *The Journal of Physical Chemistry C*, vol. 117, no. 36, pp. 18595–18602, 2013.
- [147] P. Jelínek, "High resolution spm imaging of organic molecules with functionalized tips," *Journal of Physics: Condensed Matter*, vol. 29, no. 34, p. 343002, 2017.
- [148] R. Azpiroz, L. Rubio-Perez, R. Castarlenas, J. J. Pérez-Torrente, and L. A. Oro, "gem-selective cross-dimerization and cross-trimerization of alkynes with silylacetylenes promoted by a rhodium-pyridine-*n*-heterocyclic carbene catalyst," 2014.
- [149] B. M. Trost, M. T. Sorum, C. Chan, and G. Rühler, "Palladium-catalyzed additions of terminal alkynes to acceptor alkynes," *Journal of the American Chemical Society*, vol. 119, no. 4, pp. 698–708, 1997.
- [150] H.-D. Xu, R.-W. Zhang, X. Li, S. Huang, W. Tang, and W.-H. Hu, "Rhodium-catalyzed chemo- and regioselective cross-dimerization of two terminal alkynes," *Organic letters*, vol. 15, no. 4, pp. 840–843, 2013.
- [151] A. Sánchez-Grande, B. De la Torre, J. Santos, B. Cirera, K. Lauwaet, T. Chutora, S. Edalatmanesh, P. Mutombo, J. Rosen, R. Zbořil, *et al.*, "On-surface synthesis of ethynylene-bridged anthracene polymers," *Angewandte Chemie International Edition*, vol. 58, no. 20, pp. 6559–6563, 2019.
- [152] R. Gutzler and D. F. Perepichka, " π -electron conjugation in two dimensions," *Journal of the American Chemical Society*, vol. 135, no. 44, pp. 16585–16594, 2013.
- [153] Q. Sun, O. Gröning, J. Overbeck, O. Braun, M. L. Perrin, G. Borin Barin, M. El Abbassi, K. Eimre, E. Ditler, C. Daniels, *et al.*, "Massive dirac fermion behavior in a low bandgap graphene nanoribbon near a topological phase boundary," *Advanced materials*, vol. 32, no. 12, p. 1906054, 2020.
- [154] B. Cirera, A. Sánchez-Grande, B. de la Torre, J. Santos, S. Edalatmanesh, E. Rodríguez-Sánchez, K. Lauwaet, B. Mallada, R. Zbořil, R. Miranda, *et al.*, "Tailoring topological order and π -conjugation to engineer quasi-metallic polymers," *Nature Nanotechnology*, pp. 1–7, 2020.
- [155] Y. Zhao, R. McDonald, and R. R. Tykwinski, "Study of cross-conjugated iso-polytriacetylenes and related oligoenynes," *The Journal of organic chemistry*, vol. 67, no. 9, pp. 2805–2812, 2002.
- [156] M. H. van der Veen, M. T. Rispens, H. T. Jonkman, and J. C. Hummelen, "Molecules with linear π -conjugated pathways between all substituents: omniconjugation," *Advanced Functional Materials*, vol. 14, no. 3, pp. 215–223, 2004.
- [157] F. Bebensee, C. Bombis, S.-R. Vadapoo, J. R. Cramer, F. Besenbacher, K. V. Gothelf, and T. R. Linderoth, "On-surface azide-alkyne cycloaddition on cu (111): does it "click" in ultrahigh vacuum?," *Journal of the American Chemical Society*, vol. 135, no. 6, pp. 2136–2139, 2013.
- [158] O. Diaz Arado, H. Monig, H. Wagner, J.-H. Franke, G. Langewisch, P. A. Held, A. Studer, and H. Fuchs, "On-surface azide-alkyne cycloaddition on au (111)," *ACS nano*, vol. 7, no. 10, pp. 8509–8515, 2013.
- [159] V. K. Kanuru, G. Kyriakou, S. K. Beaumont, A. C. Papageorgiou, D. J. Watson, and R. M. Lambert, "Sonogashira coupling on an extended gold surface in vacuo: reaction of phenylacetylene with iodobenzene on au (111)," *Journal of the American Chemical Society*, vol. 132, no. 23, pp. 8081–8086, 2010.
- [160] C. Sanchez-Sanchez, F. Yubero, A. R. Gonzalez-Elipse, L. Feria, J. F. Sanz, and R. M. Lambert, "The flexible surface revisited: adsorbate-induced reconstruction, homocoupling, and sonogashira cross-coupling on the au (100) surface," *The Journal of Physical Chemistry C*, vol. 118, no. 22, pp. 11677–11684, 2014.
- [161] C. Sanchez-Sanchez, N. Orozco, J. P. Holgado, S. K. Beaumont, G. Kyriakou, D. J. Watson, A. R. Gonzalez-Elipse, L. Feria, J. Fernandez Sanz, and R. M. Lambert, "Sonogashira cross-coupling and homocoupling on a silver surface: chlorobenzene and phenylacetylene on ag (100)," *Journal of the American Chemical Society*, vol. 137, no. 2, pp. 940–947, 2015.
- [162] T. Wang, J. Huang, H. Lv, Q. Fan, L. Feng, Z. Tao, H. Ju, X. Wu, S. L. Tait, and J. Zhu, "Kinetic strategies for the formation of graphyne nanowires via sonogashira coupling on ag (111)," *Journal of the American Chemical Society*, vol. 140, no. 41, pp. 13421–13428, 2018.
- [163] R. Zhang, G. Lyu, D. Y. Li, P. N. Liu, and N. Lin, "Template-controlled sonogashira cross-coupling reactions on a au (111) surface," *Chemical Communications*, vol. 53, no. 10, pp. 1731–1734, 2017.
- [164] H.-Y. Gao, H. Wagner, D. Zhong, J.-H. Franke, A. Studer, and H. Fuchs, "Glaser coupling at metal surfaces," *Angewandte Chemie International Edition*, vol. 52, no. 14, pp. 4024–4028, 2013.

- [165] P. A. Held, H.-Y. Gao, L. Liu, C. Mück-Lichtenfeld, A. Timmer, H. Moenig, D. Barton, J. Neugebauer, H. Fuchs, and A. Studer, "On-surface domino reactions: Glaser coupling and dehydrogenative coupling of a bis(carboxylic acid) to form polymeric bisacylperoxides," *Angewandte Chemie International Edition*, vol. 55, no. 33, pp. 9777–9782, 2016.
- [166] H.-Y. Gao, D. Zhong, H. Monig, H. Wagner, P.-A. Held, A. Timmer, A. Studer, and H. Fuchs, "Photochemical glaser coupling at metal surfaces," *The Journal of Physical Chemistry C*, vol. 118, no. 12, pp. 6272–6277, 2014.
- [167] T. Wang, H. Lv, L. Feng, Z. Tao, J. Huang, Q. Fan, X. Wu, and J. Zhu, "Unravelling the mechanism of glaser coupling reaction on ag (111) and cu (111) surfaces: a case for halogen substituted terminal alkyne," *The Journal of Physical Chemistry C*, vol. 122, no. 26, pp. 14537–14545, 2018.
- [168] T. Wang, H. Lv, J. Huang, H. Shan, L. Feng, Y. Mao, J. Wang, W. Zhang, D. Han, Q. Xu, *et al.*, "Reaction selectivity of homochiral versus heterochiral intermolecular reactions of prochiral terminal alkynes on surfaces," *Nature communications*, vol. 10, no. 1, pp. 1–9, 2019.
- [169] J. Björk, Y.-Q. Zhang, F. Klappenberger, J. V. Barth, and S. Stafstrom, "Unraveling the mechanism of the covalent coupling between terminal alkynes on a noble metal," *The Journal of Physical Chemistry C*, vol. 118, no. 6, pp. 3181–3187, 2014.
- [170] Y.-Q. Zhang, N. Kepčija, M. Kleinschrodt, K. Diller, S. Fischer, A. C. Papageorgiou, F. Allegretti, J. Björk, S. Klyatskaya, F. Klappenberger, *et al.*, "Homo-coupling of terminal alkynes on a noble metal surface," *Nature communications*, vol. 3, no. 1, pp. 1–8, 2012.
- [171] Q. Sun, C. Zhang, Z. Li, H. Kong, Q. Tan, A. Hu, and W. Xu, "On-surface formation of one-dimensional polyphenylene through bergman cyclization," *Journal of the American Chemical Society*, vol. 135, no. 23, pp. 8448–8451, 2013.
- [172] D. G. de Oteyza, "Eneidyne cyclization chemistry on surfaces under ultra-high vacuum," in *On-Surface Synthesis*, pp. 85–99, Springer, 2016.
- [173] H. Zhou, J. Liu, S. Du, L. Zhang, G. Li, Y. Zhang, B. Z. Tang, and H.-J. Gao, "Direct visualization of surface-assisted two-dimensional diyne polycyclotrimerization," *Journal of the American Chemical Society*, vol. 136, no. 15, pp. 5567–5570, 2014.
- [174] F. Xiang, Y. Lu, C. Li, X. Song, X. Liu, Z. Wang, J. Liu, M. Dong, and L. Wang, "Cyclotrimerization-induced chiral supramolecular structures of 4-ethynyltriphenylamine on au (111) surface," *Chemistry: a European Journal*, vol. 21, no. 37, pp. 12978–12983, 2015.
- [175] J. Liu, P. Ruffieux, X. Feng, K. Müllen, and R. Fasel, "Cyclotrimerization of arylalkynes on au (111)," *Chemical communications*, vol. 50, no. 76, pp. 11200–11203, 2014.
- [176] Q. Li, J. Gao, Y. Li, M. Fuentes-Cabrera, M. Liu, X. Qiu, H. Lin, L. Chi, and M. Pan, "Self-assembly directed one-step synthesis of [4] radialene on cu (100) surfaces," *Nature communications*, vol. 9, no. 1, pp. 1–7, 2018.
- [177] A. Riss, S. Wickenburg, P. Gorman, L. Z. Tan, H.-Z. Tsai, D. G. de Oteyza, Y.-C. Chen, A. J. Bradley, M. M. Ugeda, G. Etkin, *et al.*, "Local electronic and chemical structure of oligo-acetylene derivatives formed through radical cyclizations at a surface," *Nano letters*, vol. 14, no. 5, pp. 2251–2255, 2014.
- [178] M. Koch, M. Gille, A. Viertel, S. Hecht, and L. Grill, "Substrate-controlled linking of molecular building blocks: Au (111) vs. cu (111)," *Surface science*, vol. 627, pp. 70–74, 2014.
- [179] T. A. Pham, F. Song, M.-T. Nguyen, Z. Li, F. Studener, and M. Stöhr, "Comparing ullmann coupling on noble metal surfaces: on-surface polymerization of 1, 3, 6, 8-tetrabromopyrene on cu (111) and au (111)," *Chemistry—A European Journal*, vol. 22, no. 17, pp. 5937–5944, 2016.
- [180] M. Lackinger, "Surface-assisted ullmann coupling," *Chemical Communications*, vol. 53, no. 56, pp. 7872–7885, 2017.
- [181] Y.-Q. Zhang, M. Paszkiewicz, P. Du, L. Zhang, T. Lin, Z. Chen, S. Klyatskaya, M. Ruben, A. P. Seitsonen, J. V. Barth, *et al.*, "Complex supramolecular interfacial tessellation through convergent multi-step reaction of a dissymmetric simple organic precursor," *Nature chemistry*, vol. 10, no. 3, p. 296, 2018.
- [182] T. Wang, H. Lv, Q. Fan, L. Feng, X. Wu, and J. Zhu, "Highly selective synthesis of cis-enediynes on a ag (111) surface," *Angewandte Chemie*, vol. 129, no. 17, pp. 4840–4844, 2017.
- [183] C. B. Aakeröy, D. Welideniya, and J. Desper, "Ethynyl hydrogen bonds and iodoethynyl halogen bonds: a case of synthon mimicry," *CrystEngComm*, vol. 19, no. 1, pp. 11–13, 2017.
- [184] G. Cavallo, P. Metrangolo, R. Milani, T. Pilati, A. Priimagi, G. Resnati, and G. Terraneo, "The halogen bond," *Chemical reviews*, vol. 116, no. 4, pp. 2478–2601, 2016.
- [185] N. Pavliček and L. Gross, "Generation, manipulation and characterization of molecules by atomic force microscopy," *Nature Reviews Chemistry*, vol. 1, no. 1, pp. 1–11, 2017.
- [186] M. Yang, L. Zhou, J. Wang, Z. Liu, and Z. Liu, "Evolutionary chlorination of graphene: from charge-transfer complex to covalent bonding and nonbonding," *The Journal of Physical Chemistry C*, vol. 116, no. 1, pp. 844–850, 2012.

- [187] S. Kawai, K. Takahashi, S. Ito, R. Pawlak, T. Meier, P. Spijker, F. F. Canova, J. Tracey, K. Nozaki, A. S. Foster, *et al.*, "Competing annulene and radialene structures in a single anti-aromatic molecule studied by high-resolution atomic force microscopy," *ACS nano*, vol. 11, no. 8, pp. 8122–8130, 2017.
- [188] M. Prall, A. Wittkopp, and P. R. Schreiner, "Can fulvenes form from enediynes? a systematic high-level computational study on parent and benzannelated enediyne and enyne-allene cyclizations," *The Journal of Physical Chemistry A*, vol. 105, no. 40, pp. 9265–9274, 2001.
- [189] Q. Sun, L. Cai, H. Ma, C. Yuan, and W. Xu, "Dehalogenative homocoupling of terminal alkynyl bromides on au (111): incorporation of acetylenic scaffolding into surface nanostructures," *ACS nano*, vol. 10, no. 7, pp. 7023–7030, 2016.
- [190] J. Liu, Q. Chen, Q. He, Y. Zhang, X. Fu, Y. Wang, D. Zhao, W. Chen, G. Q. Xu, and K. Wu, "Bromine adatom promoted c-h bond activation in terminal alkynes at room temperature on ag (111)," *Physical Chemistry Chemical Physics*, vol. 20, no. 16, pp. 11081–11088, 2018.
- [191] L. Serrano-Andrés, M. Merchán, and M. Jabłoński, "The electronic spectra of aryl olefins: A theoretical study of phenylacetylene," *The Journal of chemical physics*, vol. 119, no. 8, pp. 4294–4304, 2003.
- [192] A. M. Boldi, J. Anthony, V. Gramlich, C. B. Knobler, C. Boudon, J.-P. Gisselbrecht, M. Gross, and F. Diederich, "Acyclic tetraethynylethene molecular scaffolding: Multinanometer-sized linearly conjugated rods with the poly (triacetylene) backbone and cross-conjugated expanded dendralenes," *Helvetica chimica acta*, vol. 78, no. 4, pp. 779–796, 1995.
- [193] M. R. Bryce, M. A. Coffin, P. J. Skabara, A. J. Moore, A. S. Batsanov, and J. A. Howard, "Functionalised oligoenes with unusual topologies: Synthesis, electrochemistry and structural studies on redox-active [3]-and [4]-dendralenes," *Chemistry—A European Journal*, vol. 6, no. 11, pp. 1955–1962, 2000.
- [194] Z. Zeng, X. Shi, C. Chi, J. T. L. Navarrete, J. Casado, and J. Wu, "Pro-aromatic and anti-aromatic π -conjugated molecules: an irresistible wish to be diradicals," *Chemical Society Reviews*, vol. 44, no. 18, pp. 6578–6596, 2015.
- [195] S. Mishra, T. G. Lohr, C. A. Pignedoli, J. Liu, R. Berger, J. I. Urgel, K. Mullen, X. Feng, P. Ruffieux, and R. Fasel, "Tailoring bond topologies in open-shell graphene nanostructures," *ACS nano*, vol. 12, no. 12, pp. 11917–11927, 2018.
- [196] J. Liu, S. Mishra, C. A. Pignedoli, D. Passerone, J. I. Urgel, A. Fabrizio, T. G. Lohr, J. Ma, H. Komber, M. Baumgarten, *et al.*, "Open-shell nonbenzenoid nanographenes containing two pairs of pentagonal and heptagonal rings," *Journal of the American Chemical Society*, vol. 141, no. 30, pp. 12011–12020, 2019.
- [197] S. Yang, P. Orlishevski, and M. Kertesz, "Bandgap calculations for conjugated polymers," *Synthetic Metals*, vol. 141, no. 1-2, pp. 171–177, 2004.
- [198] A. Konishi, Y. Hirao, M. Nakano, A. Shimizu, E. Botek, B. Champagne, D. Shiomi, K. Sato, T. Takui, K. Matsumoto, *et al.*, "Synthesis and characterization of teranthene: a singlet biradical polycyclic aromatic hydrocarbon having kekulé structures," *Journal of the American Chemical Society*, vol. 132, no. 32, pp. 11021–11023, 2010.
- [199] J. E. Anthony, "Functionalized acenes and heteroacenes for organic electronics," *Chemical reviews*, vol. 106, no. 12, pp. 5028–5048, 2006.
- [200] M. Bendikov, F. Wudl, and D. F. Perepichka, "Tetrathiafulvalenes, oligoacenenenes, and their buckminsterfullerene derivatives: the brick and mortar of organic electronics," *Chemical reviews*, vol. 104, no. 11, pp. 4891–4946, 2004.
- [201] J. E. Anthony, "The larger acenes: versatile organic semiconductors," *Angewandte Chemie International Edition*, vol. 47, no. 3, pp. 452–483, 2008.
- [202] S. S. Zade and M. Bendikov, "Reactivity of acenes: mechanisms and dependence on acene length," *Journal of Physical Organic Chemistry*, vol. 25, no. 6, pp. 452–461, 2012.
- [203] S. S. Zade, N. Zamoshchik, A. R. Reddy, G. Fridman-Marueli, D. Sheberla, and M. Bendikov, "Products and mechanism of acene dimerization. a computational study," *Journal of the American Chemical Society*, vol. 133, no. 28, pp. 10803–10816, 2011.
- [204] R. Dorel and A. M. Echavarren, "Strategies for the synthesis of higher acenes," *European journal of organic chemistry*, vol. 2017, no. 1, pp. 14–24, 2017.
- [205] R. Mondal, B. K. Shah, and D. C. Neckers, "Photogeneration of heptacene in a polymer matrix," *Journal of the American Chemical Society*, vol. 128, no. 30, pp. 9612–9613, 2006.
- [206] C. Tönshoff and H. F. Bettinger, "Photogeneration of octacene and nonacene," *Angewandte Chemie International Edition*, vol. 49, no. 24, pp. 4125–4128, 2010.
- [207] B. Shen, J. Tatchen, E. Sanchez-Garcia, and H. F. Bettinger, "Evolution of the optical gap in the acene series: undecacene," *Angewandte Chemie*, vol. 130, no. 33, pp. 10666–10669, 2018.

- [208] M. Bendikov, H. M. Duong, K. Starkey, K. Houk, E. A. Carter, and F. Wudl, "Oligoacenes: theoretical prediction of open-shell singlet diradical ground states," *Journal of the American Chemical Society*, vol. 126, no. 24, pp. 7416–7417, 2004.
- [209] Y. Yang, E. R. Davidson, and W. Yang, "Nature of ground and electronic excited states of higher acenes," *Proceedings of the National Academy of Sciences*, vol. 113, no. 35, pp. E5098–E5107, 2016.
- [210] J. Hachmann, J. J. Dorando, M. Avilés, and G. K.-L. Chan, "The radical character of the acenes: a density matrix renormalization group study," *The Journal of chemical physics*, vol. 127, no. 13, p. 134309, 2007.
- [211] J. Krüger, N. Pavlicek, J. M. Alonso, D. Perez, E. Guitian, T. Lehmann, G. Cuniberti, A. Gourdon, G. Meyer, L. Gross, *et al.*, "Tetracene formation by on-surface reduction," *ACS nano*, vol. 10, no. 4, pp. 4538–4542, 2016.
- [212] J. Krüger, F. Eisenhut, J. M. Alonso, T. Lehmann, E. Guitián, D. Pérez, D. Skidin, F. Gamaleja, D. A. Ryndyk, C. Joachim, *et al.*, "Imaging the electronic structure of on-surface generated hexacene," *Chemical Communications*, vol. 53, no. 10, pp. 1583–1586, 2017.
- [213] J. I. Urgel, H. Hayashi, M. Di Giovannantonio, C. A. Pignedoli, S. Mishra, O. Deniz, M. Yamashita, T. Dienel, P. Ruffieux, H. Yamada, *et al.*, "On-surface synthesis of heptacene organometallic complexes," *Journal of the American Chemical Society*, vol. 139, no. 34, pp. 11658–11661, 2017.
- [214] R. Zuzak, R. Dorel, M. Kolmer, M. Szymonski, S. Godlewski, and A. M. Echavarren, "Higher acenes by on-surface dehydrogenation: From heptacene to undecacene," *Angewandte Chemie International Edition*, vol. 57, no. 33, pp. 10500–10505, 2018.
- [215] J. Krüger, F. García, F. Eisenhut, D. Skidin, J. M. Alonso, E. Guitián, D. Pérez, G. Cuniberti, F. Moresco, and D. Peña, "Decacene: On-surface generation," *Angewandte Chemie*, vol. 129, no. 39, pp. 12107–12110, 2017.
- [216] L. E. Dinca, C. Fu, J. M. MacLeod, J. Lipton-Duffin, J. L. Brusso, C. E. Szakacs, D. Ma, D. F. Perepichka, and F. Rosei, "Unprecedented transformation of tetrathienoanthracene into pentacene on ni (111)," *ACS nano*, vol. 7, no. 2, pp. 1652–1657, 2013.
- [217] M. Zugermeier, M. Gruber, M. Schmid, B. P. Klein, L. Ruppenthal, P. Müller, R. Einholz, W. Hieringer, R. Berndt, H. F. Bettinger, *et al.*, "On-surface synthesis of heptacene and its interaction with a metal surface," *Nanoscale*, vol. 9, no. 34, pp. 12461–12469, 2017.
- [218] R. Dorel, P. R. McGonigal, and A. M. Echavarren, "Hydroacenes made easy by gold (i) catalysis," *Angewandte Chemie International Edition*, vol. 55, no. 37, pp. 11120–11123, 2016.
- [219] H. Walch, R. Gutzler, T. Sirtl, G. Eder, and M. Lackinger, "Material-and orientation-dependent reactivity for heterogeneously catalyzed carbon- bromine bond homolysis," *The Journal of Physical Chemistry C*, vol. 114, no. 29, pp. 12604–12609, 2010.
- [220] G. Galeotti, M. Di Giovannantonio, J. Lipton-Duffin, M. Ebrahimi, S. Tebi, A. Verdini, L. Floreano, Y. Fagot-Revurat, D. F. Perepichka, F. Rosei, *et al.*, "The role of halogens in on-surface ullmann polymerization," *Faraday Discussions*, vol. 204, pp. 453–469, 2017.
- [221] S. W. Slayden and J. F. Liebman, "The energetics of aromatic hydrocarbons: an experimental thermochemical perspective," *Chemical reviews*, vol. 101, no. 5, pp. 1541–1566, 2001.
- [222] G. Heimel, S. Duhm, I. Salzmann, A. Gerlach, A. Strozecka, J. Niederhausen, C. Bürker, T. Hosokai, I. Fernandez-Torrente, G. Schulze, *et al.*, "Charged and metallic molecular monolayers through surface-induced aromatic stabilization," *Nature chemistry*, vol. 5, no. 3, p. 187, 2013.
- [223] E. Goiri, P. Borghetti, A. El-Sayed, J. E. Ortega, and D. G. de Oteyza, "Multi-component organic layers on metal substrates," *Advanced Materials*, vol. 28, no. 7, pp. 1340–1368, 2016.
- [224] B. de la Torre, M. Švec, G. Foti, O. Krejčí, P. Hapala, A. Garcia-Lekue, T. Frederiksen, R. Zbořil, A. Arnau, H. Vázquez, *et al.*, "Submolecular resolution by variation of the inelastic electron tunneling spectroscopy amplitude and its relation to the afm/stm signal," *Physical Review Letters*, vol. 119, no. 16, p. 166001, 2017.
- [225] C. Riedl, C. Coletti, T. Iwasaki, A. Zakharov, and U. Starke, "Quasi-free-standing epitaxial graphene on sic obtained by hydrogen intercalation," *Physical review letters*, vol. 103, no. 24, p. 246804, 2009.
- [226] I. Palacio, L. Aballe, M. Foerster, D. de Oteyza, M. García-Hernández, and J. A. Martín-Gago, "Reversible graphene decoupling by nacl photo-dissociation," *2D Materials*, vol. 6, no. 2, p. 025021, 2019.
- [227] O. Deniz, C. Sánchez-Sánchez, T. Dumlaff, X. Feng, A. Narita, K. Mullen, N. Kharche, V. Meunier, R. Fasel, and P. Ruffieux, "Revealing the electronic structure of silicon intercalated armchair graphene nanoribbons by scanning tunneling spectroscopy," *Nano letters*, vol. 17, no. 4, pp. 2197–2203, 2017.

- [228] J. Repp, G. Meyer, S. M. Stojković, A. Gourdon, and C. Joachim, "Molecules on insulating films: scanning-tunneling microscopy imaging of individual molecular orbitals," *Physical Review Letters*, vol. 94, no. 2, p. 026803, 2005.
- [229] F. Moresco and A. Gourdon, "Scanning tunneling microscopy experiments on single molecular landers," *Proceedings of the National Academy of Sciences*, vol. 102, no. 25, pp. 8809–8814, 2005.
- [230] F. Matino, G. Schull, F. Köhler, S. Gabutti, M. Mayor, and R. Berndt, "Electronic decoupling of a cyclophane from a metal surface," *Proceedings of the National Academy of Sciences*, vol. 108, no. 3, pp. 961–964, 2011.
- [231] M. Alemani, M. V. Peters, S. Hecht, K.-H. Rieder, F. Moresco, and L. Grill, "Electric field-induced isomerization of azobenzene by stm," *Journal of the American Chemical Society*, vol. 128, no. 45, pp. 14446–14447, 2006.
- [232] M. J. Comstock, N. Levy, A. Kirakosian, J. Cho, F. Lauterwasser, J. H. Harvey, D. A. Strubbe, J. M. Fréchet, D. Trauner, S. G. Louie, *et al.*, "Reversible photomechanical switching of individual engineered molecules at a metallic surface," *Physical review letters*, vol. 99, no. 3, p. 038301, 2007.
- [233] S. Mishra, D. Beyer, K. Eimre, S. Kezilebieke, R. Berger, O. Gröning, C. A. Pignedoli, K. Müllen, P. Liljeroth, P. Ruffieux, *et al.*, "Topological frustration induces unconventional magnetism in a nanographene," *Nature nanotechnology*, vol. 15, no. 1, pp. 22–28, 2020.
- [234] J. Li, S. Sanz, M. Corso, D. J. Choi, D. Peña, T. Frederiksen, and J. I. Pascual, "Single spin localization and manipulation in graphene open-shell nanostructures," *Nature communications*, vol. 10, no. 1, pp. 1–7, 2019.
- [235] N. Pavliček, A. Mistry, Z. Majzik, N. Moll, G. Meyer, D. J. Fox, and L. Gross, "Synthesis and characterization of triangulene," *Nature Nanotechnology*, vol. 12, no. 4, pp. 308–311, 2017.
- [236] S. Mishra, D. Beyer, K. Eimre, J. Liu, R. Berger, O. Groning, C. A. Pignedoli, K. Mullen, R. Fasel, X. Feng, *et al.*, "Synthesis and characterization of π -extended triangulene," *Journal of the American Chemical Society*, vol. 141, no. 27, pp. 10621–10625, 2019.
- [237] J. Li, S. Sanz, J. Castro-Esteban, M. Vilas-Varela, N. Friedrich, T. Frederiksen, D. Peña, and J. I. Pascual, "Uncovering the triplet ground state of triangular graphene nanoflakes engineered with atomic precision on a metal surface," *Physical Review Letters*, vol. 124, no. 17, p. 177201, 2020.
- [238] M. Hollerer, D. Luftner, P. Hurdax, T. Ules, S. Soubatch, F. S. Tautz, G. Koller, P. Puschnig, M. Sterrer, and M. G. Ramsey, "Charge transfer and orbital level alignment at inorganic/organic interfaces: The role of dielectric interlayers," *ACS nano*, vol. 11, no. 6, pp. 6252–6260, 2017.
- [239] P. W. Anderson, "Localized magnetic states in metals," *Physical Review*, vol. 124, no. 1, p. 41, 1961.
- [240] G. Nazin, S. Wu, and W. Ho, "Tunneling rates in electron transport through double-barrier molecular junctions in a scanning tunneling microscope," *Proceedings of the National Academy of Sciences*, vol. 102, no. 25, pp. 8832–8837, 2005.
- [241] G. Mikaelian, N. Ogawa, X. Tu, and W. Ho, "Atomic scale control of single molecule charging," 2006.
- [242] L. Gross, B. Schuler, F. Mohn, N. Moll, N. Pavliček, W. Steurer, I. Scivetti, K. Kotsis, M. Persson, and G. Meyer, "Investigating atomic contrast in atomic force microscopy and kelvin probe force microscopy on ionic systems using functionalized tips," *Physical Review B*, vol. 90, no. 15, p. 155455, 2014.
- [243] A. Kumar, K. Banerjee, M. Dvorak, F. Schulz, A. Harju, P. Rinke, and P. Liljeroth, "Charge-transfer-driven nonplanar adsorption of f4tcnq molecules on epitaxial graphene," *ACS nano*, vol. 11, no. 5, pp. 4960–4968, 2017.
- [244] I. Fernández-Torrente, D. Kreikemeyer-Lorenzo, A. Stróżecka, K. J. Franke, and J. I. Pascual, "Gating the charge state of single molecules by local electric fields," *Physical review letters*, vol. 108, no. 3, p. 036801, 2012.
- [245] K. A. Cochrane, A. Schiffrin, T. S. Roussy, M. Capsoni, and S. A. Burke, "Pronounced polarization-induced energy level shifts at boundaries of organic semiconductor nanostructures," *Nature communications*, vol. 6, no. 1, pp. 1–8, 2015.
- [246] E. Goiri, M. Matena, A. El-Sayed, J. Lobo-Checa, P. Borghetti, C. Rogero, B. Detlefs, J. Duvernay, J. Ortega, and D. De Oteyza, "Self-assembly of bicomponent molecular monolayers: Adsorption height changes and their consequences," *Physical review letters*, vol. 112, no. 11, p. 117602, 2014.
- [247] P. Borghetti, A. El-Sayed, E. Goiri, C. Rogero, J. Lobo-Checa, L. Floreano, J. E. Ortega, and D. G. de Oteyza, "Spectroscopic fingerprints of work-function-controlled phthalocyanine charging on metal surfaces," *ACS nano*, vol. 8, no. 12, pp. 12786–12795, 2014.
- [248] L. Vitali, G. Levita, R. Ohmann, A. Comisso, A. De Vita, and K. Kern, "Portrait of the potential barrier at metal–organic nanocontacts," *Nature materials*, vol. 9, no. 4, pp. 320–323, 2010.
- [249] K. Kaiser, L. M. Scriven, F. Schulz, P. Gawel, L. Gross, and H. L. Anderson, "An sp-hybridized molecular carbon allotrope, cyclo [18] carbon," *Science*, vol. 365, no. 6459, pp. 1299–1301, 2019.

- [250] M. Corso, E. Carbonell-Sanromà, and D. G. d. Oteyza, "Bottom-up fabrication of atomically precise graphene nanoribbons," in *On-Surface Synthesis II*, Springer Nature, 2018.
- [251] I. Pozo, E. Guitian, D. Perez, and D. Pena, "Synthesis of nanographenes, starphenes, and sterically congested polyarenes by aryne cyclotrimerization," *Accounts of chemical research*, vol. 52, no. 9, pp. 2472–2481, 2019.
- [252] L. Grill, M. Dyer, L. Lafferentz, M. Persson, M. V. Peters, and S. Hecht, "Nano-architectures by covalent assembly of molecular building blocks," *Nature nanotechnology*, vol. 2, no. 11, pp. 687–691, 2007.
- [253] P. Iavicoli, S. Haq, D. B. Amabilino, R. Raval, *et al.*, "Unique intermolecular reaction of simple porphyrins at a metal surface gives covalent nanostructures," *Chemical communications*, no. 13, pp. 1536–1538, 2008.
- [254] D. De Oteyza, A. El-Sayed, J. Garcia-Lastra, E. Goiri, T. Krauss, A. Turak, E. Barrena, H. Dosch, J. Zegenhagen, A. Rubio, *et al.*, "Copper-phthalocyanine based metal–organic interfaces: The effect of fluorination, the substrate, and its symmetry," *The Journal of chemical physics*, vol. 133, no. 21, p. 214703, 2010.
- [255] F. Babudri, G. M. Farinola, F. Naso, and R. Ragni, "Fluorinated organic materials for electronic and optoelectronic applications: the role of the fluorine atom," *Chemical Communications*, no. 10, pp. 1003–1022, 2007.
- [256] A. Kukhta, I. Kukhta, N. Kukhta, O. Neyra, and E. Meza, "Dft study of the electronic structure of anthracene derivatives in their neutral, anion and cation forms," *Journal of Physics B: Atomic, Molecular and Optical Physics*, vol. 41, no. 20, p. 205701, 2008.
- [257] C. Steiner, J. Gebhardt, M. Ammon, Z. Yang, A. Heidenreich, N. Hammer, A. Görling, M. Kivala, and S. Maier, "Hierarchical on-surface synthesis and electronic structure of carbonyl-functionalized one- and two-dimensional covalent nanoarchitectures," *Nature communications*, vol. 8, no. 1, pp. 1–11, 2017.
- [258] W.-H. Soe, C. Manzano, A. De Sarkar, N. Chandrasekhar, and C. Joachim, "Direct observation of molecular orbitals of pentacene physisorbed on au (111) by scanning tunneling microscope," *Physical review letters*, vol. 102, no. 17, p. 176102, 2009.
- [259] M. Copel, P. Fenter, and T. Gustafsson, "The reconstruction and relaxation of ir (110) and au (110) surfaces," *Journal of Vacuum Science & Technology A: Vacuum, Surfaces, and Films*, vol. 5, no. 4, pp. 742–746, 1987.
- [260] G. N. Derry, M. E. Kern, and E. H. Worth, "Recommended values of clean metal surface work functions," *Journal of Vacuum Science & Technology A: Vacuum, Surfaces, and Films*, vol. 33, no. 6, p. 060801, 2015.